COMPUTER SIMULATION

OF

GEOLOGIC SEQUESTRATION OF CO_2

by

AKAND W. ISLAM

ERIC S. CARLSON, COMMITTEE CHAIR
PETER E. CLARK
MUHAMMAD ALI ROB SHARIF
ANDREW M. GOODLIFFE
JACK C. PASHIN

A DISSERTATION

Submitted in partial fulfillment of the requirements
for the degree of Doctor of Philosophy
in the Department of Chemical & Biological Engineering
in the Graduate School of
The University of Alabama

TUSCALOOSA, ALABAMA

2012

ABSTRACT

The objective of this research project was to assist in the development of a simulation framework for assessment of CO_2 sequestration in geologic formations. An important part of this framework is centered on development of efficient models for phase equilibrium computations between CO_2 and Brines for a wide range of temperature and pressure. Besides accuracy of the models, time efficiency is extremely important from the standpoint of saving computational expenses. Therefore, thorough investigations have been carried out to model the phase equilibrium of CO_2 and Brine system over the temperature range 20 – 300 °C, and pressure range 1 – 600 bar using vapor state Equation of State (EoS), liquid state EoS, and Statistical Associating Fluid Theory (SAFT) in a time efficient manner.

To ensure that the system is modeled in a time efficient manner, different optimized models were used. First, a non-iterative scheme and new EoS for CO_2 have been proposed which give more than 1000 times speed up after integration with the simulator compared with other EoS's. To ensure that the phase equilibrium for super critical CO_2 is modeled in a time efficient manner, currently available liquid state models, such as UNIQUAC, LSG, NRTL, and GEM-RS were modified and the modified models reproduced literature data to within fair deviation. SAFT, which is a theoretically sound model, has also been modified to apply in the simulator. Furthermore, a new viscosity model that takes into consideration the effect of CO_2 dissolution and the geologic environment of interest was developed to model the viscosity of CO_2 and Brine. Double diffusive natural convection of CO_2 in brine saturated porous media was also investigated to show how CO_2 dissolves over time after injection in the geologic environment.

DEDICATION

This dissertation is dedicated to everyone who helped me and guided me throughout my PhD program. In particular, my family and close friends who stood by me always.

ACKNOWLEDGMENTS

I wish to express my sincerest gratitude to the individuals who supported and encouraged me both professionally and personally in the continuation of my PhD work. First and foremost, I would like to thank my direct supervisor, Dr. Eric S. Carlson. Admittedly, without his continued support, encouragement, patience and valuable advice, continuation of this work would not have been possible. Despite the fact that I had very little research experience from my Masters, his enthusiasm, inspiration and effort drove me to conduct this research in a highly professional manner.

I would also like to thank my committee members, Dr. Peter E Clark, Dr. Muhammad Ali Rob Sharif, Dr. Andrew M Goodliffe, and Dr. Jack C Pashin, for their co-operation and suggestions. I would also like to thank the Department of Chemical and Biological Engineering for providing me the opportunity to pursue my PhD degree.

I wish to express my deepest appreciation to my parents and other family members for their lifelong sacrifices and belief in me. Their consistent mental support, love and concern have played a significant role in my life's journey.

I would like to acknowledge Francis Dumkwu, colleague of our group for his cooperation and all my friends who made my stay very comfortable in the department and in Tuscaloosa, Alabama.

TABLE OF CONTENTS

LIST OF TABLES

TABLE **PAGE**

LIST OF FIGURES

FIGURE **PAGE**

CHAPTER ONE

INTRODUCTION

In recent years we have been experiencing irregularities in weather that have made changes in climatic conditions unpredictable. This phenomenon referred to as global warming is one of the most challenging environmental problems confronting the world. It is widely agreed to be caused by atmospheric greenhouse gases, such as CO_2 which is estimated to contribute approximately 50% of global warming, making the reduction of this greenhouse gas an important goal [1]. The global warming causes disruption in the chemical composition and physical dynamics of the Earth's atmosphere, leading to abnormal distribution of heat or energy around the atmosphere [2].

One way to protect the environment is to prevent the release of CO_2 into the atmosphere or decrease the amount of CO_2 released into the atmosphere by storing it in geological formations, such as depleted oil and gas reservoirs, coal beds, and deep saline aquifers. Low permeability, deep aquifers in sedimentary basins have been shown to be technically feasible as geologic sinks for sequestration of CO_2 and they are considered to be the largest potential for CO_2 storage [3]. Sequestration in geologic media not only does not depend on local climatic conditions, but also does not compete with agriculture, fishing, and other industries for land use. The technology of deep injection of CO_2 into geologic formations is well developed and well-practiced, mainly by the energy industry [4].

The engineering design and implementation of CO_2 sequestration in geologic formations is a complicated process in which many important safety-related decisions must be made before realistic tests can be conducted. Therefore, to sequester CO_2 into geologic formations, reliable numerical modeling is essential so that early design decisions and implementation can be data driven and safety countermeasures correctly incorporated. Mathematical models and numerical simulators are essential tools for addressing problems and questions that may arise in the context of CO_2 storage in the deep subsurface. They are important for the clarification of safety, feasibility, and economic issues. The objectives of current research are to develop simulation framework from the perspective of measuring the phase equilibria between CO_2 and Brine in

subsurface environment and to investigate how CO_2 will stabilize through the natural convection process in porous media over the years, as well as to understand the fate of carbon dioxide after being sequestered in geologic formations.

The cardinal parts of the simulation framework for CO_2 sequestration are centered on physical properties (density, viscosity, etc.) and phase equilibrium computations of CO_2 and Brine for a wide range of temperature and pressure. Besides having accurate models for phase equilibrium calculations, the time efficiency of the scheme is extremely important to save computational expenses. Therefore, the time efficiency of using vapor state Equation of State (EoS), liquid state EoS, and Statistical Associating Fluid Theory (SAFT) to model the phase equilibrium of CO_2 and Brine over the temperature range 20 – 300 °C, and pressure range 1 – 600 bar was thoroughly investigated.

To ensure that the system is modeled in a time efficient manner, different optimized models were used. First, a non-iterative scheme and a new EoS for CO_2 have been proposed which give more than 1000 times speed up after integration with the simulator compared with other EoS's. To model the phase equilibrium for super critical CO_2, currently available liquid state models, such as UNIQUAC, LSG, NRTL, and GEM-RS were modified and these modified models reproduced literature data to within fair deviation. Second, SAFT, which is a theoretically sound model, has also been modified to apply in the simulator for the said temperature and pressure ranges. Third, attempts have been made to develop efficient viscosity models suitable for simulating carbon dioxide sequestration in geological formations. The new models are simpler in form than the existing equations and are very accurate in reproducing literature data to within <1% deviation. Fourth, an extensive study is performed on double diffusion natural convection of CO_2 in brine saturated porous media to investigate how CO_2 will stabilize through the natural convection process over time after being sequestered into subsurface formations. The simulation results show that only 63% of CO_2 dissolved in the aquifer after 500 years have elapsed and changing reservoir shapes do not affect the results in any noticeable ways.

The studies conducted are presented in five different chapters. In Chapter One, a fully non-iterative technique for the phase equilibrium computation of CO_2 and brine is presented. In

addition, a new empirical equation for measuring CO_2 density is proposed. In Chapter Two, we demonstrated the application of liquid state models for the phase equilibrium calculations of super critical CO_2 and H_2O at high temperatures and pressures. The application of statistical associating fluid theory in simulation of geological sequestration of CO_2 is investigated in Chapter Three. We present new tools to calculate viscosity of H_2O, H_2O+NaCl, CO_2+H_2O, CO_2+H_2O+NaCl, and CO_2 + seawater in Chapter Four. The proposed equations are simpler than existing models in literature. We also discussed extensively the effects of CO_2 dissolution in viscosity measurement. Double diffusion natural convection of CO_2 in brine saturated porous media is investigated in Chapter Five. Additionally, we showed how CO_2 fronts spread in brine solution over time due to density driven convection for both concentration and temperature gradients.

CHAPTER TWO

†A Fully Non-iterative Technique for Phase Equilibrium and Density Calculations of CO_2+Brine System and an Equation of State for CO_2

Akand W. Islam, Eric S. Carlson
Department of Chemical and Biological Engineering
The University of Alabama, Tuscaloosa, AL 35487, USA

Abstract. Any mutual solubility or phase equilibrium calculations require iterations in order to attain desired convergence in fugacity measurements from which equilibrium compositions are obtained. In this monograph a fully non-iterative technique is approached for calculating phase equilibrium compositions of CO_2 in brine water and that of H_2O in CO_2 rich phase. As an essential part of this computation process, an empirical volume explicit Equation of State (EoS) for CO_2 with having only 8 parameters is presented. The volumetric data and calculated results of phase compositions using this EoS are compared with the literature values. They exhibit good agreement with less than 2% deviation. A modified scheme of CO_2+brine density calculation is also shown. More so, the manner in which this EoS can improve computational efficiency following the non-iterative technique with respect to other EoS's used in petroleum reservoir simulation is illustrated. This shows that the proposed technique can be even more than 1000 times faster than conventional phase equilibrium computations after integrating with numerical simulation of CO_2 flows in reservoir.

Key words: non-iterative, phase composition of CO_2, phase composition of H_2O, density, time efficient

†*Proceedings of the 37th Stanford Geothermal Workshop, Stanford University, 2012.*

2.1 Introduction: It is very well known that CO_2 is the major contributor to the global warming problem. Recent surveys of CO_2 in the atmosphere show average levels of 377 ppm, compared to 280 ppm in the pre-industrial revolution era (late 18^{th} century) [1] The burning of fossil fuels and other anthropogenic activities drive a dramatic increase in the concentration of atmospheric CO_2. Capturing CO_2 from major sources (like power industries) and its storage in deep geologic formations has been considered as a means to lessen global warming [2,3] Injection into saline aquifers, abandoned oil and gas reservoirs, and unmineable coal seams are among possible ways for this purpose. Injection into deep saline aquifers provides the highest storage capacity [4]. This type of aquifers can provide storage capacity of up to 11^{13} tons of CO_2 which is enough to store several hundred years of CO_2 emissions [3-5]. CO_2 will dissolve over time in the interstitial solution of the aquifer and in some formations it would slowly react with minerals to carbonates, which would lock up the CO_2 permanently. Suitable aquifers would have also a cap rock of low permeability to minimize CO_2 leakage [6].

Predicting the sequestration potential and long term behavior of man-made geologic reservoirs requires computations of pressure, temperature and composition properties of CO_2+Brine mixtures at depths where temperature is not that high (<100 °C), however, pressure may reach several hundred bar [7]. Thermodynamically, in this range, CO_2-rich gas or liquid phase and H_2O-rich liquid phase typically exists. The amount of H_2O in the CO_2-rich phase is quite small; it can fairly be approximated as pure CO_2. On the other hand, H_2O in the CO_2 rich phase displays very non-ideal mixing behavior [8-10].

The objective of this study is to develop a fully non-iterative algorithm for phase equilibrium calculations of CO_2+Brine system for efficient numerical simulations of CO_2 flows. Over the years several theoretical studies of CO_2+Brine system have been published [8-30]. These investigations cover elevated temperatures and pressures mostly relevant to the study of hydrothermal systems and fluid inclusions. Like any other phase equilibrium calculations, all the techniques proposed in these investigations require iterations for some property measurements (like vapor/liquid phase volume, fugacity etc.) in order to obtain desired convergence which might not be a big issue for phase equilibrium computations itself, is really cumbersome for numerical flow simulations, however. Spycher et al., [9] presented an approach to compute

mutual solubilities of pure H_2O and CO_2 in a temperature and pressure most relevant to the geologic sequestration of CO_2. Later they [31, 32] extended their models for moderately saline solutions up to 6M NaCl and for temperature and pressure range 12-300° C, 1-600 bar respectively. The techniques cannot be considered fully non-iterative, unless solving cubic EoS for obtaining CO_2 density (vapor, liquid or supercritical) through built-in function is ignored. In addition, computations of activity coefficients of CO_2 in mole fraction basis are not straight forward. One possible way to avoid solving cubic EoS in non-iterative manner is applying direct techniques like, classical Cardano's method, Nickall's approach [33], and so forth. However, experiences say that in many cases these direct techniques mislead in finding actual roots, especially of cubic EoS's. Moreover, selection of roots as vapor or liquid volume should be concerned. Another possible way of getting rid of root finding is to obtain an appropriate explicit volumetric correlation or EoS of CO_2 as a function of pressure and temperature. We have shown such type of EoS as an essential part of the proposed algorithm for phase equilibrium and density calculations of CO_2+brine system.

2.2 Calculations procedures: The theories and methodologies involved in calculations are discussed in order.

2.2.1 Solubility calculations of CO2 in aqueous phase*:* From thermodynamics relations chemical potential of CO_2 in aqueous phase and that in vapor phase can be shown as

$$\begin{aligned}\mu^V_{CO_2} &= \mu^V_{CO_2}(0) + RT\ln f_{CO_2} \\ &= \mu^V_{CO_2}(0) + RT\ln y_{CO_2}P + RT\ln\varphi_{CO_2}\end{aligned} \tag{1}$$

where, fugacity $f = Py\varphi$

$$\begin{aligned}\mu^l_{CO_2} &= \mu^l_{CO_2}(0) + RT\ln a_{CO_2} \\ &= \mu^l_{CO_2}(0) + RT\ln \mathrm{m}_{CO_2} + RT\ln\gamma_{CO_2}\end{aligned} \tag{1}$$

where, activity $a = \mathrm{m}\gamma$(molal basis)

As we know at equilibrium, $\mu^l_{CO_2} = \mu^V_{CO_2}$, from Eqns. (1) and (2) it can be written

$$\ln\frac{y_{CO_2}P}{\mathrm{m}_{CO_2}} = \frac{\mu^l_{CO_2}(0) - \mu^V_{CO_2}(0)}{RT} - \ln\varphi_{CO_2} + \ln\gamma_{CO_2} \tag{2}$$

In Eqn 3, reference number $\mu^{V}_{CO_2}(0)$ is set to zero. The fugacity coefficient of CO_2 in the vapor phase of CO_2+H_2O mixtures changes very negligible from that in pure CO_2 [16] and therefore φ_{CO_2} can be calculated from any suitable EoS for pure CO_2. Our proposed empirical EoS is of the following form

$$V_r = y_0 + \sum_{i=1}^{3} a_i e^{-b_i P_r} + c(T_r - T_{r0}) / P_r \tag{3}$$

Here V_r is the reduced volume related with $V_r = \frac{V}{V_c}$. V_c is not exactly critical volume but defined as $V_c = \frac{RT_c}{P_c}$. This EoS has only 8 parameters (y_0, a_1, b_1, a_2, b_2, a_3, b_3, c) which have to be estimated by the regression of volumetric data of CO_2 within certain temperature and pressure range. For our calculations, parameters that we have predicted are given in **Table 2.1**. These parameters have been predicted by the regression of CO_2 volumes within the range 20 – 40 °C and 1 – 400 bar extracted from MIT Carbon Capture and Sequestration Technologies (MIT-CCST) (http://sequestration.mit.edu/tools/index.html). We have used open source SciPy optimization package (http://www.scipy.org/doc/api_docs/SciPy.optimize.minpack.html) for data regression process.

Finally $\ln \varphi_{CO_2}$ is computed from the equation given in Ref [16].

Table 2.1: Parameters for Eqn. 1 [P in bar, T in K, V in m3/mol, supercritical volume 94x10-6 m3/mol].

parameters	subcritical volume	supercritical volume
y_0	-766.2884	0.1272
a_1	29.3030	0.0734
b_1	21.9128	0.5304215
a_2	8.5773	4.3925×10^{-3}
b_2	5.3415	44.8821
a_3	767.7692	5.9221
b_3	0.0130	4.6914
c	11.7854×10^{-10}	0.7745

$$\ln\varphi = Z - 1 - \ln Z + \frac{a_1 + a_2/T_r^2 + a_3/T_r^3}{V_r} + \frac{a_4 + a_5/T_r^2 + a_6/T_r^3}{2V_r^2} + \frac{a_7 + a_8/T_r^2 + a_9/T_r^3}{4V_r^4} + \frac{a_{10} + a_{11}/T_r^2 + a_{12}/T_r^3}{5V_r^5} + \frac{a_{13}}{2T_r^3 a_{15}} \times \left[a_{14} + 1 - (a_{14} + 1 + \frac{a_{15}}{V_r^2}) \times \exp\left(-\frac{a_{15}}{V_r^2} \right) \right] \quad (4)$$

Where compressibility factor,

$$Z = \frac{P_r V_r}{T_r} = 1 + \frac{a_1 + a_2/T_r^2 + a_3/T_r^3}{V_r} + \frac{a_4 + a_5/T_r^2 + a_6/T_r^3}{V_r^2} + \frac{a_7 + a_8/T_r^2 + a_9/T_r^3}{V_r^4} + \frac{a_{10} + a_{11}/T_r^2 + a_{12}/T_r^3}{V_r^5} + \frac{a_{13}}{T_r^3 V_r^2}\left(a_{14} + \frac{a_{15}}{V_r^2} \right)\exp\left(-\frac{a_{15}}{V_r^2} \right) \quad (5)$$

Parameters of Eqns 5 and 6 are obtained from [17]. For the sake of calculations of solubility of CO_2 in aqueous phase, mole fraction of CO_2 in vapor phase has been approximated as

$$y_{CO_2} = (P - P_{H_2O}) / P \tag{6}$$

Water saturation pressure P_{H_2O} is calculated from DIPPR correlations [34].

$$P_{H_2O} = \exp\left[A_1 + A_2 / T + A_3 \ln T + A_4 T^{A_5} \right] \tag{7}$$

This measured y_{CO_2} will be corrected in later subsection. In order to calculate γ_{CO_2} following functional relations have been used

$$\ln \gamma_{CO_2} = 2(\lambda_{CO_2-Na} m_{Na} + \lambda_{CO_2-Cl} m_{Cl}) + \zeta_{CO_2-Na-Cl} m_{Na} m_{Cl} \tag{8}$$

Values of interaction parameters λ, ζ are taken from [17]. Substituting Eqn 8 in Eqn 3 reduces to

$$\ln \frac{y_{CO_2} P}{\mathrm{m}_{CO_2}} = \frac{\mu^l_{CO_2}(0)}{RT} - \ln \varphi_{CO_2} + 2(\lambda_{CO_2-Na} \mathrm{m}_{Na} + \lambda_{CO_2-Cl} \mathrm{m}_{Cl}) + \zeta_{CO_2-Na-Cl} \mathrm{m}_{Na} \mathrm{m}_{Cl} \tag{9}$$

Here the term

$$\begin{aligned} \frac{\mu^l_{CO_2}(0)}{RT} &= c_1 + c_2 T + c_3 / T + c_4 T^2 + c_5 / (630 - T) + c_6 P + c_7 P \ln T \\ &\quad + c_8 P / T + c_9 P / (630 - T)^2 + c_{11} T \ln P \end{aligned} \tag{10}$$

The same parametric values for λ's in Eqn 10 reported in [17] are used for our calculations. Now every term in right hand sides of Eqn 9 are known, therefore, solubility of CO2 (m_{CO_2}) in molal basis can be computed. This molal CO_2 is converted to mole/mass fraction basis in following manner

$$x_{CO_2} = \mathrm{m}_{CO_2} / (1000 / 18.06 + \mathrm{m} + \mathrm{m}_{CO_2}) \tag{11}$$

$$X_{CO_2} = \mathrm{m}_{CO_2} \times 44.01 / (1000 + \mathrm{m} \times 58.44 + \mathrm{m}_{CO_2} \times 44.01) \tag{12}$$

2.2.2 Solubility calculations of H_2O in CO_2 phase: Pruess [35] developed following equation for y_{H_2O}

$$y_{H_2O} = \frac{(1 - B) 55.508}{(1/A - B)(\nu \mathrm{m}_{NaCl} + 55.508) + \nu \mathrm{m}_{NaCl} B} \tag{13}$$

$$y_{CO_2} = 1 - y_{H_2O} \tag{14}$$

where

$$A = \frac{K^0_{H_2O}}{\varphi_{H_2O} P} \exp\left(\frac{(P - P_0)\bar{V}_{H_2O}}{RT} \right) \tag{15}$$

and

$$B = \frac{\varphi_{CO_2} P}{55.508 \gamma_{CO_2} K^0_{CO_2(v)}} \exp\left(-\frac{(P - P_0)\bar{V}_{CO_2}}{RT} \right) \tag{16}$$

In Eqn 14, to calculate φ_{H_2O} we have used fugacity expression of H_2O in CO_2 given by King et al., [8] where they applied modified form of Redlich–Kwong EoS [36]. For the mixing rules we have assumed y_{H_2O} = 0, which is very reasonable as discussed earlier. This nullifies all the complexities of the application of cubic or any volume implicit EoS to calculate φ_{H_2O} in iterative manner. Equilibrium constants, $K^0_{H_2O}$, $K^0_{CO_2(v)}$ and $K^0_{CO_2(l)}$ are found from the references [9], and Spycher and Pruess [32]. It is very necessary to note that, at subcritical temperatures and pressures $K^0_{CO_2(v)}$ has to be replaced by $K^0_{CO_2(l)}$ if the conditions (1) T<31.2 °C, and (2) V_{CO_2} <94 cm^3/mol are simultaneously met. With necessary input of NaCl molality (m_{NaCl}), and from previous steps taking φ_{CO_2} and γ_{CO_2}, all the terms of right hand side in Eqn (14) are known and therefore mole fraction of H_2O in CO_2 rich phase y_{H_2O} can be calculated in a straight forward way.

2.2.3 Density calculations:

2.2.3.1 Density of H2O+CO2: Densities of H_2O+CO_2 (CO_2 saturated water density) have been measured from very simple correlations developed by Hebach et al. [37]. For above critical density of CO_2 they have presented

$$\rho_{H_2O+CO_2} = l_0 + l_1 P + l_2 T + l_3 P^2 + l_4 T^2 \tag{17}$$

and for lower than the critical density with respect to the CO_2 phase the expression is,

$$\rho_{H_2O+CO_2} = g_0 + g_1 P + g_2 T + g_3 P^2 + g_4 T^2 + g_5 PT + g_6 P^3 + g_7 T^2 P + g_8 T P^2 \tag{18}$$

2.2.3.2 Density of H2O+NaCl: To determine brine (H_2O+$NaCl$) density the correlation published by Anderson et al. [38] has been implemented. Their correlation can be expressed as (in terms of molar volume)

$$\ln(V_{sat}) = V_0 + V_1\tau^{0.325} + V_2\tau^{0.8915} + V_3\tau^{0.825} + V_4\tau + V_5\tau^2 + V_6\tau^3 + V_7\tau^4 + V_8\tau^5 \quad (19)$$

here

$$\tau = 1 - T / T_c(b)$$

$$V_0 = 4.0208 + 3.30x_{NaCl}$$

$$V_1 = -1.9286$$

$$V_2 = -34.214$$

$$V_3 = 20.1$$

$$V_4 = 15.45 - 4.7x_{NaCl}$$

$$V_5 = -1.2059$$

$$V_6 = .63339$$

$$V_7 = 0.0$$

$$V_8 = .47437$$

Finally the volume of compressed fluid is determined by

$$V_{H_2O+NaCl} = V_{sat}[1 + C(P - P_{sat}(b))] \quad (20)$$

where

$$C = \frac{-1.6534e^{-10}}{\tau^{1.25} - 5.6x_{NaCl}{}^{1.5} + 0.005}$$

The unknowns of Eqns 19 and 20 are x_{NaCl}, $T_c(b)$, and $P_{sat}(b)$. These represent mole fraction of NaCl, critical temperature, and saturated vapor pressure of brine solution respectively. For any molality (m) of NaCl it can be written,

$$x_{NaCl} = m / [1000 / 18.016 + m] \quad (21)$$

and

$$X_{NaCl} = m \times 58.448 / [1000 + m \times 58.448].$$

(22)

Battistelli et al. [39] showed a cubic equation of X_{NaCl} in terms of $T_c(b)$ which requires iterations in order to obtain correct $T_c(b)$. However experimental data [40-42] show, approximately up to 995 °K, $T_c(b)$ varies linearly with X_{NaCl}. Therefore we have used our own linear correlation of the form

$$T_c(b) = 975 X_{NaCl} + 373.15 \quad (23)$$

$P_{sat}(b)$ remains same as P_{H_2O} around up to 405 °K according to the figure ($P_{sat}(b)$ vs. T) reported by Battistelli et al. [39]. Hence we have used Eqn 8 for $P_{sat}(b)$.

2.3.3. Density of H_2O+NaCl+CO_2: To predict the density of aqueous phase with dissolved CO_2 following correlation can be used

$$\frac{1}{\rho_{aq}} = \frac{1 - X_{CO_2}}{\rho_{H_2O+NaCl}} + \frac{X_{CO_2}}{\rho_{CO_2}} \quad (24)$$

In this equation all quantities on the right hand side are known from previous calculations, and therefore we can easily calculate ρ_{aq} .

2.3 Results: First we will show feasibility tests of our presented EoS (Eqn 4) for CO_2. **Figures 2.1 and 2.2** show the comparisons of calculated CO_2 volumes with respect to the data obtained from MIT-CCST (MIT carbon Capture and Sequestration technology). As seen in Figures 1 and 2, it is clear that our EoS can calculate CO_2 volumes with acceptable accuracy. For any particular data point we have observed deviation is less than 2%. This EoS performs more accurately if the parameters are estimated from isothermal volumetric data ($T = T_r$ = constant). In this case, the number of parameters will be reduced to 7. Comparisons of literature isothermal volumetric data and our reproduced values are shown in **Appendix A**. These results show average absolute error 0.38% for subcritical region) and 0.0935% for supercritical region.

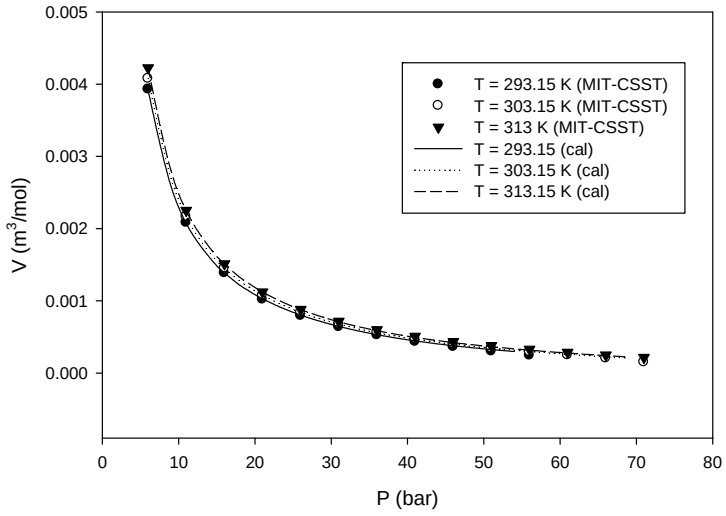

Figure 2.1: Comparison of calculated (by new EoS) CO_2 volume vs. data extracted from MIT-CSST at different temperatures (subcritical condition)

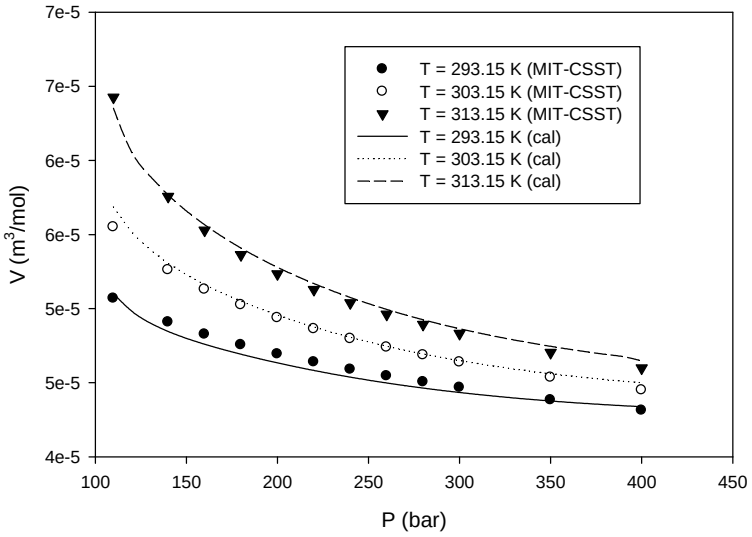

Figure 2.2: Comparison of calculated (by new EoS) CO_2 volume vs. data extracted from MIT-CSST at different temperatures (liquid and supercritical condition)

Numerous sources of solubility data of CO_2 in brine are available. However data at low temperatures and high pressures are scant. The data sources are addressed comprehensively in several review works and others [9, 17, 31, 32, 43-37]. Measured solubility data following our calculations schemes are shown in **Figures 2.3 and 2.4** against experimental values. Our discussed procedures reproduce experimental data close to or within experimental uncertainty. In many cases the experimental data themselves vary among the references at the same temperature and pressure (can be seen in figures 1.4 and 1.5). No literature data were found for comparing H_2O solubility in CO_2 rich phase for saline CO_2+H_2O solutions. Therefore **Figures 2.5 and 2.6** show comparisons between calculated and experimental values (for pure CO_2+H_2O solutions) along with only predicted values at different salinity levels.

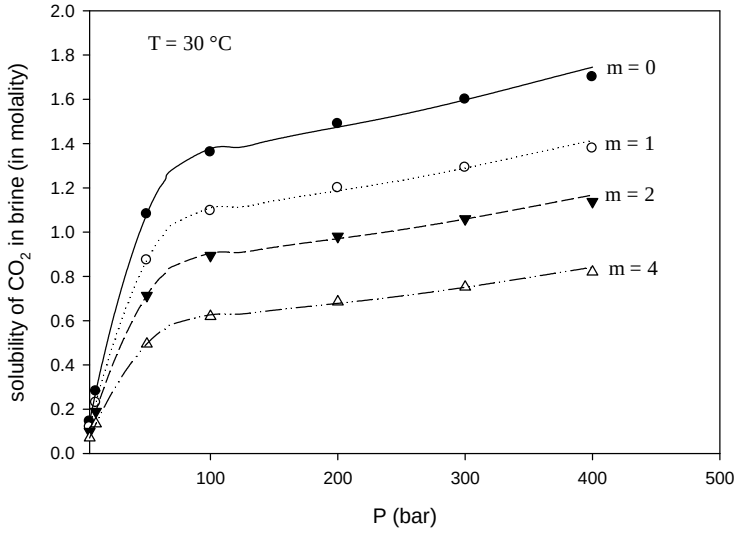

Figure 2.3: CO_2 solubility in brine at different pressures (symbols represent literature data from Enick and Klara [18]; lines represent calculated values)

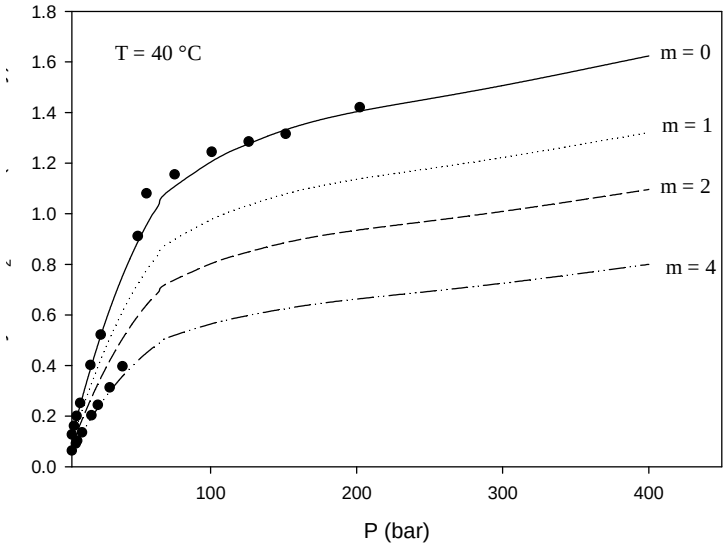

Figure 2.4: CO_2 solubility in brine at different pressures ((symbols represent literature data from Kim [45]; Rumph et al. [26]; Spycher and Pruess [9]), lines represent calculated values))

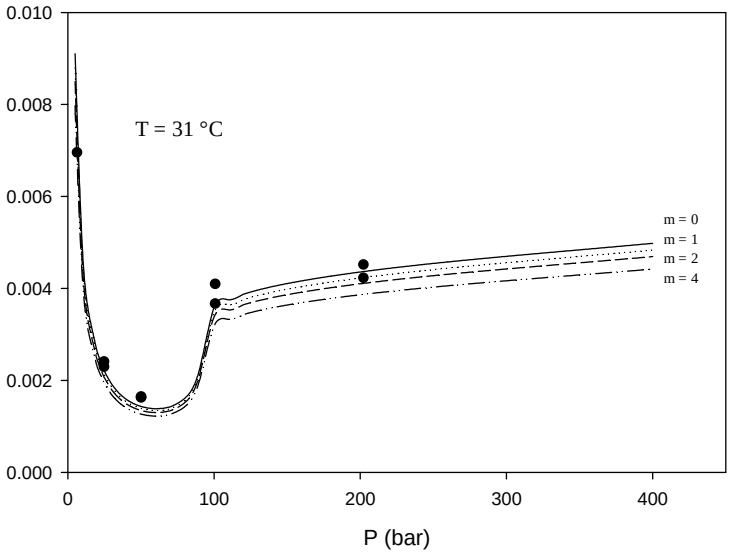

Figure 2.5: H_2O solubility in CO_2 rich phase at different pressures (symbols represent literature data from Spycher and Pruess [9] for m = 0; lines represent calculated values)

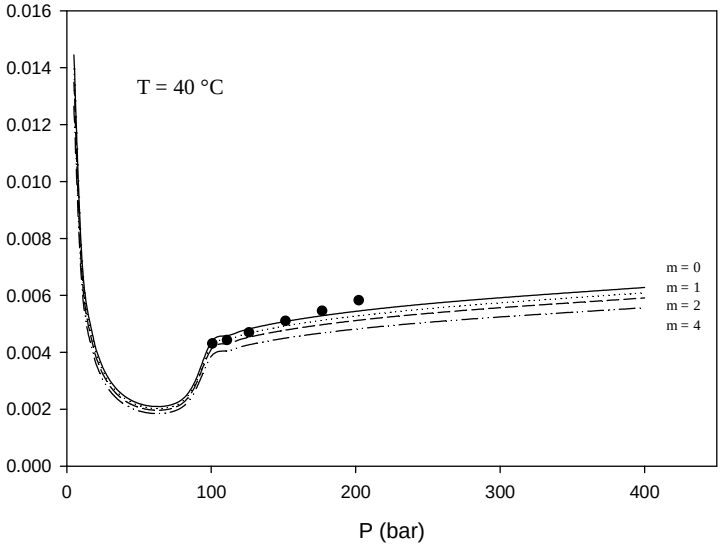

Figure 2.6: H_2O solubility in CO_2 rich phase at different pressures (symbols represent literature data from Spycher and Pruess [9] for m = 0; lines represent calculated values)

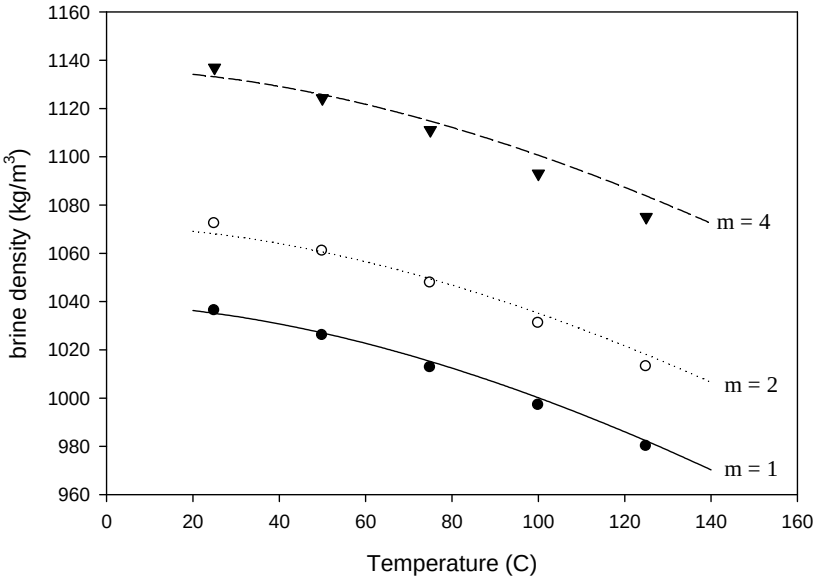

Figure 2.7: Brine densities at different temperatures ((symbols represent literature data from Potter and Brown [48]; lines represent calculated values))

Since we have also presented a slightly different approach of computing brine density, comparisons of literature (Potter and Brown, 1977) and calculated data are also shown in **Figure 2.7**. In this regard overall deviation is less than 1%.

Now we show how our proposed scheme will save huge computational expenses (cost per CPU time or memory). First we will show comparisons of computational time of CO_2+Brine phase equilibrium calculations following the algorithm that we have proposed using our EoS of CO_2 versus others EoS's which are frequently used. In this vein we have chosen Span and Wagner (S-P) [49], Duan et al. (D et al.) [16], and Redlich-Kwong (R-K) [36] EoS's for comparisons. In order to provide concrete example of how our scheme will save a significant amount of computational costs, we have integrated these phase equilibrium and density calculations with the numerical simulation of CO_2 flows in geologic reservoir. This simulation shows how CO_2 plume convects down in saline aquifers over the time period.

Table 2.2 shows the comparisons of execution times. Our proposed EoS performs 2.0 to 3.9 times faster phase equilibrium calculation on a notebook of average configuration (3 GB Ram, Dual-core CPU T4500 @ 2.3 GHz). In a fairly high configuration lab machine (11.57 GB Ram and i7-920 @ 2.67 GHz processor), this calculation is 1.1 to 3.4 times faster than others.

Table 2.2: Comparisons of execution time

computation time (CPU time in s)																
calculation of phase equilibrium only								after integrating with Simulator								
Notebook*				Lab workstation**				Notebook*					Lab workstation**			
our EoS	S-W	D et al.	R-K	our EoS	S-W	D et al.	R-K	Time steps	our EoS	S-W	D et al.	R-K	our EoS	S-W	D et al.	R-K
0.015	0.059	0.047	0.031	0.0099	0.034	0.012	0.011	1	2.1	1402.9	94.3	9.6	1.1	941.9	15.5	7.1
								120	200.5	162981.1	12201.9	1317.7	102.0	102452.2	1844.4	797.3

*3 GB Ram, Dual-core CPU T4500 @ 2.3 GHz
**11.57 GB, i7-920 CPU @ 2.67 GHz

However, the same calculation makes substantial execution time difference after combining with a reservoir simulator which may involve millions of cell grid calculations and a number of time steps. For a single time step calculation, other volume implicit EoS's make calculation 4.5 to 700.0 times slower with respect to our volume explicit EoS in a Notebook, and in lab machine these timing differences are 7.0 to 900.0 times. As the time stepping is increased in the simulator, these differences become more significant meaning our EoS may perform faster computations by 1000 times.

2.4 Conclusion: The algorithm mentioned does not involve any iteration or loop in the complete calculations process, while at the same time accuracy is not compromised. This will provide very helpful tools for designing complex reservoir simulators for which computational timing is extremely important. Our proposed volume explicit EoS for CO_2 is very simple and is comprised of less numbers of parameters compared to others found in literature. Upon estimating parameters, this EoS can reproduce CO_2 volume for given temperature and pressure within very reasonable deviation compared to the datum obtained from other sources. Integrating this scheme with numerical simulator of CO_2 flows can make calculations more than 1000 times faster and therefore will contribute to save huge computations costs.

2.5 Notations:

l = liquid phase

m = molality (mole NaCl per 1000 kg H_2O)

P = pressure (bar)

P_0 = reference pressure (1 bar)

P_c = critical pressure (73.88 bar)

P_r = reduced pressure (P/P_c)

R = universal gas constant (83.14472 bar.cm^3/mol/K)

T = temperature (K)

T_c = critical temperature (304.2 K)

T_r = reduced temperature (T/T_c)

T_{r0} = reference reduced temperature

V = vapor phase

V = volume (cm^3/mol)

V_c = critical volume of CO_2

$\bar{V}_{H_2O}$ = molar volume of liquid H_2O (18.1 cm^3/mol)

$\bar{V}_{CO_2}$ = molar volume of liquid CO_2 (32.6 cm^3/mol)

x = mole fraction in aqueous (H_2O rich) phase

X = mass fraction in aqueous (H_2O rich) phase

y = mole fraction in vapor (CO_2 rich) phase

Y = mass fraction in (CO_2 rich) vapor phase

φ = fugacity coefficient

$\rho_{H_2O+CO_2}$ = CO_2 saturated water density (mol/cm^3)

$\rho_{H_2O+NaCl}$ = brine density (mol/cm^3)

ν = stoichimetric number (2 for NaCl)

μ = chemical potential

$\mu^l_{CO_2}(0)$ = standard chemical potential of CO_2 in liquid phase in ideal solution of unit molality

$\mu^V_{CO_2}(0)$ = standard chemical potential of CO_2 in vapor phase in ideal gas when P = 1 bar

A_1, A_2, A_3, A_4, A_5 = constants for DIPPR correlation

l_0, l_1, l_3, l_4 = coefficients of the Eqn 17 taken from Hebach *et al.* (2004)

g_0, g_1, g_2, g_3, g_4, g_5, g_6, g_7, g_8 = coefficients of the equation of 18 taken from Hebach *et al.* (2004).

aq = aqueous

Eqn = Equation

Subscripts

sat = saturated

exp = experimental

cal = calculated

2.6 References:

[1] Houghton, J., Global Warming, *Rep Prog Phys., 68*, 1343-1403, 2005.

[2] Omerod, W.G., IEA Greenhouse Gas R&D Programme, Carbon Dioxide Disposal from Power Stations: IEA/GHG/SR3, 1994.

[3] Ormerod, B., Greenhouse Gas R&D Programme: Tech. Rep., IEAGHG/SR3-229, 1994.

[4] Piri, M., Prevost, J.H., and Fuller, R., Carbon Dioxide Sequestration in Saline Aquifers: Evaporation, Precipitation and Compressibility Effects: 4th Annual Conference on Carbon Capture and Sequestration DOE/NETL, Princeton University, Princeton, NJ 08544, 2005.

[5] Orr, F.M., Storage of Carbon Dioxide in Geologic Formations: paper SPE 88842, 90-97, 2004.

[6] Portier S., Rochelle, C., *Chemical Geology., 217*, 187-199, 2005.

[7] Saripalli, P., McGrail, P., *Energy convers mgmt., 43*, 185-198, 2004.

[8] King, M.B., Mubarak, A., Kim, J.D., Bott, T.R., *J Supercrit Fluids., 5,* 296-302, 1992.

[9] Spycher, N.F., Pruess, K., Ennis-King, J., *Geochim et Cosmochimi Acta, 67*, 3015-31, 2003.

[10] Spycher, N.F., Reed, M.H., *Geochim et Cosmochim Acta, 52*, 739-149, 1988.

[11] Barta, L., Bradley, D.J., *Geochim et Cosmochim Acta, 49*, 195-203, 1985.

[12] Bowers, T.S., Helgeson, H.C., *Geochim et Cosmochim Acta, 47*, 1247-1275, 1983.

[13] Cramer, S.D., The Solubility of Methane, Carbon dioxide and Oxygen in Brines From 0 to 300 C. Report of Investigations 8706. US Department of Energy, Bureau of Mines, 1982.

[14] Drummond, S.E., Boiling and Mixing of Hydrothermal Fluids: Chemical Effects on Mineral Precipitation, PhD Thesis, Pennsylvania State University, 1981.

[15] Duan, Z., Moller, N., Weare, H., *Geochim et Cosmochim Acta,* 59, 2869-2882, 1995.

[16] Duan, Z., Moller, N., Weare, J.H., *Geochim et Cosmochim Acta, 56*, 2605-2617, 1992.

[17] Duan, Z., Sun, R., *Chem Geology., 193*, 257-271, 2003.

[18] Enick, R.M., Klara, S.M., *Chem Eng Comm., 90,* 23-33, 1990.

[19] Harvey, A.H., Prausnitz, J.M., *AIChE J.*, *35*, 635-644, 1989.

[20] Li, Y., Nghiem, LX., *Can J Chem Eng., 64,* 486-496, 1986.

[21] Malinin, S.D., Kurovskaya, N.A., *Geokhym., 4,* 547-551, 1975.

[22] Malinin, S.D., Savelyeva, N.I., *Geokhym., 4,* 547-551, 1972.

[23] Masoudi, R., Tohidi, B., Danesh, A., Todd, A.C., *Fluid Phase Equilib., 215,* 163-174, 2004.

[24] Nesbitt, H.W., *Chem Geol., 43,* 319-330, 1984.

[25] Patel, N.C., Abovsky, V., Watansiri, S., *Fluid Phase Equilib., 185,* 397-405, 2001.

[26] Rumph, B., Nicolaisen, H., Ocal, C., Maurer, G., *J Sol Chem., 23,* 431-448, 1994.

[27] Shyu, G-S., Hanif, N.S.M., Hall, K.R., Eubank, P.T., *Fluid Phase Equilib., 130,* 73-85, 1997.

[28] Soreide, I., Whitson, C.H., *Fluid Phase Equilib., 77,* 217-240, 1992.

[29] Sorensen, H., KS Pedersen, K.S., Christinsen, P.L., *Org Geochem., 33*, 635-42, 2002.

[30] Zuo, Y., Guo, T.M., *Chem Eng Sci., 46,* 3251-3258, 1991.

[31] Spycher, N., K Pruess, K., *Geochim et Cosmochim Acta, 69,* 3309-20, 2005.

[32] Spycher, N., Pruess, K., *Transp Porous Med., 82,* 173-96, 2010.

[33] Nickalls, R.W.D., *The Mathmatical Gazette., 77,* (1993) 354-359.

[34] Daubert, T.E., Danner, R.P., Physical and Thermodynamic Properties of Pure Chemicals. Data Compilation. Taylor and Francis, Washington D.C, 1992.

[35] Pruess, K., ECO2N: A TOUGH2 Fluid Property Module for Mixtures of Water, NaCl, and CO_2. Earth Science Division, Lawrence Berkely National laboratory, Berkely, CA, 2005.

[36] Redlich, O., Kwong, J.N.S., *Chem Rev., 44,* 233-244, 1949.

[37] Hebach, A., Oberchof, A., Dahmen, N., *J Chem Eng Data., 49,* 950-953, 2004.

[38] Anderson, G., Probst, A., Murray, L., Butler, S., An Accurate PVT Model for Geothermal Fluids as represented by H_2O-CO_2-NaCl Mixtures. Seventeenth Workshop on Geothermal Reservoir Engineering, Stanford University, Stanford, CA, 1992.

[39] Battistelli, A., Calore, C., Pruess, K., *Geothermics.*, *26,* 737-764, 1997.

[40] Bischoff, J.L., Pitzer, K.S., *Am J Sci., 289,* 217-248, 1989.

[41] Sourirajan, S., Kennedy, G.C., *Am J Sci., 260,* 115-141, 1962.

[42] Tanger, J.C., Pitzer, K.S., *Geochim et Cosmochim Acta, 53,* 973-987, 1989.

[43] Diamond, L.W., Akinfiev, N.N., *Fluid Phase Equilib., 208,* 265-290, 2003.

[44] Kiepe, J., Horstmann, S., Fischer, K., Ghmehling. J., *Ind Eng Chem Res., 41,* 4393-4398, 2002.

[45] Kim, Y., *J Mech Sci Tech., 21,* 799-804, 2007.

[46] Li, D., Duan, Z., *Chem Geol., 244,* 730-751, 2007.

[47] Yuanhui, J., Xiaoyan, J., Xin, F., Chang, L., Linghong, L., Xiaohua, L., *Chin J Chem Eng., 15,* 439-448, 2007.

[48] Potter, R.W., Brown, D.L., The Volumetric Properties of Aqeous Sodium Chloride solutions from 0 to 500 C at Pressures up to 2000 bars Based on a Regression of Available Data in the Literature. USGS Bulletin 1421 C, Washington DC, 1977.

[49] Span, R., Wagner, W., *J Phys Chem Ref Data., 25,* 1509-1596, 1996.

2.7 Appendix:

Table A1 shows comparative study between literature and calculated CO_2 volumes.

Table A1: Comparison of CO_2 volumes extracted from MIT-CSST and the data calculated by our EoS (T = 30 °C)

P [bar]	V_{exp} (MIT-CSST) [m^3/mol]	V_{cal} [m^3/mol]	average absolute error (AAE) (%)	Parameters of Eqn 4
5.0000	4.9178e-3	4.9177e-3		
10.0000	2.3961e-3	2.3965e-3		
15.0000	1.5541e-3	1.5526e-3		
20.0000	1.1319e-3	1.1342e-3		
25.0000	8.7742e-4	8.7764e-4		y_0 = -1.2278e+3
30.0000	7.0661e-4	7.0497e-4		a_1 = 3.4274e+1
35.0000	5.8345e-4	5.8206e-4		b_1 = 26.3569
40.0000	4.8982e-4	4.8993e-4	0.385	a_2 = 1.0498e+1

45.0000	4.1558e-4	4.1706e-4		b_2 = 6.8620
50.0000	3.5454e-4	3.5629e-4		a_3 = 1.2299e+3
55.0000	3.0250e-4	3.0312e-4		b_3 = 1.4153e-3
60.0000	2.5625e-4	2.5473e-4		c = 0.0
65.0000	2.1243e-4	2.0934e-4		
70.0000	1.6348e-4	1.6584e-4		
80.0000	6.2664e-5	6.2585e-5		
90.0000	5.9069e-5	5.9230e-5		
100.0000	5.6983e-5	5.6990e-5		
110.0000	5.5500e-5	5.5415e-5		
120.0000	5.4346e-5	5.4244e-5		
130.0000	5.3402e-5	5.3323e-5		
140.0000	5.2601e-5	5.2560e-5		
150.0000	5.1907e-5	5.1903e-5		
160.0000	5.1293e-5	5.1320e-5		y_0 = 0.12354036
170.0000	5.0744e-5	5.0790e-5		a_1 = 4.7964
180.0000	5.0246e-5	5.0302e-5		b_1 = 0.00571466
190.0000	4.9791e-5	4.9848e-5	0.0935	a_2 = 0.3245
200.0000	4.9373e-5	4.9424e-5		b_2 = 0.6075
210.0000	4.8985e-5	4.9026e-5		a_3 = 1.33485463
220.0000	4.8624e-5	4.8652e-5		b_3 = 3.9744
230.0000	4.8286e-5	4.8299e-5		c = 0.0
240.0000	4.7969e-5	4.7967e-5		
250.0000	4.7669e-5	4.7653e-5		
260.0000	4.7386e-5	4.7356e-5		
270.0000	4.7117e-5	4.7077e-5		
280.0000	4.6862e-5	4.6812e-5		
290.0000	4.6618e-5	4.6563e-5		
300.0000	4.6385e-5	4.6327e-5		
310.0000	4.6162e-5	4.6105e-5		
320.0000	4.5949e-5	4.5895e-5		
330.0000	4.5744e-5	4.5696e-5		
340.0000	4.5546e-5	4.5509e-5		
350.0000	4.5356e-5	4.5332e-5		
360.0000	4.5172e-5	4.5165e-5		
370.0000	4.4995e-5	4.5007e-5		
380.0000	4.4824e-5	4.4858e-5		
390.0000	4.4658e-5	4.4717e-5		
400.0000	4.4498e-5	4.4584e-5		

CHAPTER THREE

†Activity Coefficient Models for the Phase Equilibrium Calculations of Supercritical CO_2 and H_2O at High Temperatures and Pressures

Akand W. Islam, Eric S. Carlson
Department of Chemical and Biological Engineering, The University of Alabama,
Tuscaloosa, AL 35487, USA

Abstract: There are numerous models available to compute phase equilibrium compositions of supercritical CO_2 and H_2O at higher temperatures and pressures. All of these models are based on equation of state (EoS), developed semi-empirically or fully empirically, perform VLE (vapor-liquid equilibrium) type calculations. In this monograph a different approach has been shown where liquid state models (LSM) are used following fully LLE (liquid-liquid equilibrium) flash type computational methods in order to obtain phase compositions (solubility of CO_2 in H_2O rich phase and that of H_2O in CO_2 rich phase) over the pressures and temperatures ranges. Four LSM (two two-parameter models UNIQUAC and LSG, and two three-parameter models NRTL and GEM-RS) are investigated. Since their original forms are not appropriate enough to represent the literature values, modifications of binary interaction parameters of these models have been carried out introducing both pressure and temperature dependent functions. These modified models are able to re-generate the phase compositions values within 2-7% deviations. Further investigations show that LLE calculations are more time efficient than VLE computations, meaning our approach can save huge computational expenses for the numerical simulations of CO_2 flows in a reservoir. Comparisons of time efficiency of these modified models with respect to other methods like, Redlich-Kwong, Span and Wagner have been shown.

Key words: Liquid state model, phase composition of CO_2, phase composition of H_2O, time efficient

†*Geothermal Resources Council Trans., 2012, 36, 855-861, 2012.*

3.1 Introduction: Carbon dioxide (CO_2) is the most important compound currently affecting the stability of Earth's climate [1-4]. Since more than a decade many studies have been conducted to review the feasibility of CO_2 geologic storage as mitigation measure to control rising CO_2 emissions. Injection of CO_2 into geologic media gives rise to interphase mass transfer of both CO_2 and water (H_2O). Geologic media may include saline aquifers, depleted oil/gas reservoirs, coal formations and so forth [5,6]. The solubility of supercritical CO_2 and H_2O in either phase has noticeable inference for long-term carbon sequestration. Accurate prediction of their solubilities over a wide temperature (T) and pressure (P) range is very important for the analysis of fluid inclusion data [7,8], studying carbon cycle [9,10], and so on. Furthermore, the knowledge of the phase equilibrium between CO_2 and H_2O at higher temperatures and pressures is required in industrial production, and chemical and environmental engineering applications, like, CO_2 related enhanced oil and gas recovery, supercritical fluid technology, designing separation columns etc [11-16].

Several models have been proposed to calculate phase equilibrium between CO_2 and H_2O at high temperatures and pressures [17-29]. All of these models are either based on EoS developed semi-empirically, like Peng-Robinson [17], Redlich-Kwong [24], and so on, or developed fully empirically, e.g., Span and Wagner [26], Duan and Sun [20], and so on. No attempts were found so far which applied liquid state models [30-32] directly in this maneuver. However, some investigations have been observed where liquid state models were used in mixing rules [33-39]. These modified mixing rules were based on the ideas by Huron and Vidal [40], and Wong and Sandler [41].

Above the critical temperature and pressure, components pose liquid-like densities, therefore excess Gibbs energy (G^{ex}) or liquid state models should be applicable to the phase equilibrium calculations of such components. Present study is based upon this hypothesis. In this study an attempt has been made to perform phase equilibrium computations of CO_2 and H_2O at high temperatures (=>90 °C) and pressures (=>300 bar) using only activity coefficient models and applying LLE flash type algorithm. Two two-parameter models (UNIQUAC and LSG) and two three-parameter models (NRTL and GEM-RS) have been investigated. Original forms of these models are not appropriate enough for phase calculations over a pressure and temperature range

since it is assumed that liquid densities are not varied with pressures and with temperatures densities change is negligible. This phenomenon is true for pure liquid components. However, at higher temperatures and pressures although supercritical CO_2 behaves like liquid, there are still densities changes with temperatures and pressures which cannot be over looked. Therefore, modifications of these models are obvious in order to include pressure and temperature variation terms. The objective of this work is to modify the mentioned models in such a way and then predict the appropriate parameters to regenerate the literature phase compositions data within fair deviation.

3.2 Liquid State Models: For better understanding brief introduction of the original form of the said models are discussed below:

3.2.1 UNIQUAC Model

The UNIQUAC model [30] is derived by phenomenological arguments based on a two-fluid theory and it allows local compositions to result from both size and energy differences between the molecules in the mixture. The expression for G^{ex} is given by

$$\frac{G^{ex}}{RT} = \frac{G^{ex}(combinatorial)}{RT} + \frac{G^{ex}(residual)}{RT} \tag{1}$$

Here R is the universal gas constant. The first term in the above expression accounts for molecular size and shape differences and the second term accounts largely for energy differences. For m number of components

$$\frac{G^{ex}(combinatorial)}{RT} = \sum_{j=1}^{m} x_i \ln \frac{\varphi_j}{x_j} + \frac{z}{2} \sum_{j=1}^{m} x_j q_j \ln \frac{\theta_j}{\varphi_j} \tag{2}$$

$$\frac{G^{ex}(residual)}{RT} = -\sum_{j=1}^{m} q_j x_j \ln\left(\sum \theta_j \tau_{ij}\right) \tag{3}$$

where

r_i = volume parameter for species i

q_i = surface area parameter for species i

θ_i be area fraction of species i given by

θ_i=

$$x_i q_i / \sum x_j q_j \tag{4}$$

φ_i be volume fraction of species *i* given by

$$\varphi_i = x_i r_i / \sum x_j r_j \tag{5}$$

binary interaction parameter,

$$\ln \tau_{ij} = \frac{\left(u_{ij} - u_{jj}\right)}{RT} \tag{6}$$

u_{ij} being the average interaction energy between *i-j* and *z* being the average coordination number, usually taken to be 10. This u_{ij} and u_{ji} have to be estimated from experimental data reductions. Expression of activity coefficient is given by

$$\ln \gamma_i(combinatorial) = \ln \frac{\varphi_i}{x_i} + \frac{z}{2} q_i \ln \frac{\theta_i}{\varphi_i} + l_i - \frac{\varphi_i}{\theta_i} \sum_j x_j l_j \tag{7}$$

$$\ln \gamma_i(residual) = q_i \left[1 - \ln\left(\sum_j \theta j \tau_{ji} \right) - \sum_j \frac{\theta_j \tau_{ji}}{\sum_k \theta_k \tau_{kj}} \right] \tag{8}$$

$$\ln \gamma_i = \ln \gamma_i(combinatorial) + \ln \gamma_i(residual)$$

The UNIQUAC model is essentially a two-parameter model and is of considerable use because of its wide applicability to various liquid solutions.

3.2.2 LSG Model

This model is based on Guggenheim's quasi-lattice model and Wilson's local composition concept proposed by Vera et al [32]. Like UNIQUAC this has also combinatorial and residual parts, although the equation is similar but not identical to UNIQUAC. Final expression of activity coefficient is given by

$$\ln \gamma_i = 1 - \frac{\varphi_i}{x_i} + \ln \frac{\varphi_i}{x_i} + \frac{z q_i}{2} \left[\frac{\varphi_i}{\theta_i} - \sum_k \frac{\theta_k \tau_{ki}}{\sum_j \theta_j \tau_{kj}} + \ln \frac{\theta_i / \varphi_i}{\sum_k \theta_k \tau_{ik}} \right] \tag{9}$$

where

r_i = volume parameter for species i

q_i = surface area parameter for species i

θ_i and φ_i are determined from Eqs. 4 and 5

$$\ln \tau_{ij} = \frac{u_{ij}}{RT}$$

Here like UNIQUAC, u_{ij} and u_{ji} are the binary interaction parameters.

3.2.3 NRTL Model

This model was developed by Renon and Prausnitz [31] based on two-liquid theories. This is different from the UNIQAC and two-parameter model. This model does not contain combinatorial and residual parts separately. For a solution of *m* components, the NRTL equation is,

$$\frac{g^E}{RT} = \sum_{i=1}^{m} x_i \frac{\sum_{j=1}^{m} \tau_{ji} G_{ji} x_j}{\sum_{l=1}^{m} G_{li} x_l} \tag{10}$$

where

$$\tau_{ji} = \frac{u_{ji}}{RT}$$

Here u_{ij} and u_{ji} are the binary interaction parameter between component *i* and *j*, and non-randomness factor is related by,

$$G_{ji} = \exp(-\alpha_{ji} \tau_{ji})$$

where

$$\alpha_{ji} = \alpha_{ij}$$

Finally the activity coefficient for any component *i* is given by

$$\ln \gamma_i = \frac{\sum_{j=1}^{m} \tau_{ji} G_{ji} x_j}{\sum_{l=1}^{m} G_{li} x_l} + \sum_{j=1}^{m} \frac{x_j G_{ij}}{\sum_{l=1}^{m} G_{lj} x_l} \left(\tau_{ij} - \frac{\sum_{r=1}^{m} x_r \tau_{rj} G_{rj}}{\sum_{l=1}^{m} G_{lj} x_l} \right) \tag{11}$$

In this expression u_{ij}, u_{ji}, and α_{ij} ($\alpha_{ji} = \alpha_{ij}$) are predicted from data regression.

3.2.4 GEM-RS Model

This is the same as the LSG model but contains the third interaction parameters like the NRTL model. The method of obtaining *r* and *q* values is the same for the LSG and GEM-RS model. Methods of obtaining these volume and surface parameters are discussed by Vera and his co-workers [32]. Activity coefficient is given by

$$\ln\gamma_i = 1-\frac{\varphi_i}{x_i}+\ln\frac{\varphi_i}{x_i}+\frac{zq_i}{2}\left[\frac{\varphi_i}{\theta_i}-\sum_k\frac{\theta_k\tau_{ki}}{\sum_j\theta_j\tau_{kj}}+\ln\frac{\theta_i/\varphi_i}{\sum_k\theta_k\tau_{ik}}\right]\frac{zq_i}{2}\sum_{k\neq i}\pi_{ik}\theta_k \qquad (12)$$

$$-\frac{zq_i}{2}\sum_{k=1}\sum_{l>k}\pi_{kl}\theta_k\theta_l$$

where

r_i = volume parameter for species i

q_i = surface area parameter for species i

θ_i and φ_i are determined from Eqs. 6 and 7

$$\ln\tau_{ij}=\frac{u_{ij}}{RT}$$

$$\pi_{ij}=\frac{\lambda_{ij}}{RT}$$

Here u_{ij}, u_{ij}, and λ_{ij} ($\lambda_{ij}=\lambda_{ji}$) are the predictable interaction parameters.

3.3 Modification of the Models: From previous description it can be clearly seen that original form of these models may perform well at isothermal conditions or at best at little temperature range, and the activity coefficient does not vary with pressures. Some attempts have been made to apply these models over a wide temperature range. Adding temperature dependent terms (linear, quadratic, so on) with binary interaction parameters (BIP) make them flexible to reproduce the experimental data over the temperature range [42-45]. Islam and Kabadi [46] have reviewed these studies.

However, to make the said models suitable for calculations over both the temperature and pressure range reduced temperature (T_r) and reduced pressure (P_r) have been proposed to relate with the BIP in the following manner

$$u_{ij} = A_{ij} + B_{ij}T_r^{b_{ij}} + C_{ij}P_r^{c_{ij}} + K_{ij} \times T_r \times P_r \tag{13}$$

Third interaction parameter of NRTL and GEM-RS have also been co-related in the same way,

$$\alpha_{ij} \text{ or } \lambda_{ij} = D_{ij} + E_{ij}T_r^{e_{ij}} + F_{ij}P_r^{f_{ij}} + L_{ij} \times T_r \times P_r \tag{14}$$

These modified relations for BIP are consistent with parametric nature of the original models (i.e., $u_{ii} = 0$, $\alpha_{ij} = \alpha_{ji}$, $\lambda_{ij} = \lambda_{ji}$) [47]. After this modification, total number of parameters of UNIQUAC and LSG are 12, and that of NRTL and GEM-RS are 18.

3.4 Parameters Estimation: Parameters of the Eqs 13 and 14 for all four models have been predicted in a heuristic manner through regression of literature data. In each case the objective function was set as

$$F_i(\text{obj}) = \sum_k^{N_k} \sum_i^{N_i} \frac{1}{N} \frac{F_{i,k}(\text{exp}) - F_{i,k}(\text{cal})}{F_{i,k}(\text{exp})} \tag{15}$$

where

$$N = N_K * N_i \tag{16}$$

Here N = number of data points, N_k = total number of property, k = 2 [k = 1 indicates solubility of CO_2 in water, and k = 2 indicates solubility of H_2O in CO_2]

In this data reduction process, data (solubility of CO_2 in H_2O and that of H_2O in CO_2) from Spycher and Pruess [27], and Duan and Sun [20] were used as experimental (exp) values and calculated (cal) data were generated using LLE (liquid-liquid equilibrium) flash calculation shown in **Figure 3.1**. Open source SciPy optimization package (http://docs.scipy.org/doc/scipy/reference/optimize.htm) was used for regressing the data. For any kind of optimization scheme initial guess values of the parameters is extremely important since no optimization package will be able to give best fitted parameters for any random initial values. Therefore we had to follow a trial and error process in order to get appropriate initial values of all parameters. First we regressed two solubility data (at constant T and P) to estimate two parameters by giving known parameter values of a known system [48] as the guess values. These two predicted values along with another two parameters with some small random values were

used as the next guess values to obtain four parameters for four solubility data (at constant *T*, different *P*'s). Thereafter these four parameters values were used to get best fitted four parameters (at different *T*'s, different *P*'s). These best fitted four parameters including another two parameters with small values were used as the initial values to find corrected six parameters for six solubility data (at different *T*'s, different *P*'s). This process was continued until we obtained the best fitted parameters of all mentioned modified models regressing the whole data set.

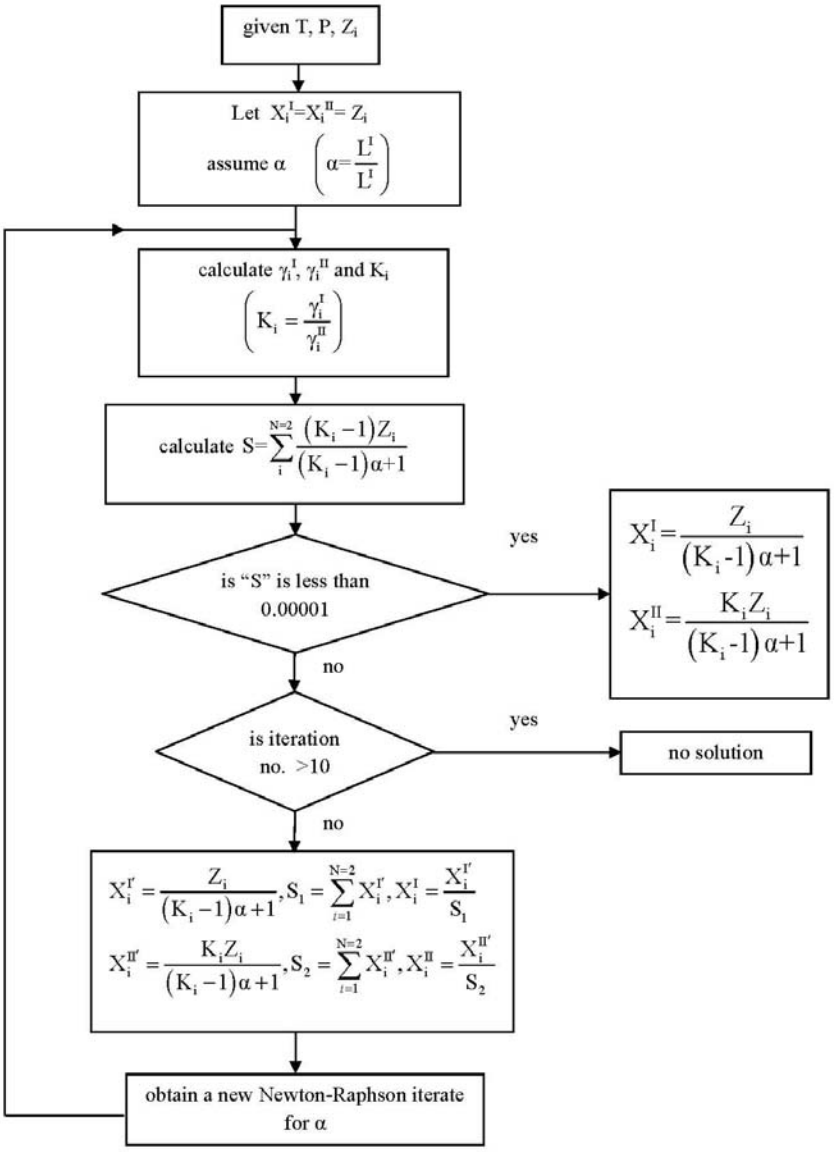

Figure 3.1: Flowchart of LLE flash calculation

3.5 Results and Discussion: After successful data reduction process, coefficients which give optimum results for said models are reported in **Table 3.1**. Comparisons of calculated results with respect to literature data by these best fitted parameters are shown in **Table 3.2**.

Table 3.1: List of parameters of Eqs 13 and 14

parameters	Two-parameter models		parameters	Three-parameter models	
	UNIQUAC	LSG		NRTL	GEM-RS
A_{12}	14.934	270.34	A_{12}	-651.228	3.143
A_{21}	2087.31	-4.565	A_{21}	2993.045	173.29
B_{12}	499.71	-71.735	B_{12}	1627.507	-60.16
B_{21}	-1136.96	36.49	B_{21}	-1618.917	164.02
b_{12}	1.11	3.38	b_{12}	1.215	2.838
b_{21}	1.02	4.58	b_{21}	1.215	2.838
C_{12}	-19.5	5.504	C_{12}	14.870	176.86
C_{21}	-0.1003	-1.1	C_{21}	-393.524	-50.398
c_{12}	0.2534	1.32	c_{12}	0.230	7.31E-02
c_{21}	1.3098	-5.36	c_{21}	0.230	7.31E-02
K_{12}	-12.843	-3.54	K_{12}	-8.282	0.966
K_{21}	4.723	-7.18	K_{21}	-0.4976	-5.143
			D_{12}	0.1827	-18.95
			E_{12}	4.975E-05	339.66
			e_{12}	12.024	-0.997
			F_{12}	-2.343E-03	9.243E-02
			f_{12}	0.685	6.57E-02
			L_{12}	-6.305E-03	1.139

Table 3.2 Comparisons of results among four models

	Two-parameter models		Three-parameter models	
	UNIQUAC	LSG	NRTL	GEM-RS
temperature range (°C)	90-250	90-250	90-250	90-250
pressure range (bar)	300-1000	300-1000	300-1000	300-1000
AAE* (%)	6.85	6.98	1.98	5.07

*AAE (average absolute error) = $\frac{\sum_{k}^{N_k}\sum_{i}^{N_i} \mathrm{err}_{i,k}}{N}$

where

$$N=N_K*N_i$$

From **Table 3.2** it can be said that the proposed modified liquid state models can represent the data fairly well within the maximum deviation 7%. Among these models NRTL shows best results exhibiting overall 1.98% deviation whereas LSG shows least preferable results performing 6.98% deviation. It is also observed that three-parameter models (NRTL and GEM-RS) are superior to two-parameter models (UNIQUAC and LSG). This may be due to the fact that the third parameter of NRTL and GEM-RS give them better flexibility to fit the data over the two-parameter models, UNIQUAC and LSG. This finding is similar like the study by Islam et al., [48] where they applied these four models to a highly non-ideal ternary liquid system Hexane-Butanol-Water [49]. This means supercritical CO_2+H_2O also behaves like a highly non-ideal liquid-liquid system.

Figures 3.2a-3.2f show comparative results of different isotherms. In these figures x_{CO2} represent solubility of CO_2 in H_2O and y_{H2O} denotes that of H_2O in CO_2. Symbols stand for literature data. These figures clearly depict, using liquid state models, that it is possible to obtain representative phase compositions of CO_2 in H_2O at higher temperatures and pressures within data uncertainty. Moreover, LLE flash computation tool where these models are used is more time efficient than VLE (vapor-liquid-equilibrium) calculations. For instance, **Table 3.3** shows comparisons of computation time of LLE calculations against that of VLE where Redlich-Kwong (R-K), Duan et

al., [50] [D et al.], Span and Wagner [26] [S-W], and finally our own recently proposed EoS [51] were used. The comparisons that are shown were executed in two types of machine; one is of average configuration Notebook (3 GB Ram, Dual-core CPU T4500 @ 2.3 GHz Notebook) and another one is of comparatively high-end configuration lab machine (11.57 GB Ram, i7-920 CPU @ 2.67 GHz Lab workstation). LLE calculations can be 8 to 15 times faster than that of VLE in a regular Notebook whereas in a lab machine these differences can be 4 to 12 times based upon the EoS type used. Since NRTL shows better representative values than others, this LSM was used to produce these comparisons. These little timing differences can make timing variations of 1000 times after integrating with numerical simulations of CO_2 flows [51]. This results in significantly more computational efficiency.

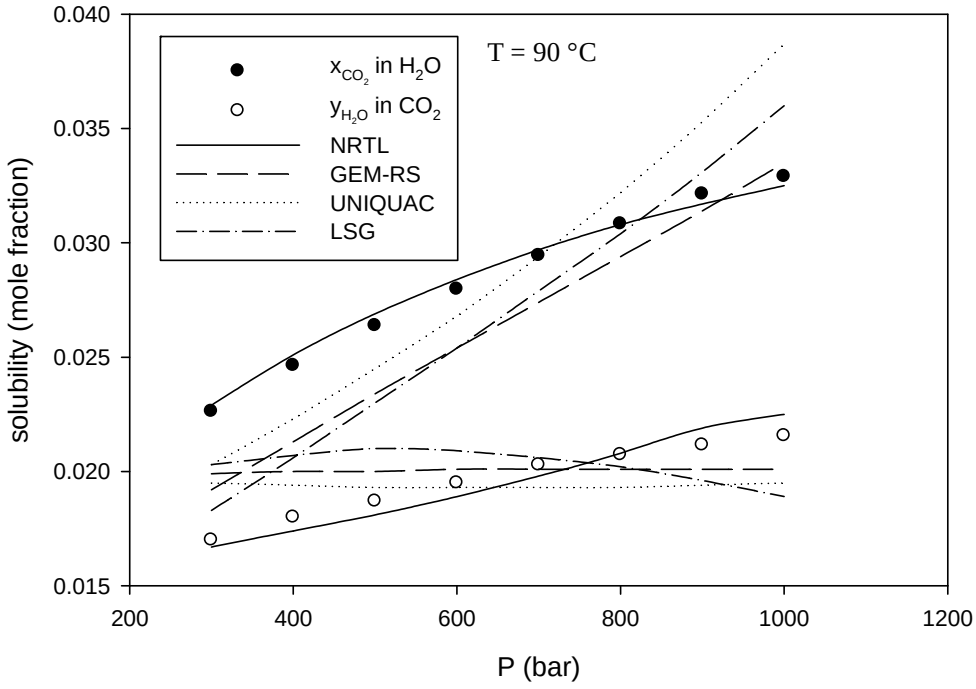

(a)

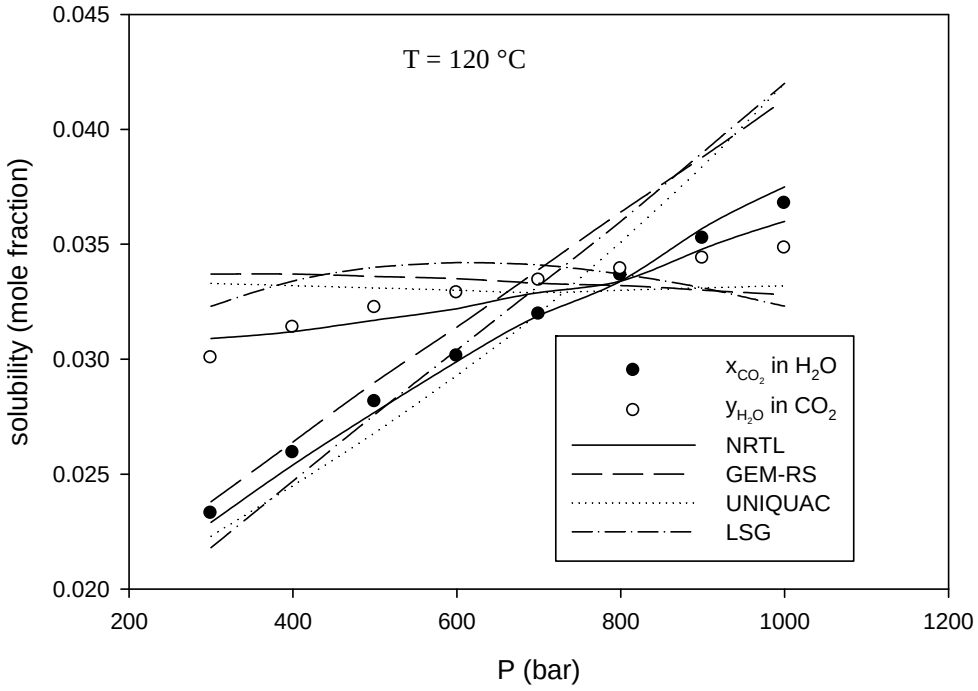
T = 120 °C
solubility (mole fraction)
P (bar)
0.045
0.040
0.035
0.030
0.025
0.020
200
400
600
800
1000
1200
x_{CO_2} in H_2O
y_{H_2O} in CO_2
NRTL
GEM-RS
UNIQUAC
LSG

(b)

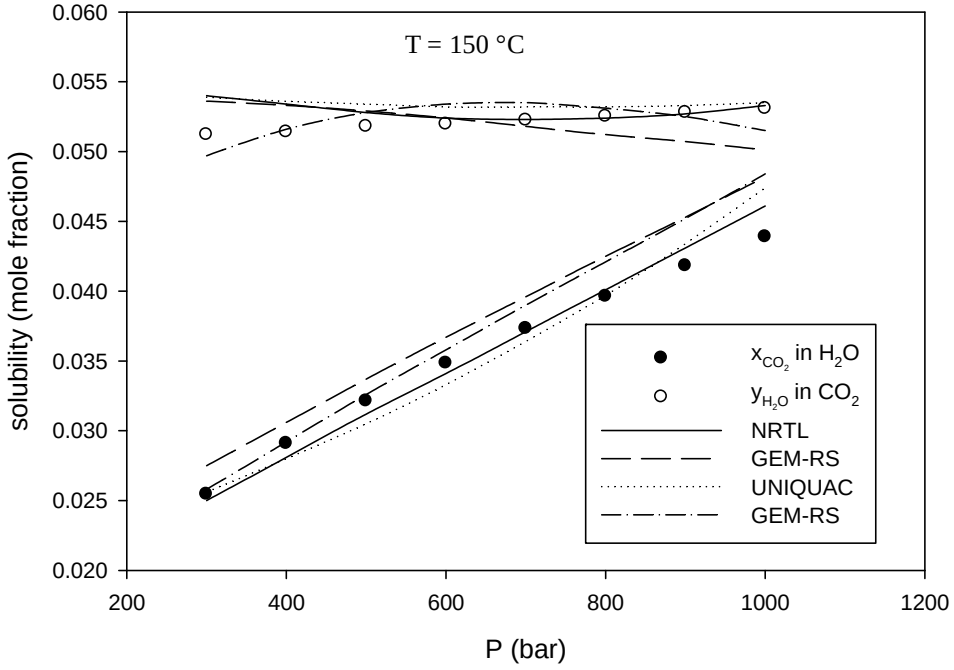
T = 150 °C
solubility (mole fraction)
P (bar)
0.060
0.055
0.050
0.045
0.040
0.035
0.030
0.025
0.020
200
400
600
800
1000
1200
x_{CO_2} in H_2O
y_{H_2O} in CO_2
NRTL
GEM-RS
UNIQUAC
GEM-RS

(c)

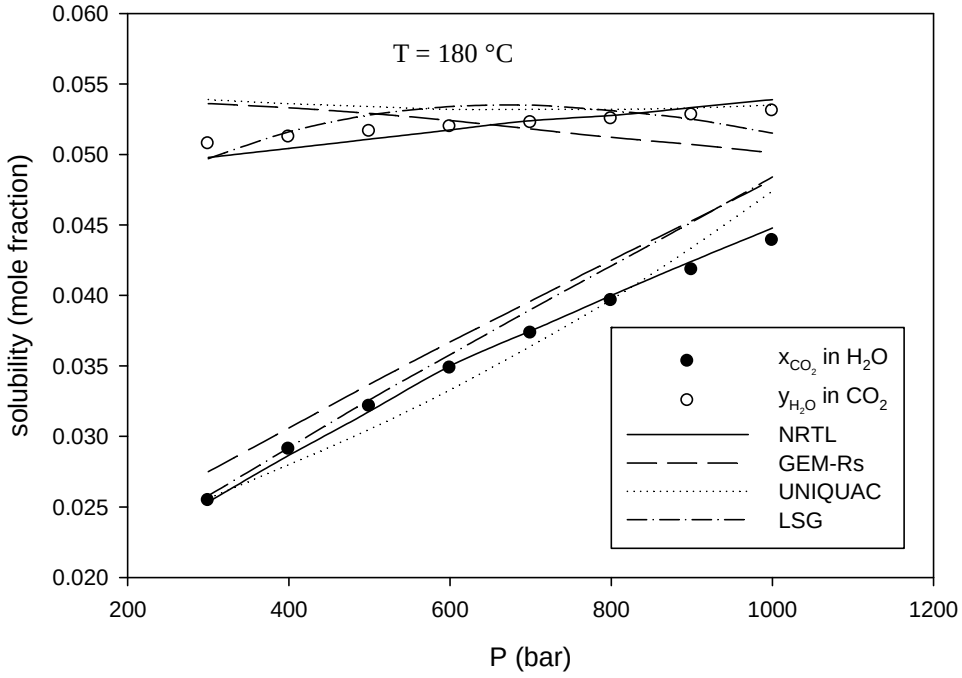
T = 180 °C
solubility (mole fraction)
P (bar)
0.060
0.055
0.050
0.045
0.040
0.035
0.030
0.025
0.020
200
400
600
800
1000
1200
x_{CO_2} in H_2O
y_{H_2O} in CO_2
NRTL
GEM-Rs
UNIQUAC
LSG

(d)

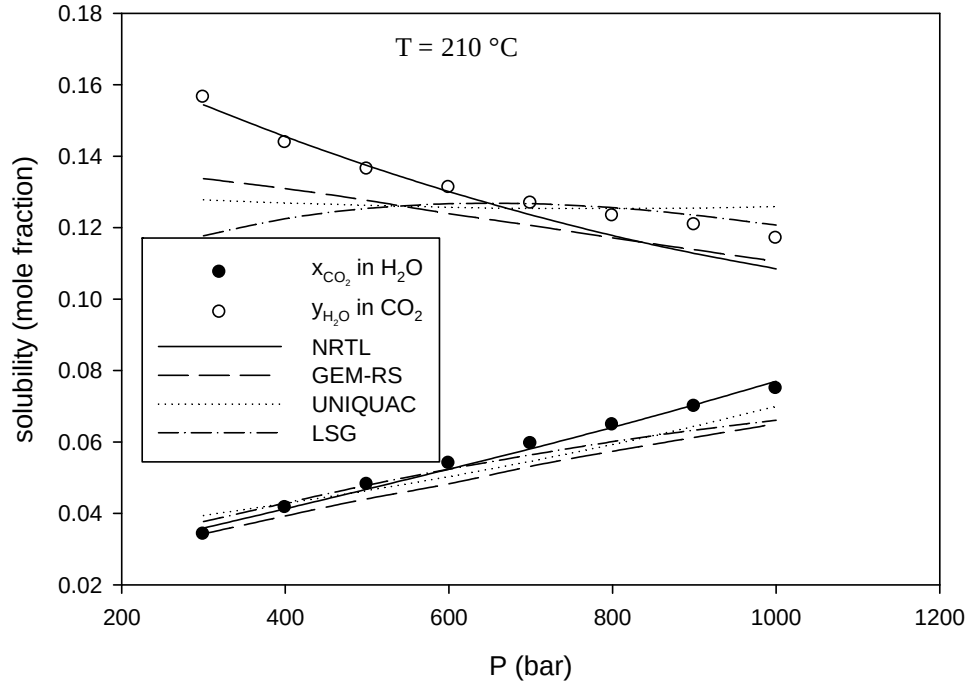
T = 210 °C
solubility (mole fraction)
P (bar)
0.18
0.16
0.14
0.12
0.10
0.08
0.06
0.04
0.02
200
400
600
800
1000
1200
x_{CO_2} in H_2O
y_{H_2O} in CO_2
NRTL
GEM-RS
UNIQUAC
LSG

(e)

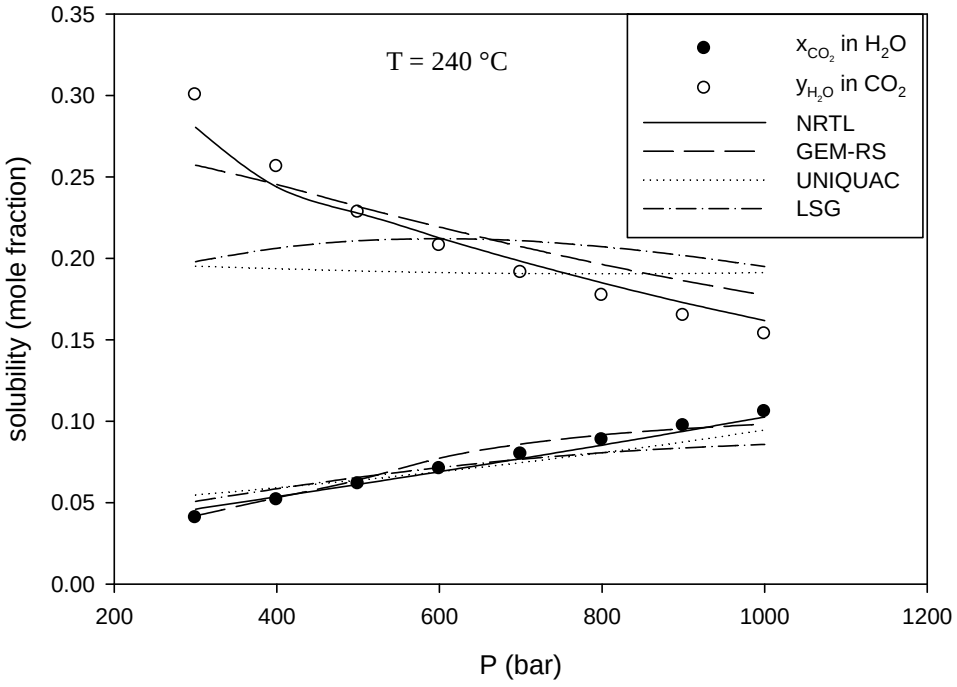

(f)

Figure 3.2: Comparisons of solubilities calculated by different models

Table 3.3: Comparisons of computation time

computation time (CPU time in s)							
Notebook				Lab workstation			
LSM	S-W	D et al.	R-K	LSM	S-W	D et al.	R-K
0.004	0.059	0.047	0.031	0.0029	0.034	0.012	0.011

3.6 Concluding Remarks: Liquid state models can be applied to phase equilibrium calculations of supercritical CO_2 and H_2O upon simple modifications. Introducing temperature and pressure related terms in these models will give stability to predict the solubility data carrying only LLE flash calculations over the large pressure and temperature ranges. On one hand, advantages of this tool is: we do not have to be concerned with selecting an EoS for CO_2, and H_2O; do not need mixing rules; do not require suitable expression for fugacity computations and other matters relating to VLE calculations. This calculation will be performed faster than that of VLE and will save huge computational expenses. On the other hand, the limitation of this scheme is that it is applicable only at high temperatures and pressures.

3.7 References:

[1] Climate Change 1995: The Science of Climate Change, Summary for Policymakers and Technical Summary of the Working Group I report., Intergovernmental Panel on Climate Change. Cambridge, UK, 1996.

[2] Climate Change 2001: The Scientific Basis, Summary for Policymakers and Technical Summary of the Working Group I Report., Intergovernmental Panel on Climate Change. Cambridge, UK, 2001.

[3] Climate change 2007: Mitigation. Contribution of Working group III to the Fourth Assessment Report of the Intergovernmental Panel on Climate Change., (eds. B. Metz, O.R.D., P. R. Bosch, R. Dave, and L. A. Meyer), Intergovernmental Panel on Climate Change. Cambridge, United Kingdom and New York, NY, USA, 2007.

[4] Gilfillan, S.M.V., Ballentine, C.J., Holland, G., Blagburn, D., Lollar, B.S., Stevens, S., Schoell, M., Cassidy, M., *Geochimica et Cosmochimica Acta, 72,* 1174-1198, 2008.

[5] Kaszuba, J.P., Janecky, D.R., Snow, M.G., *Appl Geochem., 18,* 1065-1080 (2003).

[6] Pruess, K., Muller, N., *Water Resources Research, 45,* W03402, 2009.

[7] Dubessy, J., Buschaert, S., Lamb, W., Pironon, J., Thiery, R., *Chem Geology, 173,* 193-205, 2001.

[8] Roedder, E., *Reviews in Minerology, 12,* 1984.

[9] Butcher, S.S., Charlson, R.J., Orians, G.H., Wolfe, G.V., Global Biogeochemical Cycles. Academic Press, London, 1992.

[10] Millero, F.J., Thermodynamics of the carbon dioxide system in the oceans. *Geochim et Cosmochim Acta,* 59, 661– 677, 1995.

[11] Allen, A.J., Green Chemistry: Dense Carbon dioxide and Water as Environmentally Benin Reaction Media. Massacusetts Institute of Technology, 2004.

[12] Fukushima, Y., *R&D Review of Toyota CRDL., 35,* 1-9, 2000.

[13] Kemmere, M., Supercritical Carbon Dioxide for Sustainable Polymer Processes, Weinheim, 2005.

[14] Ota, M., Abe, Y., Watanabe, M., Smith, R.L.J., Inomata, H., *Fluid Phase Equilib., 228-229,* 553-559, 2005.

[15] Pruess, K., Enhanced Geothermal Systems (EGS): Comparing Water and CO_2 as Heat Transmission Fluids. New Zealand Geothermal Workshop, New Zealand, 2007.

[16] White, C.M., Smith, D.H., Jones, K.L., Goodman, A.L., Jikich, S.A., LaCount, R.B., DuBose, S.B., Ozdemir, E., Morsi, B.I., Schroeder, K.T., *Energy Fuels, 19*, 659-724, 2005.

[17] Daridon, J.L., Lagourette, B., Saint-Guirons, H., Xans, P., *Fluid Phase Equilib., 91,* 31-54, 1993.

[18] Diamond, L.W., Akinfiev, N.N., *Fluid Phase Equilib., 28, 265-290,* 2003.

[19] Duan, Z., Moller, N., Weare, J.H., *Geochim et Cosmochim Acta, 59, 2869-2882,* 1995.

[20] Duan, Z., Sun, R., *Chem. Geology, 193,* 257-271, 2003.

[21] Ferry, J.M., Baumgartner, L., *Rev Miner Geochem., 17,* 323-365, 1987.

[22] Holloway, J.R., Fugacity and activity of molecular species in supercritical fluids. Fraser, D.G. (Ed.), Thermodynamics in Geology. D Reidel Publishing Co., Holland, Dordrecht, 1977.

[23] Hu, J., Duan, Z., Zhu, C., Chou, I.-M., *Chem Geology., 238,* 249-267, 2007.

[24] Kerrick, D.M., Jacobs, G.K., *Am J Sci., 281,* 735-767, 1981.

[25] Mader, U.K., *Can Miner., 29,* 767-790, 1991.

[26] Span, R., Wagner, W., *J Phys Chem Ref Data, 25,* 1509-1596, 1994.

[27] Spycher, N., Pruess, K., *Geochim et Cosmochim Acta, 67,* 3015-3031, 2003.

[28] Spycher, N., Pruess, K., *Geochim et Cosmochim Acta, 69,* 3309-3320, 2005.

[29] Tödheide, K., *Ber. Bunsenges Phys Chem Geology, 86,* 1005–1016, 1982.

[30] Abrams, D.S., Prausnitz, J.M., *AIChE J., 21,* 116-128, 1975.

[31] Renon, H., Prausnitz, J.M., *AIChE J., 14,* 135-144, 1968.

[32] Vera, J.H., Sayegh, S.G., Ratcliff, G.A., *Fluid Phase Equilib., 1,* 113-135, 1977.

[33] Keshtkar, A., Jalali, F., Moshfeghian, M., *Fluid Phase Equilib., 140,* 107-128, 1997.

[34] Kristensen, J.N., Christensen, P.L., *Fluid Phase Equilib., 82,* 199-206, 1993.

[35] Kwak, C., Sandler, S.I., Byun, H.-S., *Korean J Chem Eng., 23,* 1016-1022, 2006.

[36] Lindeloff, N., Michelsen, M., *SPE J.*, 298-303, 2003.

[37] Pahlevanzadeh, H., Mohseni-Ahooei, A., *Iran J Chem Chem Eng., 24,* 21-26, 2005.

[38] Sørensen, H., Pedersen, K.S., Christensen, P.L., *Organic Geochem., 33,* 635-642, 2002.

[39] Thomsen, K., Rasmussen, P., *Chem Eng Sci., 54,* 1787-1802, 1999.

[40] Huron, M.-J., Vidal, J., *Fluid Phase Equilib., 3,* 255-271, 1979.

[41] Wang, L.-S., Lang, Z.-X., Guo, T.-M., *Fluid Phase Equilib., 117,* 364-372, 1996.

[42] Demirel, Y., Gecegormez, H., *Can J Chem Eng., 67,* 455-461, 1989.

[43] Demirel, Y., Paksoy, H.O., Gecegormez, H., *Thermochim Acta, 194,* 343-359 (1992).

[44] Nagata, I., Meyer, T., Gmehling, J., *Fluid Phase Equilib., 65,* 19-39, 1991.

[45] Skjold-Jorgensen, S., Rasmussen, P., Fredenslund, A.A., *Chem Eng Sci., 35,* 2389-2403, 1980.

[46] Islam, A.W., Kabadi, V.N., *Chem Process Eng., 32,* 101-115, 2011.

[47] Prausnitz, J.M., Litchtenthaler, R.N., de Azevedo, E.G., Molecular Thermodynamics of Fluid Phase Equilibria, Third ed., New Jersy, 1999.

[48] Islam, A.W., Javvadi, A., Kabadi, V.N., *Ind Eng Chem Res., 50,* 1034-1045, 2011.

[49] Islam, A.W., Kabadi, V.N., Analysis of Partition Coefficients and Ternary Liquid-Liquid Equilibrium Data for Highly Non-Ideal Systems., 3rd National Conference of Environmental Science and Technology, Greensboro, NC 2007, pp. 311-317. SpringerLink., 2009.

[50] Duan, Z., Moller, N., Weare, J.H., *Geochim et Cosmochim Acta, 56,* 2605-2617, 1992.

[51] Islam, A.W., Carlson, E.S., A Fully Non-iterative Technique for Phase Equilibrium and Density Calculations of CO2+Brine System and an Equation of State for CO_2. 37th Stanford Geothermal Workshop, Stanford University, 2012.

CHAPTER FOUR

†Application of SAFT equation for CO_2+H_2O phase equilibrium calculations over a wide temperature and pressure range

Akand W. Islam, Eric S. Carlson
Department of Chemical & Biological Engineering, The University of Alabama, AL-35487, USA

Abstract: The statistical associating fluid theory (SAFT) equation of state is employed for the correlation and prediction of vapor – liquid equilibrium of CO_2+H_2O binary system for a wide temperature (10 – 300 °C) and pressure (1 – 600 bar) range. To make the equation applicable for these temperature and pressure ranges effective number of segments and energy parameter have been co-related with reduced temperature and pressure. Simple mixing rules have been applied to obtain binary interaction parameter. The results were found to be in satisfactory agreement with the literature data except in fully miscible regions.

Keywords: SAFT, CO_2, H_2O, phase equilibrium, solubility, wide temperature and pressure

†*Fluid Phase Equilib., 321, 17-24, 2012.*

4.1 Introduction: Increasing global interest in the geologic sequestration of CO_2 has raised important questions about its long term fate. For long term carbon sequestration the phase equilibrium of CO_2 in H_2O has clear inference [1-3]. The solubility of H_2O into CO_2 is also of importance because it affects the reactivity of CO_2 with surrounding rocks [4, 5]. This also determines the capacity of injected CO_2 to dry the rock formations adjacent to injection wells [6, 7]. The partitioning of H_2O into CO_2 determines the time required for the removal of H_2O from the enhanced geothermal systems, and the type of chemical interactions that may take place between the CO2 plume, reservoir rocks, and engineering systems [8]. Therefore CO_2+H_2O phase equilibrium calculations is an important aspect for the study of CO_2 geologic storage.

Equation of state (EOS) [9, 10] differs in their accuracy in modeling systems due to their mathematical complexity. Several EOS's have been proposed to calculate phase equilibrium between CO_2 and H_2O for a wide temperature and pressure range [8, 11-23]. Basically all of these models are the modifications of either Van der Waals type EOS, like, Redlich – Kwong [24], Peng-Robinson [25], Patel – Teja [26] and so on, or, the modifications of Virial type EOS, like, Bendict et al., [27] Starling – Han [28] and so on. A nice review on EOS's of CO_2 and H_2O phase equilibrium computations has been carried out by Sun and Dubessy [29]. SAFT is a molecular based EOS, is very suitable for modeling water-bearing fluids because hydrozen bonding force between water molecules is taken into account. This can work well over a wide range of temperatures from subcritical region to supercritical region. More so, only few parameters (pure compound and mixture) are needed which can have a theoretical significance and facilitates their estimation. There are some investigations [30-39] where CO_2+H_2O phase equilibrium calculations were shown using SAFT equation.

Due to the statistical mechanics basis, SAFT holds great promise as a predictive model in general. This is capable of modeling various sized molecules with sites that can associate with other sites. This takes into account the possible chain-like shape and size differences in the fluid molecules, and the effects of any association between molecules such as hydrogen bonding. It also poses statistical fluid theory, with the hard sphere and dispersion terms analogous to the van der Waals molecular co-volume and attraction terms, and the chain formation and association terms based on Wertheim' theory [40-44]. In this study we will show usability of SAFT equation

for the range of temperature 10-300 °C and that of pressure up to 600 bar using only a single set of parameters.

We have considered carbon dioxide as homonuclear chainlike molecules. This is an approximation because the actual molecules are heteronuclear. Therefore, a molecule of the polar fluid is mentioned to be composed of *m* hard-spherical segments of diameter σ tangentially bonded together to form chains. The equation of state is written in terms of the Helmholtz free energy for binary mixture of associating chain molecules can be expressed as the sum of hard-sphere repulsion, hard-chain formation, dispersion, and association terms. Mathematically,

$$A^{res} = A^{hs} + A^{chain} + A^{disp} + A^{assoc} \tag{1}$$

Where A^{hs} is the free energy of hard-sphere fluid; A^{chain} is the free energy associated with the formation of chains from hard spheres; A^{disp} and A^{assoc} are the contributions to the free energy of dispersion and association interactions, respectively.

4.2 Equation of State: Based upon Eq. 1 detailed description of the equations which were involved in computation process is elaborated in subsequent subsections.

4.2.1 Hard-Sphere repulsion term

Following Boublik-Mansoori-Carnahan-Starling-Leland [45, 46] equation the hard sphere term A^{hs} is expressed as

$$\frac{A^{hs}}{RT} = \frac{\sum_{i=1}^{N} x_i m_i}{\pi \rho_s}\left[\frac{3\zeta_1\zeta_2 - \zeta_2^3/\zeta_3^2}{1-\zeta_3} + \frac{\zeta_2^3/\zeta_3^2}{(1-\zeta_3)^2} + \frac{\zeta_2^3}{\zeta_3^2}\ln(1-\zeta_3)\right] - \sum_{i=1}^{N} x_i m_i \ln(1-\zeta_3) \tag{2}$$

where

$$\zeta_j = \frac{\pi}{6}\rho_n \sum_{i=1}^{N} x_i m_i d_i^j \qquad (j = 0, 1, 2, 3) \tag{3}$$

and

$$\rho_s = \rho_n \sum_{i=1}^{N} x_i m_i \tag{4}$$

To make Eq. (2) more applicable for wide temperature and pressure range, the effective number of segments, m_i has been correlated with reduced temperature, T_r (T/T_c), and reduced pressure, P_r (P/P_c) following way

$$m_i = A_i + B_i P_r + C_i T_r \tag{5}$$

d_i is the hard sphere diameter of segment *i*. It relates with the soft-sphere diameter, σ_i based on Barker-Henderson perturbation theory and is expressed as [47]

$$\frac{d_i}{\sigma_i} = \frac{1 + 0.2977kT/\varepsilon_i}{1 + 0.33163kT/\varepsilon_i + 0.001047(kT/\varepsilon_i)^2} \tag{6}$$

where ε_i is the energy parameter of the L-J (Lennard-Jones) potential. Like Eq. (5) this has also been expressed as follows

$$\varepsilon_i / k = D_i + E_i P_r + F_i T_r \tag{7}$$

4.2.2 Hard-Chain formation term

A^{chain} is presented as [48]

$$\frac{A^{chain}}{RT} = \sum_{i=1}^{N} x_i (1 - m_i) \ln[g_i^{hs}(d_i)] \tag{8}$$

where

$$g_i^{hs}(d_i) = \frac{1}{1-\zeta_3} + \frac{3d_i\zeta_2}{2(1-\zeta)^2} + \frac{d_i^2}{2(1-\zeta_3)^3} \tag{9}$$

and for binary mixture

$$g_{ij}^{seg}(d_{ij}) = g_{ij}^{hs}(d_{ij}) = \frac{1}{1-\zeta_3} + \frac{3d_i d_j}{d_i + d_j}\frac{\zeta_2}{(1-\zeta_3)^2} + 2\left(\frac{d_i d_j}{d_i + d_j}\right)^2 \frac{\zeta_2^2}{(1-\zeta_3)^3} \tag{10}$$

4.2.3 Dispersion term

A^{disp} is computed using the expression by Cotterman et al., [47] based on the L-J potential.

$$\frac{A_{disp}}{RT} = \sum_{i=1}^{N} x_i m_i \frac{1}{T_R}(A_1^{disp} + A_2^{disp}/T_R) \tag{11}$$

where

$$A_1^{disp} = \rho_R(-8.5959 - 4.5424\rho_R - 2.1268\rho_R^2 + 10.285\rho_R^3) \tag{12}$$

$$A_2^{disp} = \rho_R(-1.9075 + 9.9724\rho_R - 22.216\rho_R^2 + 15.904\rho_R^3) \tag{13}$$

$$T_R = kT / \varepsilon_x \tag{14}$$

$$\rho_R = \frac{6}{\sqrt{2\pi}}\zeta_3 \tag{15}$$

$$\varepsilon_x\sigma_x^3 = \sum_{i=1}^{N}\sum_{j=1}^{N} y_i y_j \varepsilon_{ij}\sigma_{ij}^3 \tag{16}$$

$$y_i = \frac{x_i m_i}{\sum_{j=1}^{N} x_j m_j} \tag{17}$$

The cross parameters between segments, ε_{ij} and σ_{ij} are calculated from following combining rules

$$\sigma_{ij} = (\sigma_i + \sigma_j)/2 \tag{18}$$

$$\varepsilon_{ij} = (1-k_{ij})\sqrt{\varepsilon_i\varepsilon_j} \tag{19}$$

k_{ij} is the binary interaction parameter.

4.2.4 Association term

The Helmholtz energy due to association is calculated using following expression [49]

$$\frac{A^{assoc}}{RT} = \sum_i x_i \left[\sum_{A_i} (\ln X^{A_i} - X^{A_i}/2) + .5M_i \right] \tag{20}$$

Here m_i is the number of associating sites on molecule *i*. X^{A_i} is the mole fraction of molecules *i*, in mixtures with other components, not bonded at site *A* and is given by

$$\Delta^{A_iB_j} = d_{ij}^3 g_{ij}(d_{ij})^{seg} \kappa^{A_iB_j} [\exp(\varepsilon^{A_iB_j}/kT) - 1] \tag{21}$$

κ^{AB} is the bonding volume, and ε^{AB}/k is the associating energy. For mixture, following combining rules have been applied

$$\kappa^{A_iB_j} = \kappa^{A_jB_i} = (\kappa^{A_iB_i} + \kappa^{A_jB_j})/2 \tag{22}$$

$$\varepsilon^{A_iB_j} = \varepsilon^{A_jB_i} = (1-k_{ij}^{AB})\sqrt{\varepsilon^{A_iB_i}\varepsilon^{A_jB_j}} \tag{23}$$

where k_{ij}^{AB} is the binary associating interaction parameter. Calculations of chemical potentials, compressibility factor, and other properties of the components are shown in Appendix.

4.3 Parameter Estimation: Three pure component parameters for non-associating fluid CO_2 and five parameters for associating fluid H_2O have to be estimated. These are L-J potential well depth (ε / k), the soft-sphere diameter of the segments (σ), the number of the segments in the molecule (m), the bonding volume (κ^{AB}), and the associating energy between sites A and B (ε^{AB}). These are predicted from regressing density [50, 51] and CO_2+H_2O phase equilibrium data [52-75] simultaneously. Van der Waals one fluid mixing rules with the binary interaction parameter k_{ij} for the dispersion interactions and the parameter k_{ij}^{AB} for the associating interactions have been applied. k_{ij} is estimated to be 0.98. Since CO_2 is non-associating fluid, k_{ij}^{AB} is set to zero. Four-site model [76, 77] is used for the water molecule. The regressed segment parameters are shown in **Table 4.1**.

Table 3.1 Segment parameters of pure fluids

	CO_2	H_2O
P (bar)	10 - 600	10 - 600
T (K)	283.15 - 573.15	283.15 - 573.15
m [Eq. 5]		
A	14.2510376	0.182045774
B	0.0579913896	-.0299311078
C	-3.18338604	-0.0672066604
σ (10^{-10} m)	1.35479513	8.07923743
ε / k (k) [Eq. 7]		
D	5.82994041	5.22073609
E	0.360613659	-1404.66374
F	18.3594617	-3.33815292
ε^{AB} / k (K)		1195.20
κ		0.038

To keep numeric values of m and ε / k positive, absolute values are used during regression process. In all cases the objective function is set as

$$F_i(obj) = \sum_{k}^{N_k} \sum_{i}^{N_i} \frac{1}{N} \frac{F_{i,k}(lit) - F_{i,k}(cal)}{F_{i,k}(lit)} \tag{24}$$

where,

$N=N_k \times N_i$

Ni=number of data points

N_k=total number of property (like k=1 (density), k=2 (phase equilibrium))

4.4 Results and discussions: Using the mixing rules of Eqs. 16 – 19 and the required parameters reported in previous section comparisons between literature and calculated phase equilibrium data (solubility of CO_2 in H_2O and that of H_2O in CO_2) are shown in **Fig 4.1 (a - z)**. Isotherm results are shown at the temperatures 10, 20, 30, 40, 50, 60, 80, 100, 150, 200, 250, 275, and 300 °C. For cases where data was not obtained at exact temperatures (like, 10, 30, and 150 °C),

comparisons are shown with available data at the nearest temperatures. As seen in these figures, the calculations are in good agreement with experimental data typically within the range of uncertainty. The calculated results tend to follow any of the trends established by cases where experimental data differ significantly among the references especially at higher temperatures (T > 150 °C) and pressures (P > 500 bar). This is because each data source has its own share of assumptions and potential problems. At 300 °C the dew point data of Blencoe et al., [71] are well reproduced up to pressures 500 bar, above which our calculations seem to be misleading because full miscibility is approached. According to Blencoe et al., [71] the critical line at 300 °C occurs at about 567 bar. Above this condition, the CO_2 solubilities reported by them differ noticeably from the measurements by Todheide and Frank [67], and Takenouchi and Kennedy [65].

There is a noticeable divergence between the gas phase data reported by Takenouchi and Kennedy [65] and Todheide and Frank [67]. The latter are not reproduced well, and the model appears in much better agreement with the water solubilities determined by Takenouchi and Kennedy [65]. Again at 300 °C, the model appears to somewhat underestimate the amount of H_2O in CO_2, with results still follow a good trend up to 500 bar. Above that the model completely deviates from the measured data as fully miscible behavior is approached.

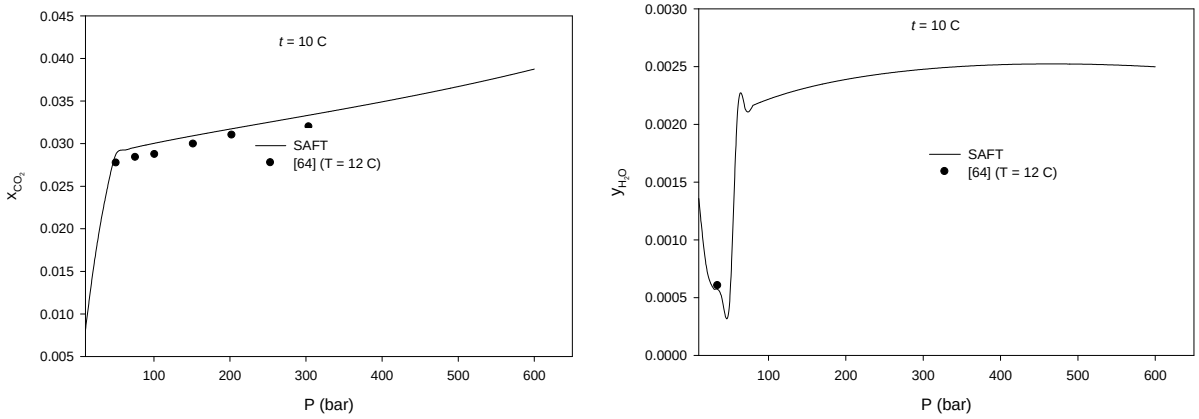

a b

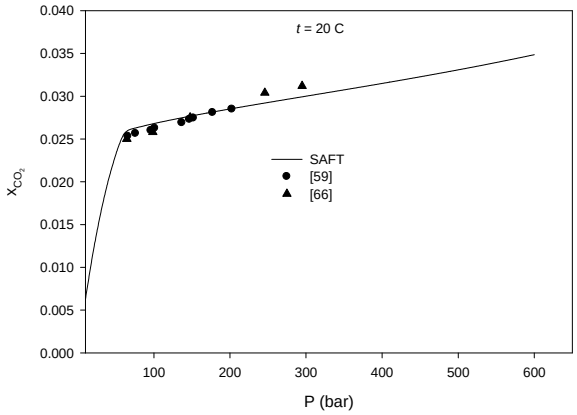
t = 20 C
SAFT
[59]
[66]
x_{CO_2}
P (bar)

c

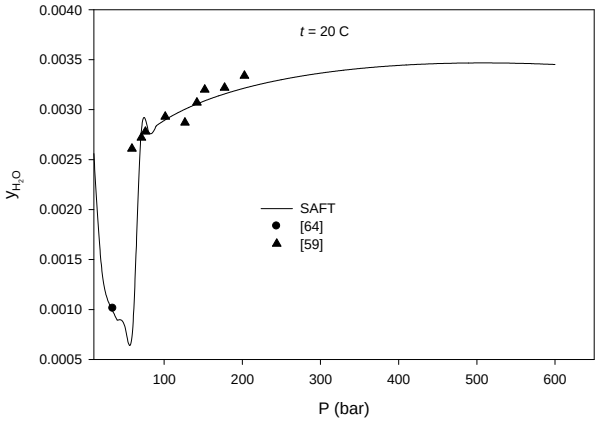
t = 20 C
SAFT
[64]
[59]
y_{H_2O}
P (bar)

d

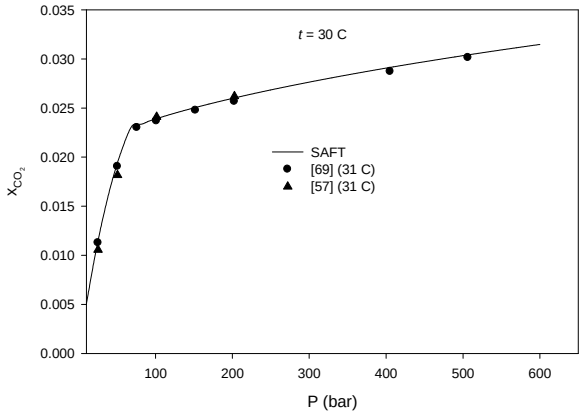
t = 30 C
SAFT
[69] (31 C)
[57] (31 C)
x_{CO_2}
P (bar)

e

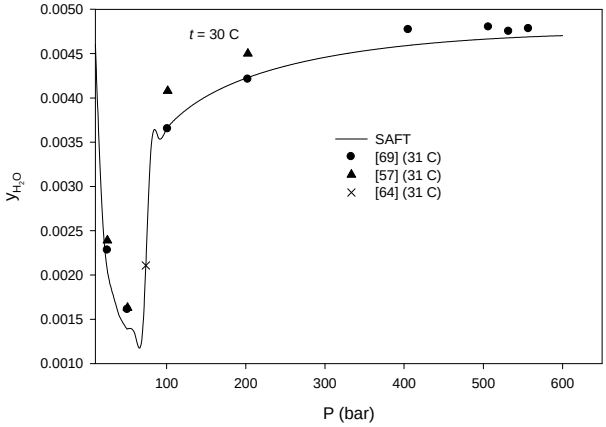
t = 30 C
SAFT
[69] (31 C)
[57] (31 C)
[64] (31 C)
y_{H_2O}
P (bar)

f

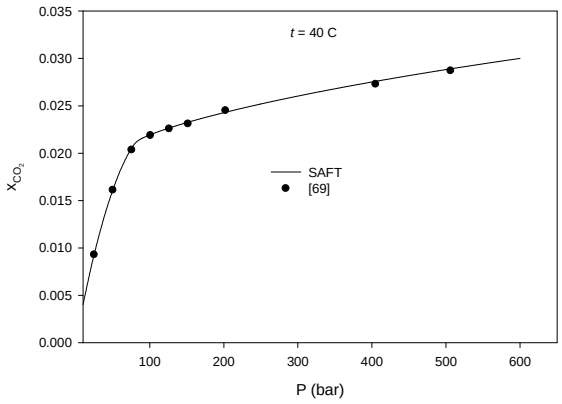
t = 40 C
SAFT
[69]
x_{CO_2}
P (bar)

g

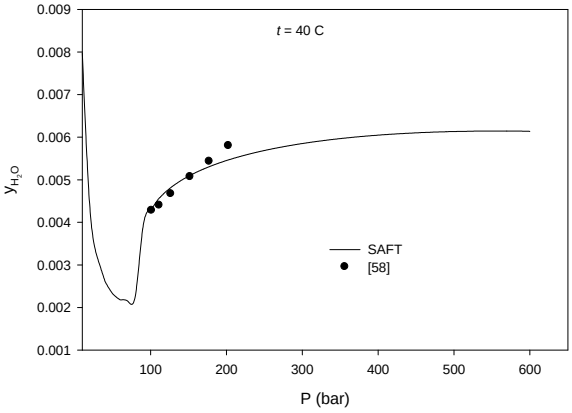
t = 40 C
SAFT
[58]
y_{H_2O}
P (bar)

h

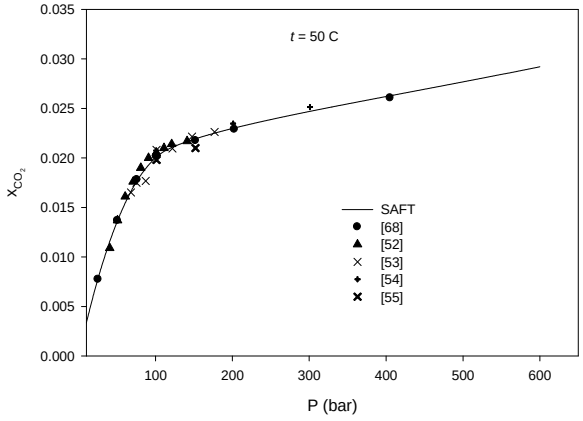
t = 50 C
SAFT
[68]
[52]
[53]
[54]
[55]
x_{CO_2}
P (bar)

i

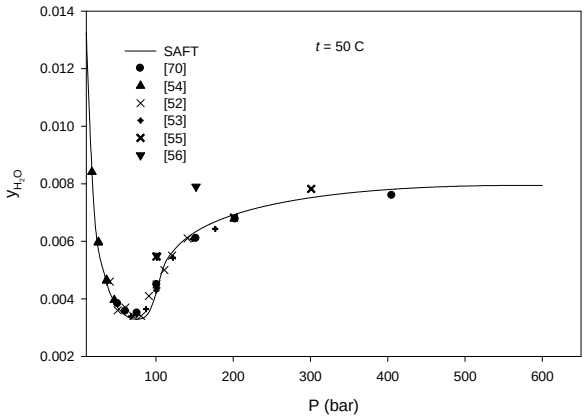
t = 50 C
SAFT
[70]
[54]
[52]
[53]
[55]
[56]
y_{H_2O}
P (bar)

j

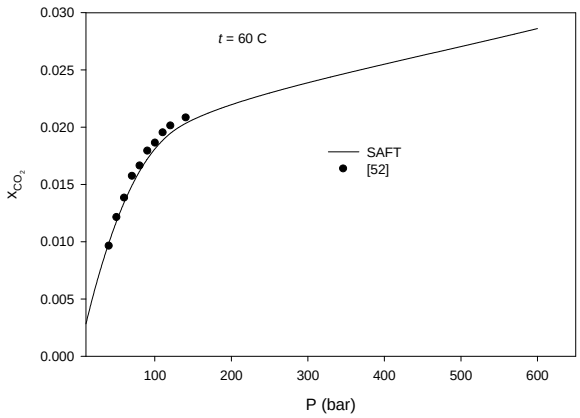
t = 60 C
SAFT
[52]
x_{CO_2}
P (bar)

k

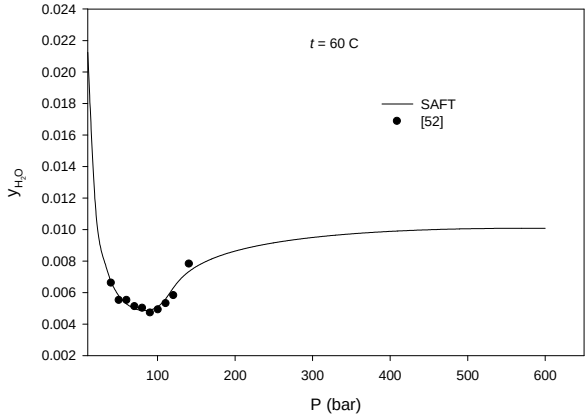
t = 60 C
SAFT
[52]
y_{H_2O}
P (bar)

l

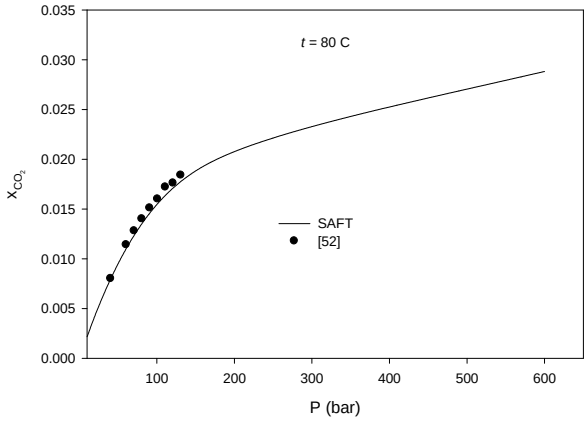
t = 80 C
SAFT
[52]
x_{CO_2}
P (bar)

m

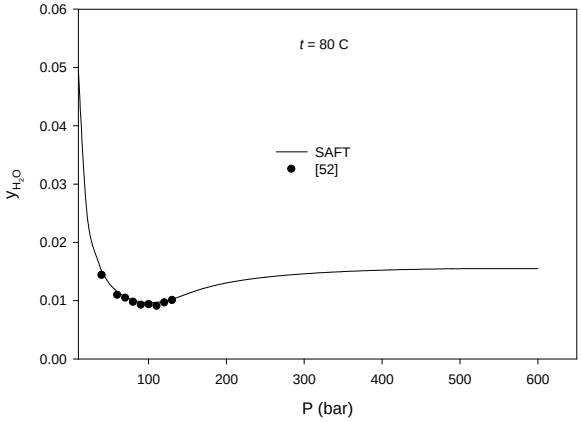
t = 80 C
SAFT
[52]
y_{H_2O}
P (bar)

n

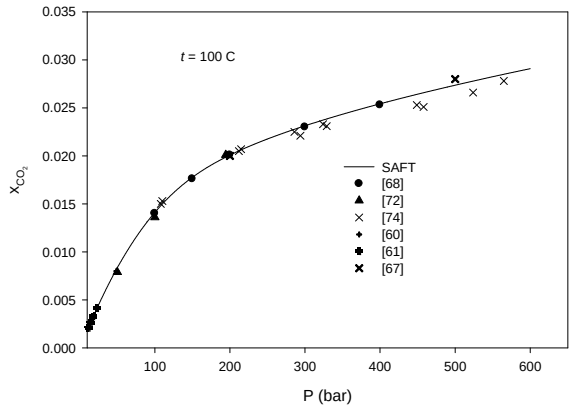
t = 100 C
SAFT
[68]
[72]
[74]
[60]
[61]
[67]
x_{CO_2}
P (bar)

o

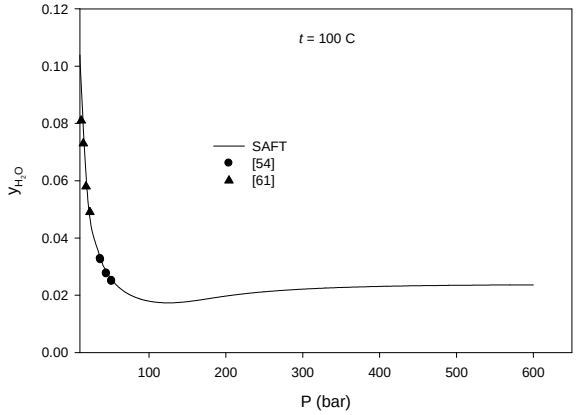
t = 100 C
SAFT
[54]
[61]
y_{H_2O}
P (bar)

p

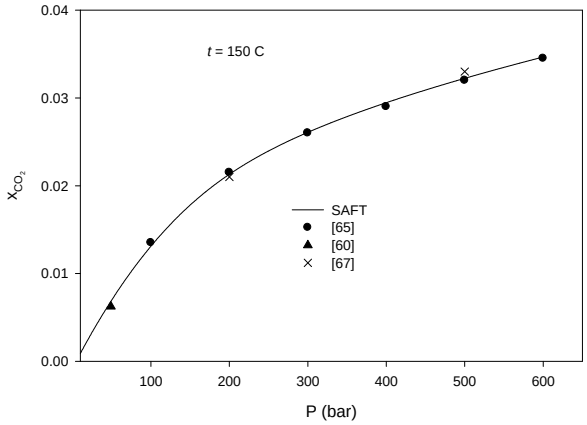
t = 150 C
SAFT
[65]
[60]
[67]
x_{CO_2}
P (bar)

q

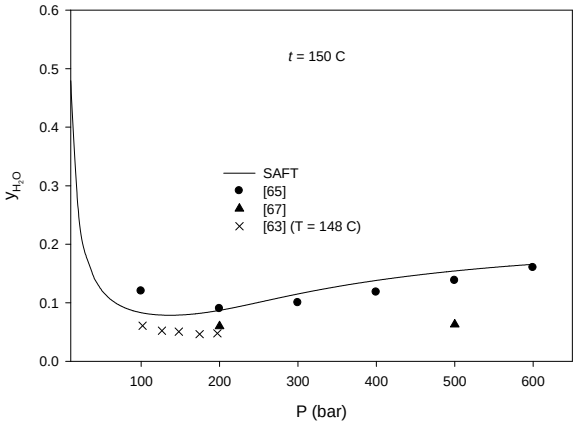
t = 150 C
SAFT
[65]
[67]
[63] (T = 148 C)
y_{H_2O}
P (bar)

r

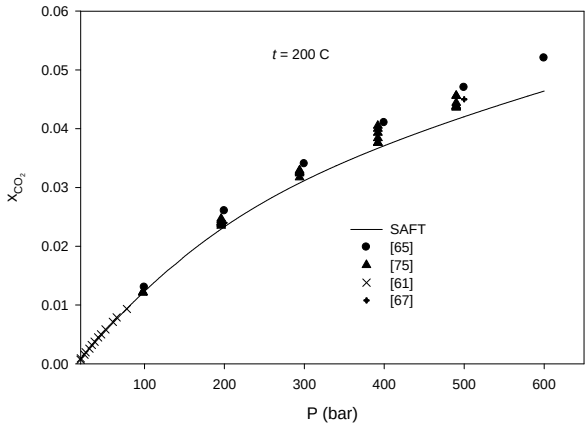
t = 200 C
SAFT
[65]
[75]
[61]
[67]
x_{CO_2}
P (bar)

s

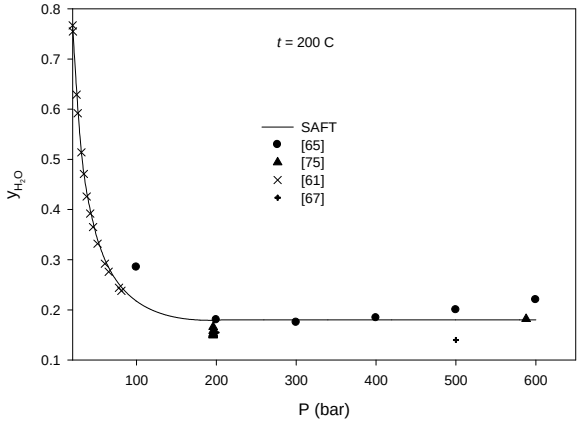
t = 200 C
SAFT
[65]
[75]
[61]
[67]
y_{H_2O}
P (bar)

t

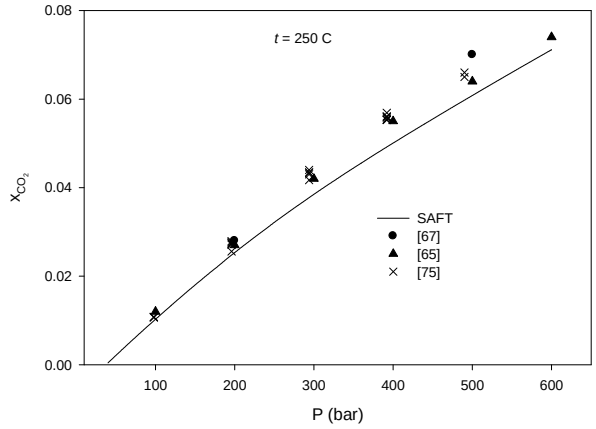

u

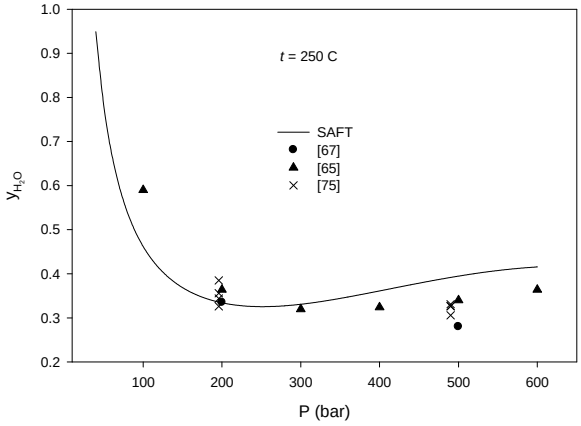

v

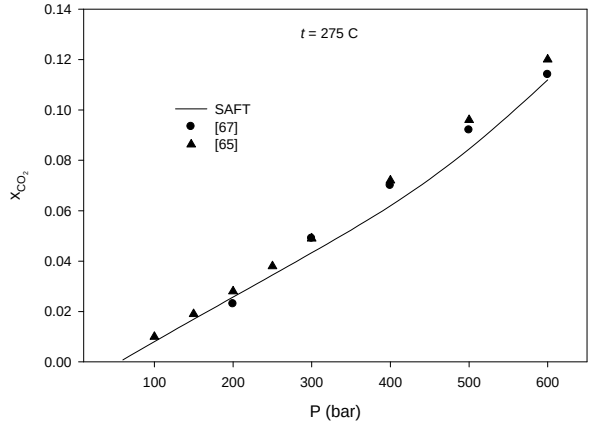

w

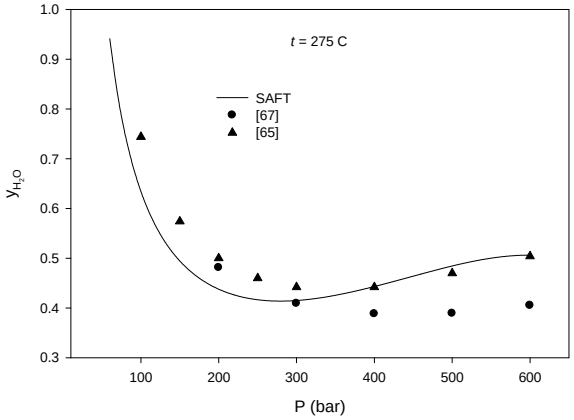

x

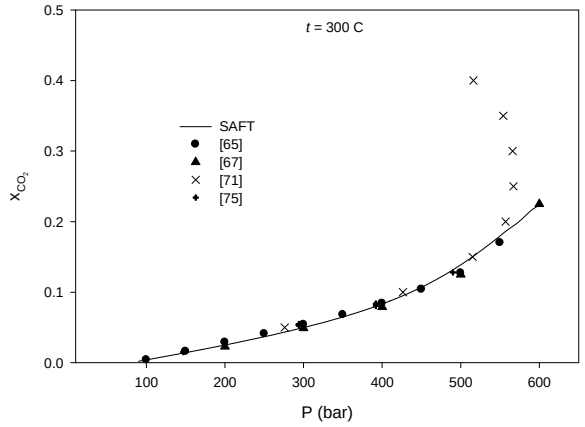

y

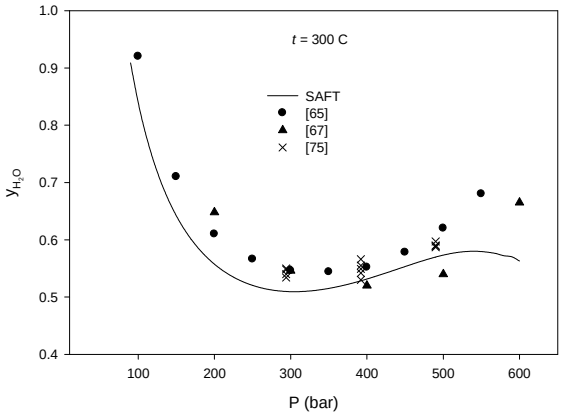

z

Figure 4.1: Comparisons between calculated and literature mutual solubilities of CO_2 and H_2O.

4.5 Conclusions: The SAFT equation of state is employed to compute the phase equilibria for CO_2 + H_2O binary system over the temperature range 10 – 300 °C and the pressure up to 600 bar. Pure component and binary interaction parameters estimated from the density and vapor-liquid equilibrium data of the constituent binary system is implemented. Except in fully miscible region (t = 300 °C, P > 560 bar), a satisfactory agreement between predicted values and experimental data is found.

4.6 Notations:

A	Helmholtz free energy, J
d	Hard – sphere diameter, 10^{-10} m
g	radius distribution function
k	Boltzman constant, JK^{-1}
M	number of associated sites
N	number of molecules
N_{AV}	Avogadro's number, 6.02217×10^{23} mol^{-1}
P	pressure, bar
P_c	critical pressure (for CO_2 73.83 bar, for H_2O 220.55 bar)
T_c	critical temperature (for CO_2 304.2 °K, for H_2O 647.1 °K)
T	absolute temperature, °K
t	absolute temperature, °C
R	gas constant, $JK^{-1}mol^{-1}$
x	mole fraction in liquid phase
X_i^A	mole fraction of molecule i not bonded at site A
y	mole fraction in vapor phase
Z	compressibility factor
$\beta = 1/kT$	
$\frac{\varepsilon}{k}$	energy parameter of dispersion, K
$\frac{\varepsilon^{AB}}{k}$	energy parameter of association between sites A and B
κ^{AB}	bonding volume

Δ^{AB}	association strength between sites *A* and *B*
μ	chemical potential
ρ	molar density, $molm^{-3}$
ρ_n	number density, m^{-3}
A, *B*, *C*	
D, E, F	constants
assoc	association interaction
chain	hard – sphere chain
disp	dispersion interaction
hs	hard sphere
obj	objective function
lit	literature value
cal	calculated value

4.7 References:

[1] Gilfillan, S.M.V., Ballentine, C.J., Holland, G., Blagburn, D., Lollar, B.S., Stevens, S., Schoell, M., Cassidy, M., *Geochim et Cosmochim Acta., 72,* 1174-1198, 2008.

[2] Kaszuba, J.P., Janecky, D.R., Snow, M.G., *Appl Geochem., 18,* 1065-1080, 2003.

[3] Moore, J., Adams, M., Allis, R., Lutz, S., Rauzi, S., *Chem Geology.,* 217*,* 365-385, 2005.

[4] Lin, H., Fujii, T., Takisawa, R., Takahashi, T., Hashida, T., *J Mater Sci., 43,* 2307-2315, 2008.

[5] Suto, Y., Liu, L., Yamasaki, N., Hashida, T., *Appl Geochem., 22,* 202-218, 2007.

[6] Pruess, K., Muller, N., *Water Resources Research., 45,* w03402, 2009.

[7] Giorgis, T., Carpita, M., Battistelli, A., *Energy Convers Mgmt., 48,* 1816-1826, 2007.

[8] Spycher, N., Pruess, K., *Transp Porous Media, 82,* 173-196, 2009.

[9] Wei, Y.S., Sadus, R. J., *AIChE J., 46,* 169-196, 2000.

[10] Kontogeorgis, G.M., Economou, I.G., *J Supercrit Fluids, 55,* 421-437, 2010.

[11] Daridon, J.L., Lagourette, B., Saint-Guirons, H., Xans, P., *Fluid Phase Equilib., 91,* 31-54, 1993.

[12] Diamond, L.W., Akinfiev, N.N., *Fluid Phase Equilib., 28,* 265-290, 2003.

[13] Duan, Z., Moller, N., Weare, J.H., *Geochim et Cosmochim Acta, 59,* 2869-2882, 1995.

[14] Duan, Z., Sun, R., *Chem Geology., 193,* 257-271, 2003.

[15] Ferry, J.M., Baumgartner, L., *Rev Miner Geochem, 17,* 323-365, 1987.

[16] Holloway, J.R., Fugacity and activity of molecular species in supercritical fluids. Fraser, D.G. (Ed.), Thermodynamics in Geology. 1977, Holland, Dordrecht: D Reidel Publishing Co.

[17] J. Hu, J., Duan, Z., Zhu, C., Chou, I.-M., *Chem Geology., 238,* 249-267, 2007.

[18] Kerrick, D.M., Jacobs, G.K., *Am J Sci., 281,* 735-767, 1981.

[19] Mader, U.K., *Can Miner., 29,* 767-790, 1991.

[20] Span, R., Wagner, W., *J Phys Chem Ref Data, 25,* 1509-1596, 1994.

[21] Spycher, N., Pruess, K., *Geochim et Cosmochim Acta, 69,* 2005, 3309-3320.

[22] Tödheide, K., *Ber Bunsenges, 86,* 1005-1016, 1982.

[23] Spycher, N., Pruess, K., *Geochim et Cosmochim Acta, 67,* 3015-3031, 2003.

[24] Redlich, O., Kwong, J.N.S., *Chem Rev., 44,* 233-244, 1949.

[25] Peng, D.Y., Robinson, D.B., *Ind Eng Chem Fundam., 15,* 59-64, 1976.

[26] Patel, N.C., Teja, A.S., *Chem Eng Sci., 37,* 463-473, 1982.

[27] Bendict, M., Webb, G.B., Rubin, L.C., *J Chem Phys., 8,* 334-345, 1940.

[28] Starling, K.E., Han, M.S., *Hydrocarbon Process, 51,* (1972) 129-132, 1972.

[29] Sun, R., Dubessy, J., *Geochim Cosmochim Acta, 74,* 1982-1998, 2010.

[30] Li, X., P. Englezos, P., *Ind Eng Chem Res., 42,* 4953-4961, 2003.

[31] X. Li, Englezos, P., *Fluid Phase Equilib., 224,* 111-118, 2004.

[32] Huang, S.H., Radosz, M., *Ind Eng Chem Res., 29,* 2284-2294, 1990.

[33] Perakis, C., Voutsas, E., Magoulas, K., Tassios, D., *Fluid Phase Equilib., 243,* 142-150, 2006.

[34] Kontogeorgis, G.M., Tsivintzelis, I., Michelsen, M.L., Stenby, E.H., *Fluid Phase Equilib., 301,* 244-256, 2011.

[35] Tsivintzelis, I., Kontogeorgis, G.M., Michelsen, M., Stenby, E.H., *Fluid Phase Equilib., 306,* 38-56, 2011.

[36] Kislev, S.B., Ely, J.F., *Ind Eng Chem Res., 45,* 3981-3990, 2006.

[37] Hu, Z.-Q., Yang, J.-C., Li, Y.-G., *Fluid Phase Equilib., 205,* 25-36, 2003.

[38] dos-Ramos, M.C., Blas, F.J., Galindos, A., *J Phys Chem. C, 111,* 15924-15934, 2007.

[39] Valtz, A., Chapoy, A., Coquelet, C., Patrice, P., Richon, D., *Fluid Phase Equilib., 226,* 333-344, 2004.

[40] Wertheim, M.S., *J Stat Phys., 35,* 19-34, 1984.

[41] Wertheim, M.S., *J Stat Phys., 35,* 35-47, 1984.

[42] Wertheim, M.S., *J Stat Phys., 42,* 459-476, 1986.

[43] Wertheim, M.S., *J Stat Phys., 42,* 477-492, 1986.

[44] Octavio, L.M., Numerical aspects of the SAFT Equation of State, University of Rhode Island, 2006.

[45] Boublik, T., *J Chem Phys., 53,* 471-472, 1970.

[46] Mansoori, G.A., Carnahan, N.F., Starling, K.E., Leland, T.W., *J Chem Phys., 54,* 1523-1525, 1971.

[47] Cotterman, R.L., Schwarz, B.J., J.M. Prausnitz, J.M., *AIChE J., 32,* 1986, 1787-1798.

[48] Chapman, W.G., Gubbins, K.E., Jackson, G., Radosz, M., *Fluid Phase Equilib., 52,* 31-38, 1989.

[49] Chapman, W.G., Gubbins, K.E., G. Jackson, M. Radosz, New Reference Equation of State for Associating Liquids. *Ind Eng Chem Res., 29,* 1709-1721, 1990.

[50] ASME Steam Table, 1993.

[51] http://sequestration.mit.edu/tools/index.html.

[52] Bamberger, A., Sieder, G., Maurer, G., *J Supercrit Fluids, 17,* 97-100, 2000.

[53] Briones, J.A., Mullins, J.C., Thies, M.C., *Fluid Phase Equilib., 36,* 235-246, 1987.

[54] Coan, C.R., King, A.D.J., *J Am Chem Soc., 93,* 1971, 1857-1862.

[55] Dohrn, R., Bunz, A.P., *Fluid Phase Equilib., 83,* 149-158, 1993.

[56] D'Souza, R., Patrick, J.R., Teja, A.S., *Can J Chem Eng., 66,* 319-323, 1988.

[57] Gillepsie, P.C., Wilson, G.M., Vapor-Liquid and Liquid-Liquid equilibria: Water-Methane, Water-Carbon dioxide, Water-Hydrogen Sulfide, Water-n Pentane, in Research report PR-48, Gas processors association: Tulsa. 1982.

[58] Jackson, K., Bowman, L.E., Fulton, J.L., *Anal Chem., 67,* 2368-2372, 1995.

[59] King, M.B., Mubarak, A., Kim, J.D., Bott, T.R., *J Supercrit Fluids., 5,* 296-302, 1992.

[60] Malinin, S.D., Kurovskaya, N.A., *Geokhimiya, 4,* 547-551, 1975.

[61] Muller, G., Bender, E., Maurer, G., *Berichte der Bunsen-Gesellshaft fur Physikalische Chemie, 92,* 148-160, 1988.

[62] Rosenbauer, R.J., Bischoff, J.L., Kokasalan, T., *Trans Am Geophys Union,* 2001.

[63] Sako, T., Sugeta, T., Nakazawa, N., Obuko, T., Sato, M., Taguchi, T., Hiaki, T., *J Chem Eng Jpn., 24,* 449-454, 1991.

[64] Song, K.Y., Kobayashi, R., *SPE Form. Eval, 2,* 500-508, 1987.

[65] Takenouchi, S., Kennedy, G.C., *Am J Sci., 262,* 1055-1075, 1964,

[66] Teng, H., Yamasaki, N., Chun, M.-K., *J Chem Thermodyn., 29,* 1301-1310, 1997.

[67] Todhiede, K., Franck, E.U., *Zeitschrift für Physikalische, 37,* 387-401, 1963.

[68] Wiebe, R., Gaddy, V.L., *J Am Chem. Soc, 61,* 315-318, 1939.

[69] Wiebe, R., Gaddy, V.L., *J Am Chem. Soc, 62,* 815-817, 1940.

[70] Wiebe, R., Gaddy, V.L., *J Am Chem. Soc., 63,* 475-477, 1941.

[71] Blencoe, J.G., Naney, M.T., Anovitz, L., *Am Mineral., 86,* 1100-1111, 2001.

[72] Koschel, D., Coxam, J.-Y., Rodier, L., V. Majer, V., *Fluid Phase Equilib., 247,* 107-120, 2006.

[73] Roedder, E., *Reviews in Minerology, 12,* 1984.

[74] Prutton, C.F., Savage, R.L., *J Am Chem Soc., 67,* 1550-1554, 1945.

[75] Malinin, S.D., *Geokhimiya, 3,* 235-245, 1959.

[76] Economou, I.G., Tsonopoulos, C., *Chem Eng Sci., 52,* 511-525, 1997.

[77] Yakoumis, I.V., Kontogeorgis, G.M., Voutsas, E.C., Hendriks, E.M., Tassios, D.P., I*nd Eng Chem Res., 37*, 4175-4182, 1998.

4.8 Appendix: SAFT model is presented in terms of molar residual Helmohltz energy (A^{res}) in Section 2. This section will provide other properties and functions needed to calculate phase equilibria, for instance, chemical potential (μ_i), compressibility factor (*Z*), and fugacity coefficient (φ_i). However, we will start with the μ_i, which is a derivative of A^{res} with respect to the mole number of component *i* at constant *T*, volume (V), and non-*i* components.

A. Expression for chemical potential: We discuss μ_i in the order used to present the corresponding Helmohltz energy terms, i.e., hard-sphere, chain, dispersion, and association terms. The expression is as follows

$$\mu_i^{res} = \mu_i^{hs} + \mu_i^{chain} + \mu_i^{disp} + \mu_i^{assoc} \qquad \text{(A1)}$$

The hard-sphere contribution to the chemical potential, μ_i^{hs}, can be expressed as

$$\frac{\mu_i^{hs}}{RT} = \frac{m_i d_i^3 \zeta_0 + 3m_i d_i^2 \zeta_1 + 3m_i d_i \zeta_2 - 3m_i d_i^2 \zeta_2^2 / \zeta_3^2 + 2m_i d_i^3 \zeta_2^3 / \zeta_3^3 - m_i d_i^3 \zeta_2^3 / \zeta_3^2}{1-\zeta_3}$$
$$+ \frac{3m_i d_i^3 \zeta_1 \zeta_2 + 3m_i d_i^2 \zeta_2^2 / \zeta_3^2 - m_i d_i^3 \zeta_2^3 / \zeta_3^2 - 2m_i d_i^3 \zeta_2^3 / \zeta_3^3}{(1-\zeta)^2} + \frac{2m_i d_i^3 \zeta_2^3 / \zeta_3^2}{(1-\zeta_3)^3} \quad \text{(A2)}$$
$$+ \frac{(3m_i d_i^2 \zeta_2^2 \zeta_3 - 2m_i d_i^3 \zeta_2^3)\ln(1-\zeta_3)}{\zeta_3^3} - m_i \ln(1-\zeta_3)$$

μ_i^{chain} , the chain contribution to the chemical potential is expressed as

$$\frac{\mu_i^{chain}}{RT} = (1-m_i)\ln[g_i^{hs}(d_i)] + \rho \sum_{i=1}^{N} \frac{x_i(1-m_i)}{g_i^{hs}(d_i)} \left[\frac{\partial g_i^{hs}}{\partial \rho_i} \right]_{T,V,\rho_{j\neq i}} \quad \text{(A3)}$$

where

$$\left[\frac{\partial g_i^{hs}(d_i)}{\partial \rho_i} \right]_{T,V,\rho_{j\neq i}} = \frac{\pi}{6} m_i d_i^2 \left[\frac{d_i}{(1-\zeta_3)^2} + \frac{3d_i(1-\zeta_3+2d_i\zeta_2)}{2(1-\zeta)^3} + \frac{d_i^2(2\zeta_2 - 2\zeta_2\zeta_3 + 3d_i\zeta_2^2)}{2(1-\zeta_3)^4} \right] \quad \text{(A4)}$$

The dispersion contribution to the chemical potential, μ_i^{disp} is expressed as

$$\frac{\mu_i^{disp}}{RT} = \frac{m_i A_1^{disp}}{T_R} + \frac{m_i A_2^{disp}}{T_R^2} + \frac{\rho_s}{T_R} \left[\frac{\partial A_1^{disp}}{\partial \rho_i} \right]_{T,V,\rho_{j\neq i}} - \left(\frac{\rho_s A_1^{disp}}{T_R^2} + 2\frac{\rho_s A_2^{disp}}{T_R^3} \right) \left[\frac{\partial T_R}{\partial \rho_i} \right]_{T,V,\rho_{j\neq i}} \quad \text{(A5)}$$

where

$$\left[\frac{\partial A_1^{disp}}{\partial \rho_i} \right]_{T,V,\rho_{j\neq i}} = \frac{m_i d^3}{\sqrt{2}} (-8.5959 - 9.0848\rho_R - 6.3807\rho_R^2 + 41.141\rho_R^3) \quad \text{(A6)}$$

$$\left[\frac{\partial A_2^{disp}}{\partial \rho_i} \right]_{T,V,\rho_{j\neq i}} = \frac{m_i d_i^3}{\sqrt{2}} \left(-1.9075 + 19.9449\rho_R - 66.648\rho_R^2 + 63.616\rho_R^3 \right) \quad \text{(A7)}$$

$$\left[\frac{\partial T_R}{\partial \rho_i} \right]_{T,V,\rho_{j\neq i}} = \frac{2m_i \rho \left(\varepsilon_x \sum_{l=1}^{N} x_l m_l \rho_{il}^3 - \sum_{l=1}^{N} x_l m_l \rho_{il}^3 \varepsilon_{il} \right)}{\beta \varepsilon_x^2 \sigma_x^3 \rho_s^2} \quad \text{(A8)}$$

μ_i^{assoc} , the association contribution to the chemical potential can be expressed as

$$\frac{\mu_i^{assoc}}{RT} = \left\{ \sum_{A_i} \left(\ln X^{A_i} - .5X^{A_i} \right) + .5M_i + \sum_j x_j \rho \sum_{A_j} \left[\left(\frac{\partial X^{A_j}}{\partial \rho_i} \right)_{T,\rho_{j\neq i}} \left(\frac{1}{X^{A_j}} - .5 \right) \right] \right\} \quad \text{(A9)}$$

where

$$\left(\frac{\partial X^{A_j}}{\partial \rho_j}\right)_{T,\rho_{j\neq i}} = -\left(X^{A_j}\right)^2 N_{AV}\left\{\sum_{B_i} X^{B_i}\Delta^{A_jB_i} + \rho\sum_k\sum_{B_k} X_k\left[\Delta^{A_jB_{kl}}\left(\frac{\partial X^{B_k}}{\partial \rho_i}\right)_{T,\rho_{l\neq i}} + X^{B_k}\left(\frac{\partial \Delta^{A_jB_k}}{\partial \rho_i}\right)_{T,\rho_{l\neq i}}\right]\right\} \tag{A10}$$

$$\left(\frac{\partial X^{B_j}}{\partial \rho_i}\right)_{T,\rho_{k\neq i}} = -\left(X^{B_j}\right)^2\left\{N_{AV}\sum_{C_i} X^{C_i}\Delta^{B_iC_i} + \sum_k\sum_{C_k} N_{AV}\rho_k\left[\Delta^{B_jC_k}\left(\frac{\partial X^{C_k}}{\partial \rho_i}\right)_{T,\rho_{l\neq i}} + X^{C_k}\left(\frac{\partial \Delta^{B_jC_k}}{\partial \rho_i}\right)_{T,\rho_{l\neq i}}\right]\right\} \tag{A11}$$

$\left(\frac{\partial X^{C_k}}{\partial \rho_i}\right)_{T,\rho_{l\neq i}}$ or so forth can be found similarly following Eq. (A11). Now the expression for $\left(\frac{\partial \Delta^{A_jB_k}}{\partial \rho_i}\right)_{T,\rho_{l\neq i}}$ is given by

$$\left(\frac{\partial \Delta^{A_jB_k}}{\partial \rho_i}\right)_{T,\rho_{l\neq i}} = d_{jk}^3\left[\frac{\partial g_{jk}(d_{jk})^{hs}}{\partial \rho_i}\right]_{T,\rho_{l\neq i}}\left[\exp\left(\varepsilon^{A_jB_k}/kT\right)-1\right]\kappa^{A_jB_k} \tag{A12}$$

where

$$\left[\frac{\partial g_{jk}(d_{jk})^{hs}}{\partial \rho_i}\right]_{T,\rho_{l\neq i}} = \frac{\pi N_{AV}}{6} m_i\left\{\frac{d_i^3}{(1-\zeta_3)^2} + 3\frac{d_jd_k}{d_j+d_k}\left[\frac{d_i^2}{(1-\zeta_3)^2} + \frac{2d_i^3\zeta_2}{(1-\zeta_3)^3}\right] + 2\left(\frac{d_jd_k}{d_j+d_k}\right)^2\left[\frac{2d_i^2\zeta_2}{(1-\zeta_3)^3} + \frac{3d_i^3\zeta_2^2}{(1-\zeta_3)^4}\right]\right\} \tag{A13}$$

B. Expression for compressibility factor: *Z*, the compressibility factor is calculated from the Helmholtz free energy, *A*, through

$$Z = \rho\left[\frac{\partial(A/RT)}{\partial \rho}\right]_{T,N} = 1 + Z^{hs} + Z^{disp} + Z^{chain} + Z^{assoc} \tag{B1}$$

where

$$Z^{hs} = \frac{\sum_{i=1}^{N} x_i m_i}{\zeta_0}\left[\frac{6\zeta_1\zeta_2 - \zeta_2^3/\zeta_3^3 - \zeta_2^3/\zeta_3 + \zeta_0\zeta_3}{1-\zeta_3} + \frac{6\zeta_1\zeta_2\zeta_3 - 3\zeta_1\zeta_2 - 2\zeta_2^3/\zeta_3 + 2\zeta_2^3/\zeta_3^2}{(1-\zeta_3)^2} + \frac{3\zeta_2^3/\zeta_3 - \zeta_2^3/\zeta_3^2}{(1-\zeta_3)^3}\right] \tag{B2}$$

$$Z^{disp} = \sum_{i=1}^{N} x_i m_i \left(Z_1^{disp}/T_R + Z_2^{disp}/T_R^2\right) \tag{B3}$$

and

$$Z_1^{disp} = \rho_R(-8.5959 - 9.0848\rho_R - 6.3807\rho_R^2 + 41.1416\rho_R^3) \tag{B4}$$

$$Z_2^{disp} = \rho_R(-1.9075 + 19.9449\rho_R - 66.648\rho_R^2 + 63.616\rho_R^3) \tag{B5}$$

$$Z^{chain} = \sum_{i=1}^{N} \frac{x_i(1-m_i)}{g_i^{hs}(d_i)}\left[\frac{\zeta_3 + 1.5d_i\zeta_2}{(1-\zeta_3)^2} + \frac{3d_i\zeta_2\zeta_3 + d_i^2\zeta_2^2}{(1-\zeta_3)^3} + \frac{1.5d_i^2\zeta_2^2\zeta_3}{(1-\zeta_3)^4}\right] \tag{B6}$$

$$Z^{assoc} = \frac{1}{RT}\left[\sum_i x_i \mu_i^{assoc} - A^{assoc}\right] \tag{B7}$$

Here μ_i^{assoc} and A^{assoc} are presented by Eqs. (A9) and (20), respectively.

C. Expression for fugacity coefficient: The relation between φ_i (fugacity coefficient) and the residual chemical potential of component *i* is as follows

$$\ln\varphi_i = \frac{\mu_i^{res}}{RT} - \ln Z \tag{C1}$$

μ_i^{res} and Z can be obtained from Eqs (A1) and (B1), respectively.

CHAPTER FIVE

†Viscosity Models and Effects of Dissolved CO_2

Akand W. Islam, Eric S. Carlson
Department of Chemical and Biological Engineering
The University of Alabama, Tuscaloosa, AL-35487, USA.

Abstract: A comprehensive study is carried out on the viscosity modeling for the geologic sequestration of CO_2 in the pressure (*P*) and temperature (*T*) range 1-600 bar, 20-105 °C, respectively. For the liquid phase we have subsequently presented viscosity models for pure water (H_2O), brine water (H_2O+NaCl), H_2O+CO_2, H_2O+NaCl+CO_2, and saline water of having typical sea water composition. In each case we attempted to develop very accurate formulations but having less number of parameters than existing ones in order for efficient computations. Effects of dissolved CO_2 are studied very extensively. We have found that deviations can be 2-8% in liquid phase viscosity calculations due to neglecting CO_2 dissolution. In addition, model for vapor phase is also suggested.

†*Energy & Fuels, 26, 5330-5360, 2012*.

5.1 Introduction: Increasing atmospheric concentrations of greenhouse gases are suspected of causing a gradual warming of the Earth's surface and potentially disastrous changes to global climate. Because CO_2 is a major greenhouse gas, storing in subsurface formations is being explored as a viable option to limit the accumulation of greenhouse gases in the atmosphere. Carbon sequestration, sometimes broadly referred as carbon management, is a way to reduce greenhouse gas emissions while still enjoying the benefits of fossil fuel use. This is a complementary approach to the current CO_2 mitigation efforts of improved energy efficiency and increased use of non-carbon energy sources. These days much attention is given in the carbon management option because it is very compatible with the large energy production and delivery infrastructure now in place and because non-fossil energy sources face large barriers, renewables are very expensive and nuclear has public acceptance problems. Sequestration covers technologies that capture carbon at its source (e.g., power plants, industrial processes) and directs it to non-atmospheric sinks (e.g., depleted oil and gas reservoirs, deep saline formations, coal seams, hard rock caverns, deep ocean), as well as processes that increase the removal of carbon from the atmosphere by natural processes (e.g., forestation [1]). Due to the great potential of storage while being wide spread available and having lack of effective uses, the most promising places for sequestration are aquifers [2,3] Accurate evaluation of the capacity of a saline aquifer for CO_2 sequestration and the fate of the injected fluids in sedimentary basins require analysis of thermo-physical properties of CO_2 and brine. The thermo-physical properties include thermodynamic properties, e.g., PVT (pressure-volume-temperature) behaviors; transport properties, e.g., viscosities, thermal conductivities, and diffusion coefficients. Our previous studies [4-6] contain comprehensive investigations on PVT behaviors. This study focuses on one of primary transport properties: viscosity, and presents some simpler and efficient tools to compute the viscosity of aqueous and gaseous phases in CO_2 sequestration.

For any multiphase flow system viscosity play an important role. Viscosity characterizes the fluids' resistance with respect to deformation under shear stress [7]. The lower a fluid's viscosity, the lower is its resistance to flow and the displacement of one fluid by another. If the viscosity of the injected CO_2 is higher than the viscosity of the CO_2 and brine that is in the aquifer, the displacement front is stable. On the other hand if the viscosity of the injected CO_2 is lower, the displacement front can become unstable. Therefore accurate prediction of viscosity is

extremely important. Though not exactly on simulation of CO_2 sequestration, the authors [8,9] have studied extensively on sensitivity of reservoir simulations to uncertainties in viscosity of both liquid and vapor phases.

In general viscosity change of brine with CO_2 saturation is neglected in the simulators developed so far [10-14]. This is because there is no model available in the literature for the effect of dissolved CO_2 on water/brine viscosity. However, in reality viscosity is directly related to the density and dissolution of CO_2 may cause density variations by 2-3% [4, 15]. When injecting CO_2, the plume has the tendency to flow upward. However, a small amount of CO_2 will dissolve into the water; under the influence of the small density difference, that water has the tendency to flow downward Ref [16, 17] showed viscosity of water varies from 1.0 to 1.3 centipoise for 4% (weight) dissolved CO_2. Tumasjan et al. [18] showed that the viscosity of water varies from 1.0 to 1.3 centipoise for 4% (by weight) dissolved CO_2. Thus it is important that CO_2 dissolution be considered while modeling viscosity. In this paper, we will present some simple empirical formulations for computing the viscosity of pure water, brine (H_2O+NaCl and H_2O+NaCl+CO_2), and typical seawater (having 3.5% salinity) for the pressure and temperature range of a saline aquifer at 1-600 bar, and 20°-105° C, respectively [19]. We will also analyze how viscosity varies quantitatively for CO_2 dissolution in the aqueous phase.

5.2 Viscosity of pure Water: Very well established formulations for the viscosity of H_2O are available for wide pressure and temperature ranges [20-26]. The most recent one is IAPWS Formulation 2009 [27] which covers temperature and pressure ranges up to 900 °C, and 10000 bar, respectively. Here more simple correlation with less number of parameters for the viscosity calculations applicable for the interested *P-T* range is proposed. The correlation is given by function of *P* and *T*,

$$\mu_{H_2O} = a_0 + \sum_{i=1}^{3} b_i \exp(-c_i T) + P\sum_{i=0}^{3} d_i (T - 293.15)^i \qquad (1)$$

Parameters of Eq. 1 are estimated by regressing generated data from IAPWS Formulation 2009 (IAPWS09). The coefficients of *a*, *b*, *c*, and *d* are reported in **Table 5.1**. In this equation *P* is in

MPa (Mega Pascal). Viscosity data of pure water can be regenerated by Eq. 1 with maximum 0.05% deviation as compared to IAPWS09. Here deviation means, Deviation = $\frac{lit - cal}{lit} \times 100$.

Figure 5.1 show comparisons of data at different isotherms (20, 50, 80, and 100 °C). From this figure this is clearly seen that maximum divergence (~0.05%) occurs at 100 °C at low pressure (<5 bar). Otherwise divergences lie within 0.04%.

Table 5.1: Coefficients of Eq. 1.

i	*a*	*b*	*c*	*d*
0	9.03591045e+01			-1.22757462e-01
1		3.40285740e+04	1.40090092e-02	2.15995021e-02
2		8.23556123e+08	4.86126399e-02	-3.65253919e-04
3		-9.28022905e+08	5.26696663e-02	1.97270835e-06

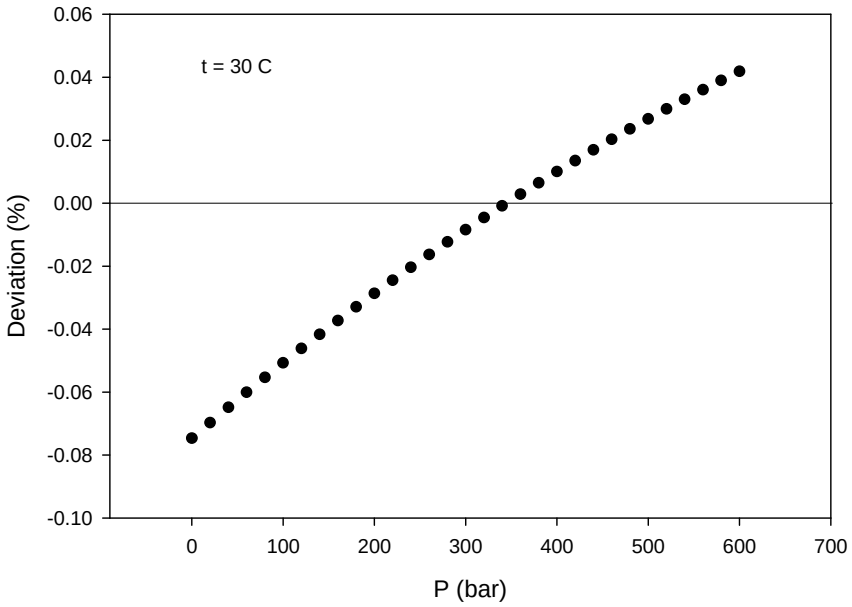

(a)

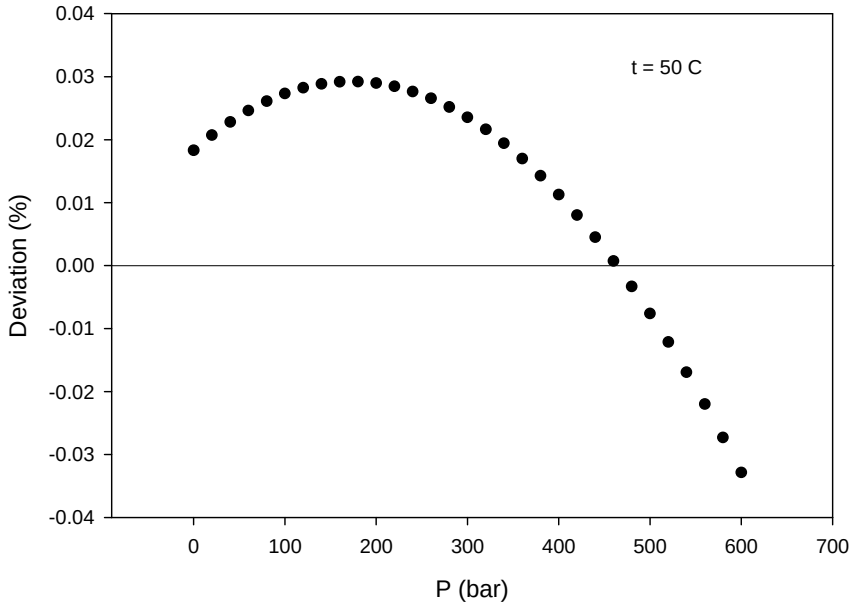
t = 50 C
Deviation (%)
P (bar)
0.04
0.03
0.02
0.01
0.00
-0.01
-0.02
-0.03
-0.04
0
100
200
300
400
500
600
700

(b)

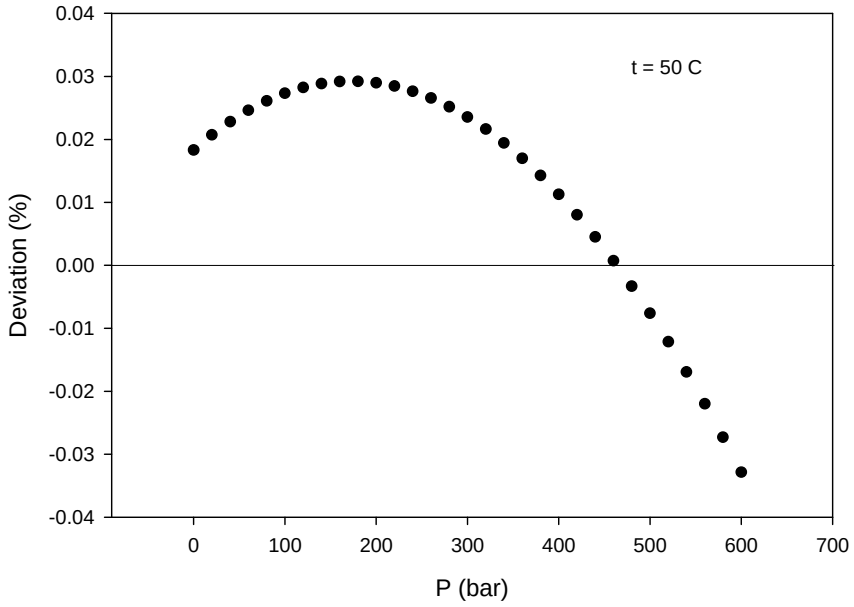
t = 50 C
Deviation (%)
P (bar)
0.04
0.03
0.02
0.01
0.00
-0.01
-0.02
-0.03
-0.04
0
100
200
300
400
500
600
700

(c)

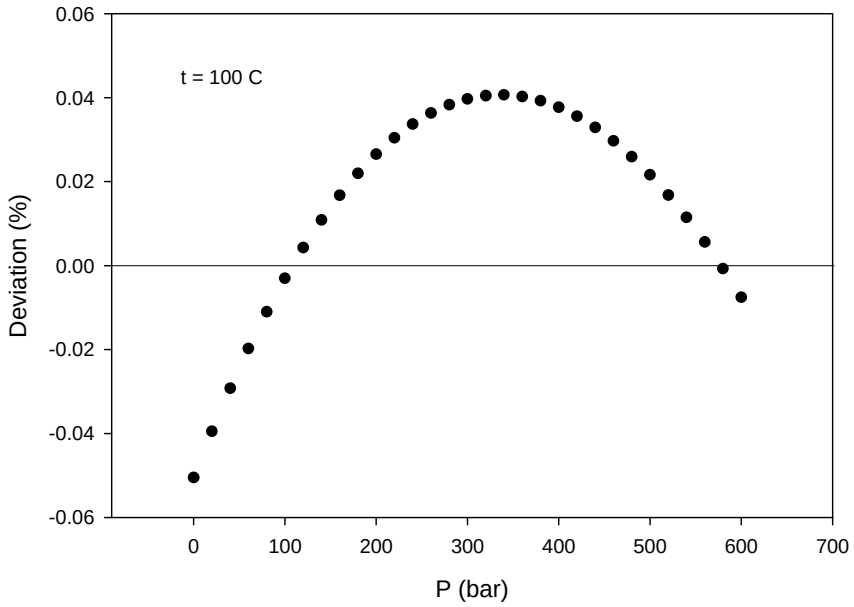

(d)

Figure 5.1: Deviations between calculated data from IAPWS09 and Eq. 1.

5.3 Viscosity of H2O+NaCl: Recently Mao and Duan [15] have done very nice viscosity modeling work for brine water (H_2O+NaCl). Their model covers *P*-*T* range of up to 1000 bar and 350 °C, and ionic strength up to 6.0 molality. Their formula can reproduce the literature values within 1% deviation. However, in their model they have used IAPWS97 for density calculations of water. Instead, to reduce the number of parameters for efficient computations of water density we recommend following equation,

$$\rho_{H_2O} = a_0 + \sum_{i=1}^{3} b_i 10^{c_i T} + \sum_{i=1}^{2} d_i P^i \qquad (2)$$

Parameters of Eq. 2 are predicted by regressing generated data from IAPWS97 and with this modification in Mao and Duan's formulation we could reproduce their values with maximum 0.1% deviation. Here *P* is in MPa. **Table 5.2** shows the parameter's values. **Figure 5.2** show these comparisons for two different temperatures 30 and 100 °C for different molalities of NaCl. From this figure we can also observe that deviation is increased (~0.1%) at higher temperatures' calculations and there is no relative variation for molality change.

Table 5.2: Coefficients of Eq. 2.

i	*a*	*b*	*c*	*d*
0	1.34136579e+02			
1		-4.07743800e+03	-5.56126409e-03	4.45861703e-01
2		1.63192756e+04	-1.07149234e-02	-4.51029739e-04
3		1.37091355e+03	-5.46294495e-04	

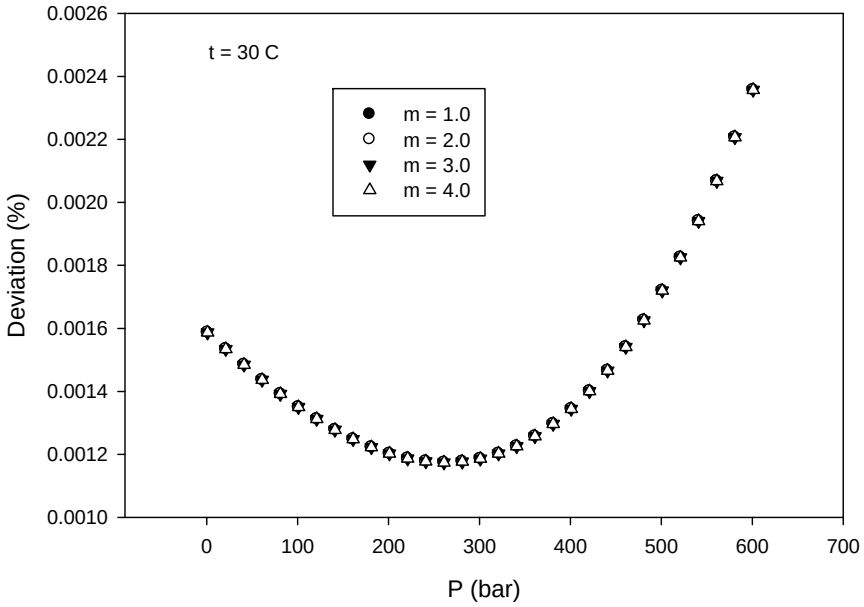

(a)

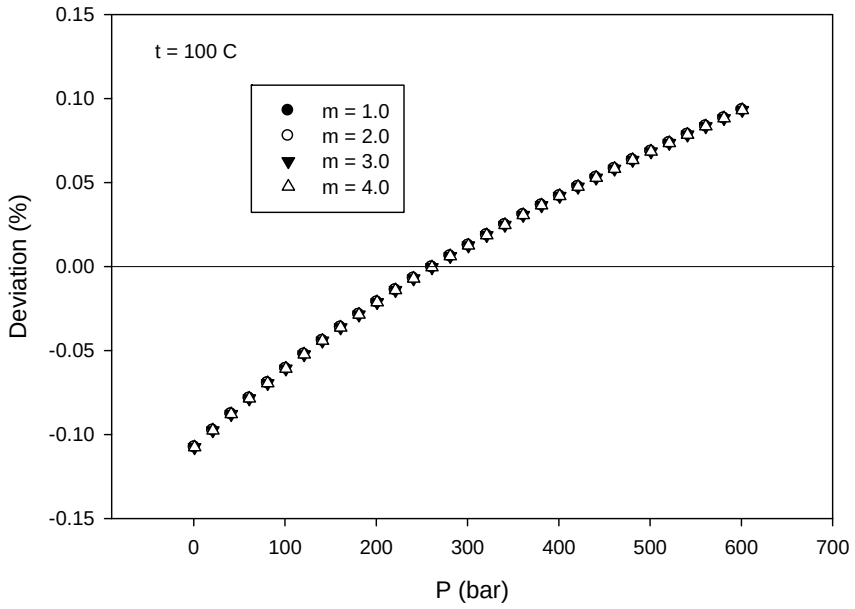

(b)

Figure 5.2: Deviations between calculated data from Mao and Duan [14], and Eq. 2.

5.4 Viscosity of H_2O+CO_2: Kumagai et al. [29] measured the viscosity of water containing up to 4.8% (wieght) CO_2 at pressure range within 400 bar and over the temperature range from 0-50 °C. They presented their experimental results only in graphical forms and therefore although there is uncertainty of picking exact numeric values from graphs, we did for our modeling purpose. After analyzing their data we have come up with the equation as follows:

$$\mu_r = 1 + \frac{\sum_{i=1}^{2} a_i x_{CO_2}^i}{\sum_{i=0}^{1} b_i T^i} \tag{3}$$

where

$$\mu_{H_2O+CO_2} = \mu_r \times \mu_{H_2O} \tag{4}$$

The parameters are reported in **Table 5.3**.

Table 5.3 Coefficients of Eq. 3**.**

i	*a*	*b*
0	7.632609119e+02	-1.047187396332e+04
1	- 9.46077673946e+03	3.6.8325597e+01

Direct experimental values from [30] were also used for data reduction process. The errors of calculated data from this model is shown in **Figure 5.3** and the maximum deviation reported is 0.68% compared to the data from Kumagai et al. (1998). Comparative results of **Figure 5.3c** were produced with respect to the data by Bando et al. (2004). The author's study clearly reveals that for the temperatures greater than 25 °C the effect of pressure on the viscosity of water with dissolved CO_2 is nil and as the temperature increases (>50 °C) the effect of dissolutions of CO_2 becomes less concerned.

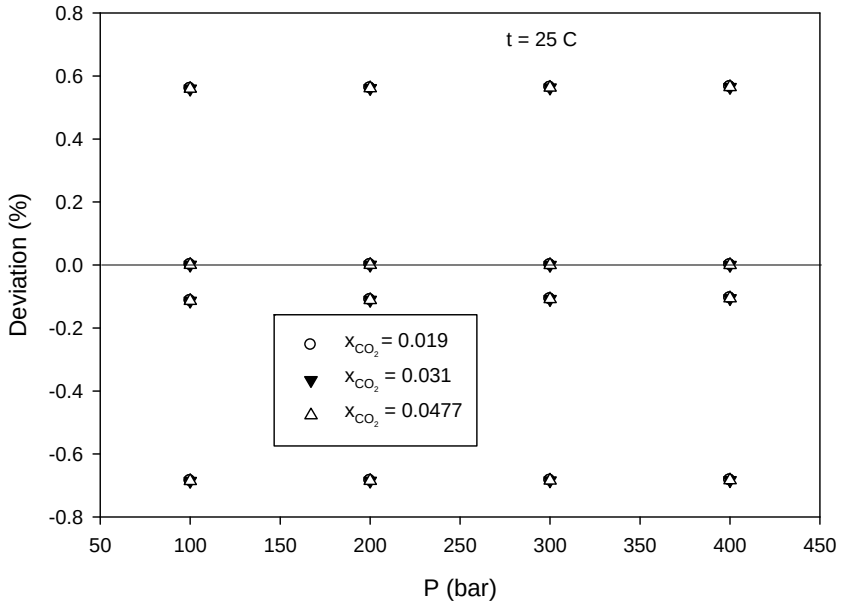

(a)

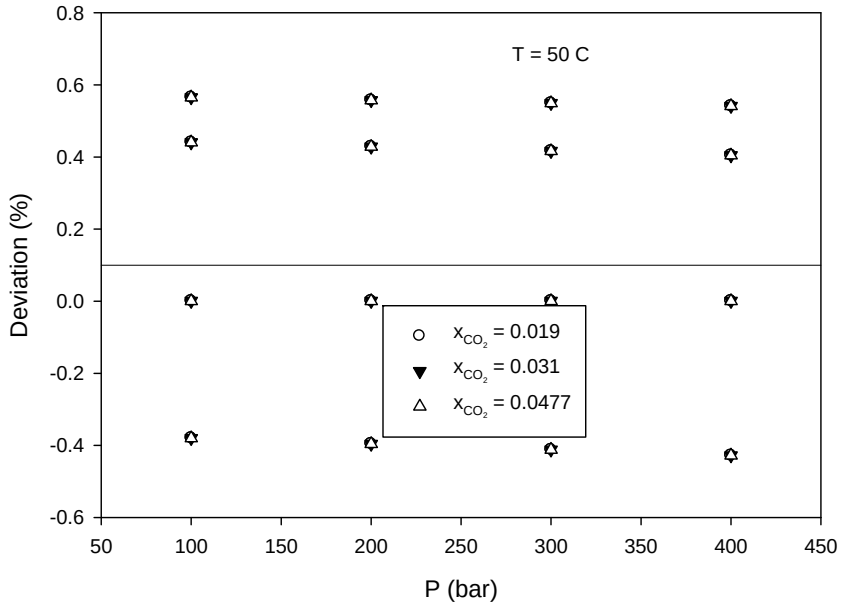

(b)

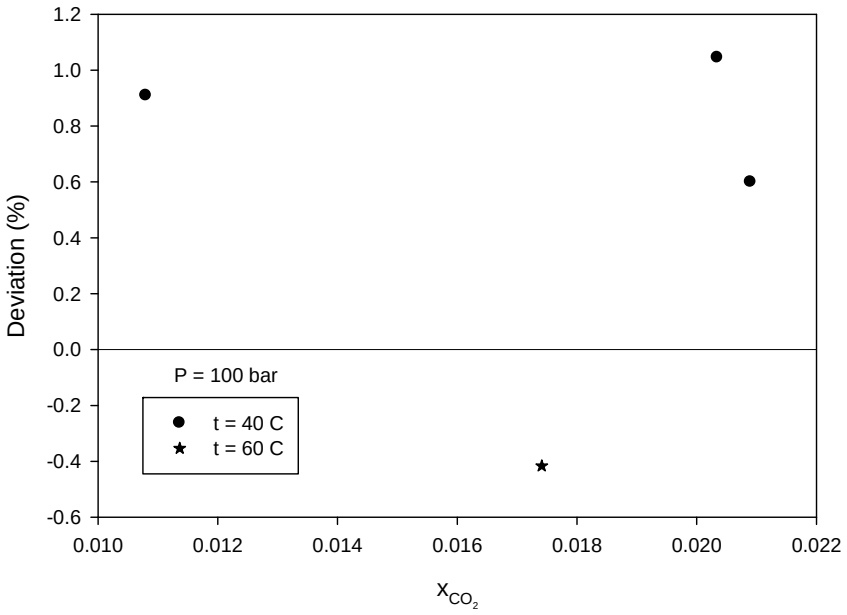

(c)

Figure 5.3: Deviations between experimental data and calculated results by Eq. 4

5.5 Viscosity of H_2O+NaCl+CO_2: We have found three literatures where effects of CO_2 dissolution on brine viscosity were investigated [30-32]. The study by Kumagai and Yokoyama [32] is not our interest because their temperature range (<5 °C) is too low. Bando et al., [30] measured the viscosity of brine solutions with dissolved CO_2 at *T-P* ranges, 30-60 °C, 100-200 bar, respectively, at a mass fraction of NaCl between 0 to 0.03. Fleury and Deschamps [31] studied the effect of dissolved CO_2 on the viscosity of three NaCl solutions covering the range of salinity usually encountered in potential CO_2 storage geological formations. They showed experimental data of viscosity variations of brine solutions for CO_2 dissolution at 35 °C and 85 bar, and found viscosity are proportional to the mole fraction of CO_2. They made a comparative study of the temperature dependence up to 100 °C with and without dissolved CO_2 with respect to the data of 35 °C they have measured. In modeling part they presented a linear relationship with respect to the mole fraction of CO_2 and however reported that the deviation of calculated results can be even on the order of 10%. Therefore to reduce discrepancies and combining with the data by Bando et al., (2004) we attempted to find a new correlation. Our new modified model is,

$$\mu_{H_2O+NaCl+CO_2} = \mu_{H_2O+NaCl}\left(1+4.65x_{CO_2}^{1.0134}\right) \tag{5}$$

$\mu_{H_2O+NaCl}$ can be measured from previous discussion at the same temperature and pressure of $\mu_{H_2O+NaCl+CO_2}$ .Comparisons of calculated data from this formulation against the experimental data are shown in **Figure 5.4 and 5.5** for different temperatures and different molalities. The divergences are very scattered, and the error is relatively high (~7%) for some data points. This is because calculated data from formulations of Bando et al., [30] and Fleury and Deschamps [31] differ by 11% at the same conditions and the uncertainty of their experimental values is around 2-3%. Still we can recommend that the Eq. 3 can be used with confidence for the mentioned *P-T* range based upon the authors' findings that pressure dependence on viscosity of brine solutions can be ignored and the effect of dissolved CO_2 is not temperature dependent.

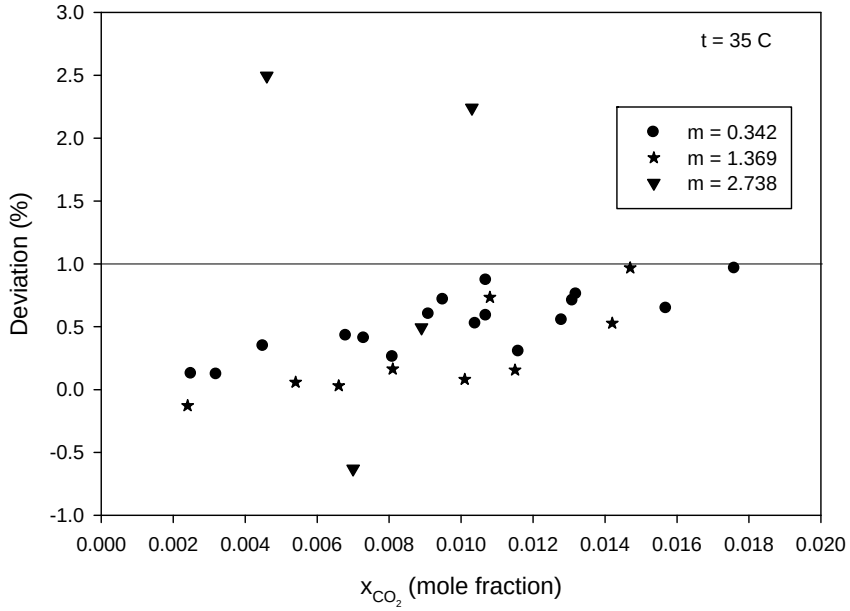

Figure: 5.4 Deviations between experimental and calculated data from Fleury and Deschamps [31], and Eq. 5, respectively.

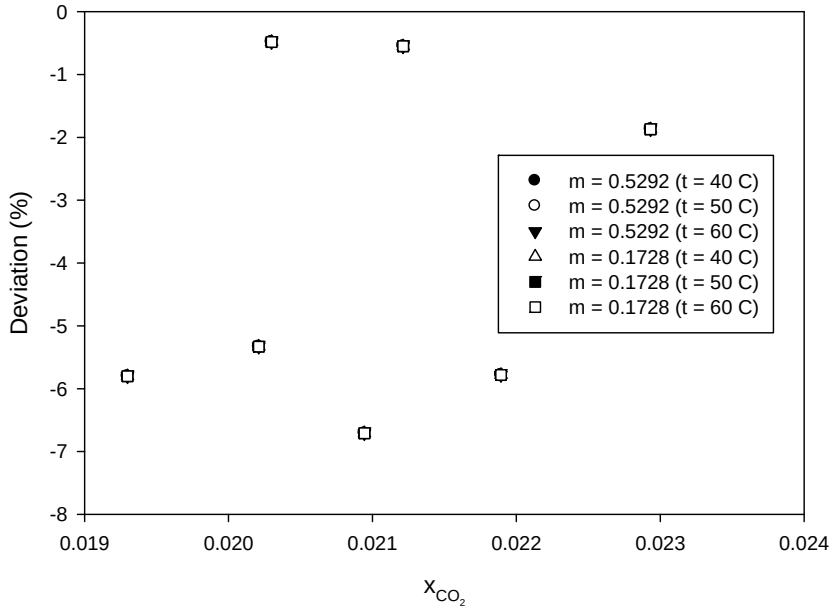

Figure 5.5: Deviations between experimental and calculated data from Bando et al. [30], and Eq. 5, respectively.

5.6 Viscosity of saline (sea) water: In addition to brine water, we also want to propose viscosity model for saline water considering typical sea water composition [33]. Practically the salinity (S) of sea water is considered to be 35 (35.16504) gkg^{-1}. Brief list of sea water components is shown in **Table 5.4** adapted from Ref [34].

Table 5.4: Sea water components (S = 35).

Salt, i	m_i, (mol/kg water)	$x_i = \frac{m_i}{\sum m_i}$
NaCl	0.424310	0.79644
Na_2SO_4	0.029245	0.054895
$NaHCO_3$	0.002418	0.004539
KCl	0.009412	0.017666
KBr	0.000854	0.001602
$MgCl_2$	0.055211	0.103630
$CaCl_2$	0.010707	0.020098
$SrCl_2$	0.000093	0.000173
H_3BO_3	0.000436	0.000139

A comprehensive literature review has been carried out on the viscosity modeling of sea water [34-43]. Most of the studies were concentrated on the viscosity measurements at atmospheric pressure for different salinity and temperature ranges. Stanley and Batten [41] performed measurements of viscosity of 35 salinity IAPO (International Association of Physical Oceanography) standard sea water for the pressure range up to 1400 bar and temperatures from 0 to 30 °C. Kobayashi and Nagashima [38] presented viscosity data of synthetic standard sea water for the temperature range 0-100 °C and for pressures up to 400 bar. Their study reveals after 20 °C, the effect of pressure can be ignored completely. The pressure dependence of the viscosity of sea water is similar to that of pure water; temperature dependence is not, however. Based upon the measured data and the viscosity values computed from the models proposed in both literature, our new formulation is exactly same as Eq. 1, but with different coefficient values. The new values are shown in **Table 5.5**. Errors of computed results by our model are shown in **Figure 5.6**. The results are satisfactory as deviations are within 0.9%.

Table 5.5: Coefficients of Eq. 1 for sea water viscosity.

i	*a*	*b*	*c*	*d*
0	2.27027348e+01			-2.08076250e-01
1		1.09512918e+04	9.89379527e-03	2.02116962e-02
2		9.59424756e+08	4.38767404e-02	-2.80171705e-04
3		-8.60130112e+08	4.41842469e-02	1.19302430e-06

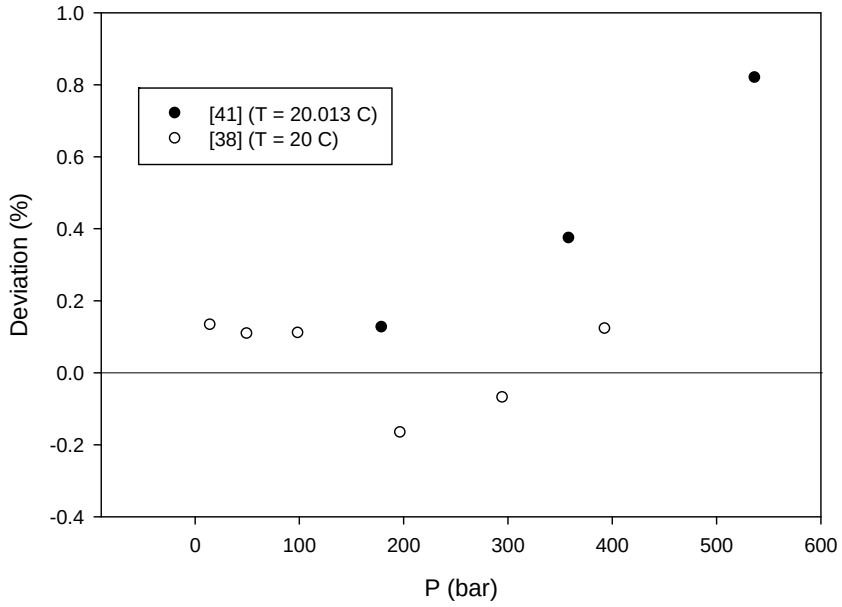

(a)

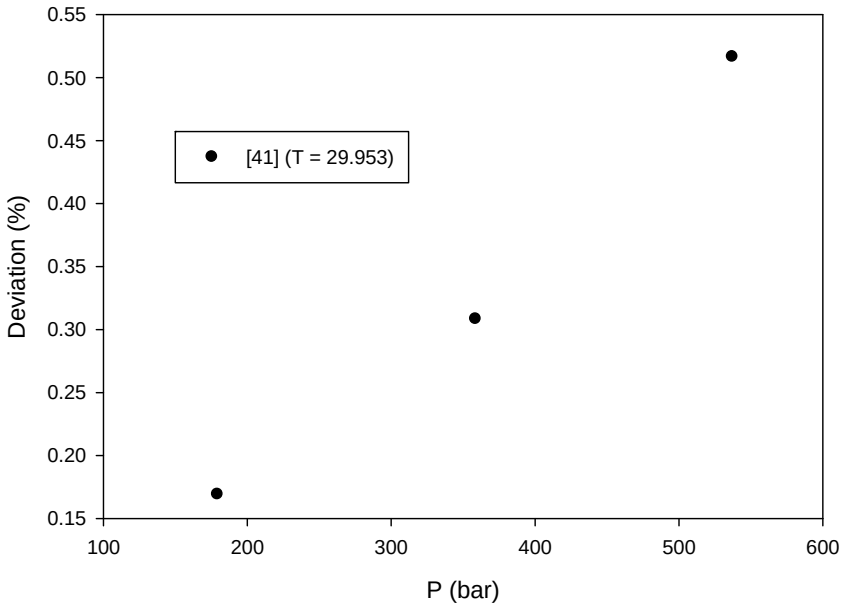

(b)

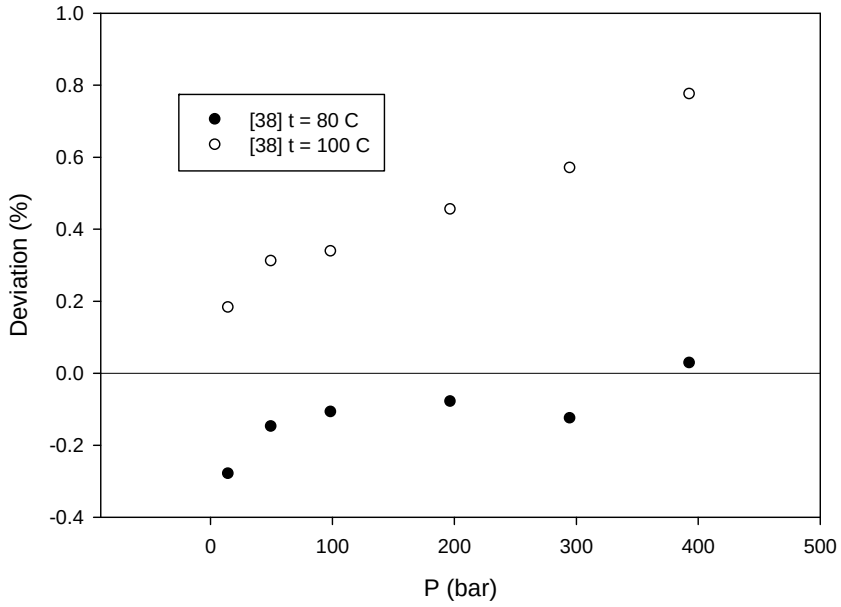

(c)

Figure 5.6: Deviations between experimental and calculated data of sea water viscosity.

5.7 Effects of dissolved CO_2: In this section we will discuss effect of dissolved CO_2 on the viscosity of aqueous phase based upon the models established. **Figure 5.7** show computed

viscosity values of H_2O (pure water), H_2O+NaCl (brine water), H_2O+CO_2, H_2O+NaCl+CO_2, and sea water with respect to temperatures at three different pressures 50, 200, and 600 bar, at molality m = 1, and CO_2 mass fraction x_{CO_2} = 0.02. The mass fraction was chosen within the solubility range of CO_2 in pure water and brine [5, 44]. From these figures it is observed that at lower temperature (<40 °C) consequence of CO_2 dissolution in pure water's viscosity is relatively high and that tends to diminish as temperature increases. For instance, at t = 20 °C, viscosity of water with 2% (weight) dissolved CO_2 is around 6% higher than pure water while at 100 °C, this amount is 0.6%. This finding is consistent with the results by Ref [32]. PVT behavior of aqueous solution with dissolved CO_2 is also same like this [19].

Neglecting CO_2's presence in brine water will warrant large error because as seen in the figures, at any particular temperature and pressure viscosity of brine water of having 1 molal NaCl with mentioned amount of CO_2 dissolved is more than 8% higher than with no CO_2. This percentage will increase with the concentration or molality of NaCl. Phase behavior of CO_2 in brine is also steady with this [44]. Effect of CO_2 in sea water is not tangible because no such literature was found and therefore, no model could be developed.

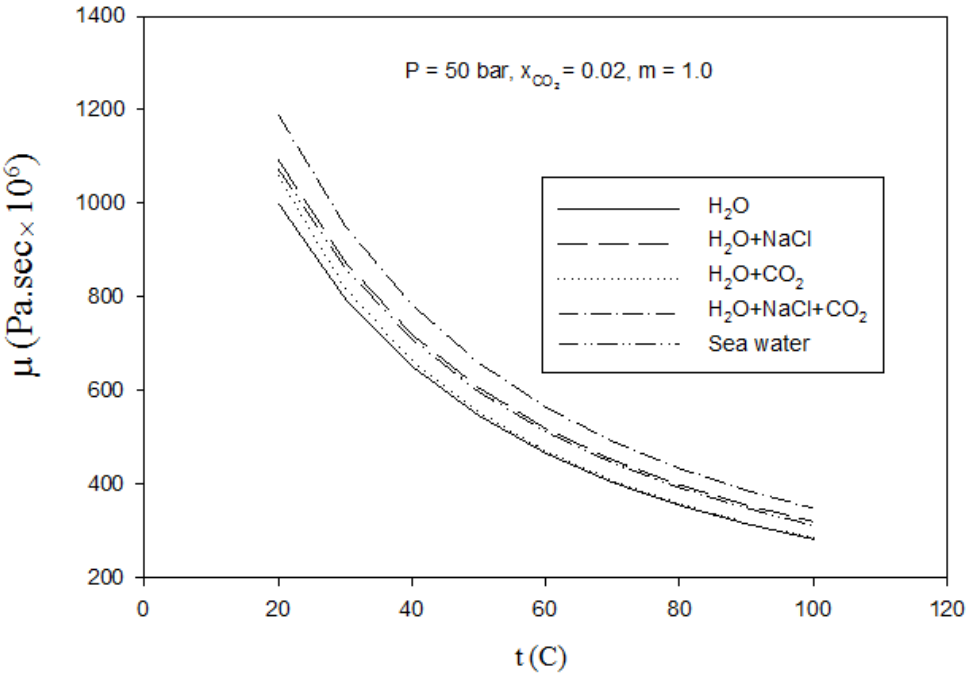

(a)

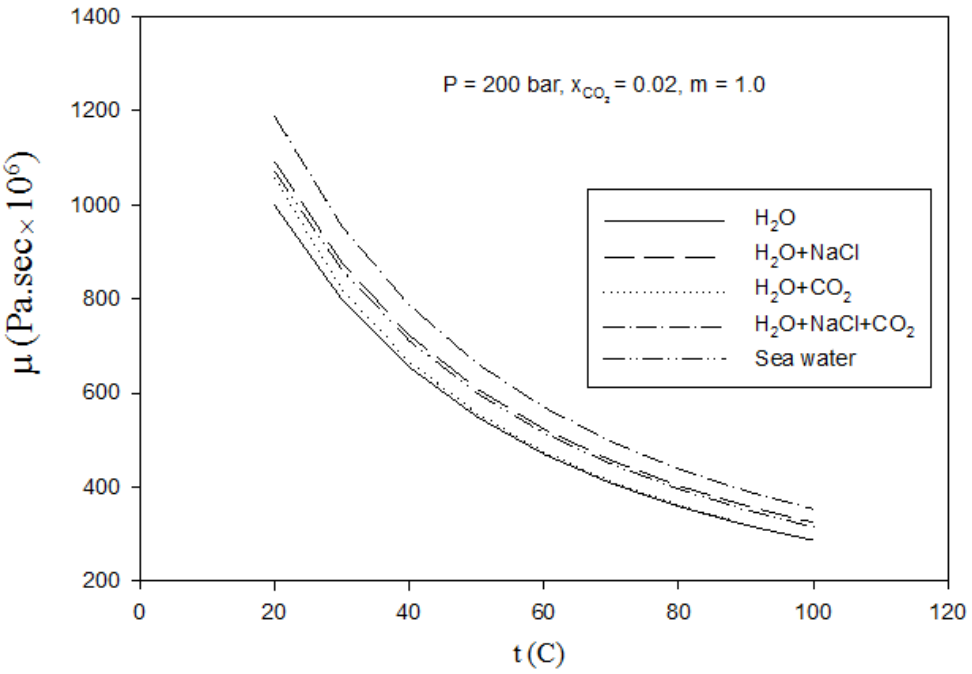

(b)

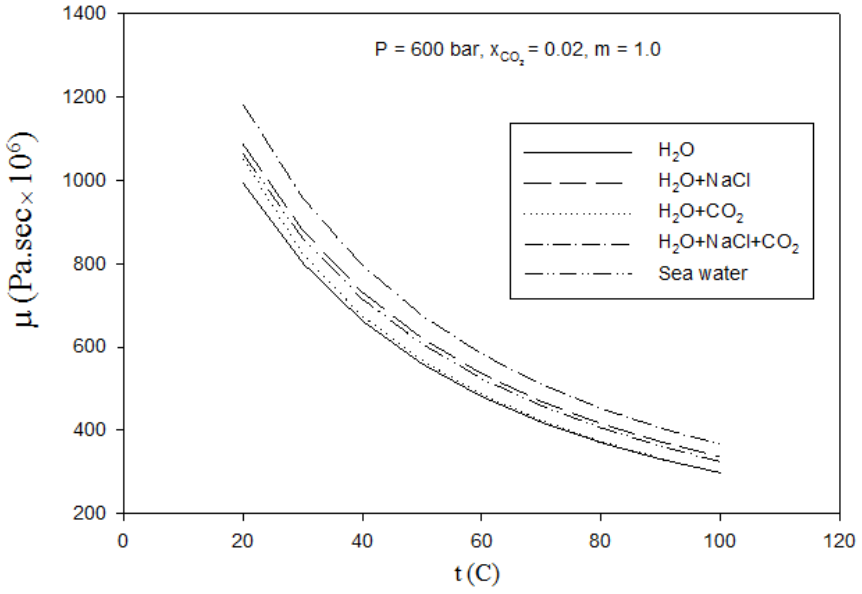

(c)

Figure 5.7: Viscosity of aqueous solution

5.8 Concluding Remarks: We have observed one common feature for the models proposed that percentage of deviation remains same at any particular temperature and pressure irrespective of NaCl molality or CO_2 composition. This will give more confidence in using our simpler formulations. Moreover, literature values could be reproduced with less than 1% deviation except some cases where high (2-3%) experimental uncertainty was reported and the computed values from previous models differed around 10%. All possible combinations of viscosity models for the geologic simulation of CO_2 are discussed and the effects of dissolved CO_2 are narrated elaborately. Since the models have less number of parameters will also help increase computational efficiency for the simulation of geologic sequestration of CO_2.

5.9 Nomenclatures:

t	Temperature (°C)
T	Temperature (K)
P	Pressure (bar, if not specified)
μ	Dynamic viscosity (micro Pascal.sec)
ρ	Density (kg/m^3)
lit	literature
cal	calculated

5.10 References:

[1] Herzog, H., Golomb, D., Carbon Capture and Storage from Fossil Fuel Use. *Encyclopedia of Energy*, Elsevier Inc., 2004.

[2] Dirik, I., Altintas, A., Bulbul, S., Gumrah, F., *Analytical Modeling of CO_2 Sequestration in Saline Aquifers*, 5th Canadian International Petroleum Conference, Calgary, Alberta, Canada, June 8-10, 2004; Calgary, Alberta, Canada, 2004.

[3] Herzog, H.J., What Future Carbon Capture and sequestration. *Environmental Science & Technology* April, 2001, 38, 148A-153A.

[4] Islam, A.W., Carlson, E.S., *A Fully Non-iterative Technique for Phase Equilibrium and Density Calculations of CO_2+Brine System and an Equation of State for CO_2*, 37th Stanford Geothermal Workshop, Stanford University, CA, Jan 30-Feb 1, 2012; Stanford University, CA, 2012.

[5] Islam, A.W., Carlson, E.S., *Fluid Phase Equilib. 321,* 17-24, 2012.

[6] Islam, A.W., Carlson, E.S., Application of Liquid State Models for the Time Efficient Phase Equilibrium Calculations of Supercritical CO_2 and H_2O at High Temperatures and Pressures. (in *review*)

[7] Class, H., *Models for non-isothermal compositional gas-liquid flow and transport in porous media*. Stuttgart, 2007.

[8] Davani, E., Ling, K., Teodoriu, C., Mccain Jr., W.D., Falcone, G., *More Accurate Gas Viscosity Correlation for Use at HPHT Conditions Ensures Better Reservoir Estimation*, SPE Annual Technical Conference and Exhibition New Orleans, Louisiana, October 4-7, 2009; New Orleans, Louisiana, 2009.

[9] Hernandez, J.C., Vesovic, V., Carter, J.N., Lopez, E., *Sensivity of Reservoir Simulations to Uncertainties in Viscosity*, SPE/DOE Improved Oil Recovery Symposium, Tulsa, Oklahoma, April 13-17, 2002; Tulsa, Oklahoma, 2002.

[10] Hassanzadeh, H., Pooladi-Darvish, M., Elsharkawy, A. M., Keith, D. W., Leonenko, Y., *Int J Greenhouse Gas Control, 2,* 65-77, 2008.

[11] Pruess, K. *ECO2N: A TOUGH2 Fluid Property Module for Mixtures of Water, NaCl, and CO_2.*; Earth Science Division, Lawrence Berkeley National Laboratory, University of California: Berkeley, CA 94720, 2005.

[12] Ozgur, E.; Gumrah, F., *Energy Sources, Part A, 32,* 674-687, 2010.

[13] Piri, M., Prevost, J.H., Fuller, R., *Carbon Dioxide Sequestration in Saline Aquifers: Evaporation, Precipitation and Compressibility Effects.*, Fourth Annual Conference on Carbon Capture and Sequestration DOE/NETL, Pittsburgh, 2005; Pittsburgh, 2005.

[14] Lu, C., Litchtner, P.C., *Journal of Physics: Conference Series, 78,* 012042, 2007.

[15] Mao, S., Duan, Z., *Int. J. Thermophys, 30,* 1510-1523, 2009.

[16] Lindeberg, E., Wessel-Berg, D., *Energy Conv Mgmt., 38,* S229-S234, 1997.

[17] Hassanzadeh, H., Pooladi-Darvish, M., Keith, D.W., *J Can Petrol Technol., 44,* 44, 43-51, 2005.

[18] Tumasjan, A.B., Panteleev, V.G., Mecncer, G.P., *Nefteprom, 2,* 20-23, 1969.

[19] Spycher, N., Pruess, K., Ennis-King, J., *Geochim et Cosmochim Acta*, *67,* 3015-3031, 2003.

[20] *ASME Steam Table*. 1967.

[21] Hendricks, R.C., McClintock, R.B., Silvestri, G., *ASME J Eng Power, 99*, 664-679, 1977.

[22] Kestin, J., Whitelaw, J.H., *ASME J Eng. Power, 88,* 82-104, 1966.

[23] Nagashima A., *J Phys. Chem Ref Data,* 6, 1133-1176, 1977.

[24] Kestin, J., *Water and Steam: Their Properties and current industrial applications: proceedings of the Ninth International Conference on the Properties of Steam*, Munich, 10-14 September, 1980; Straub, J.; Scheffler, K., Eds. Munich, 1980.

[25] Sengers, J.V., Watson, J.T.R., *J Phys Chem Ref Data, 15,* 1291-1314, 1986.

[26] *IAPWS, Revised Release on the IAPS Formulation 1985 for the Viscosity of Ordinary Water Substance,* 2003.

[27] Huber, M.L., Perkins, R.A., Laesecke, A., Friend, D. G., *J Phys Chem Ref Data, 38,* 101-125, 2009.

[28] Wagner, W., Cooper, J.R., Dittmann, A., Kijima, J., Kretzschmar, H.-J., Kruse, A., Mares, R., Oguchi, K., Sato, H., Stocker, I., Sifner, O., Takaishi, Y., Tanishita, I., Trubenbach, J., Willkommen, T., *ASME Transac, 122,* 150-182, 2000.

[29] Kumagai, A., Kawase, Y., Yokoyama, C., *Review of Scientific Instruments, 69,* 1441-1444, 1998.

[30] Bando, S., Takemura, F., Nishio, M., Hihara, E., Akai, M., *J Chem Eng Data, 49,* 1328-1332, 2004.

[31] Fleury, M., Deschamps, H., *J Chem Eng Data, 53,* 2505-2509, 2008.

[32] Kumagai, A., Yokoyama, C., *J Chem Eng Data, 44,* 227-229, 1999.

[33] Millero, F.J., Feistel, R., Wright, D.G., McDougall, T.J., *Deep Sea Res I, 55,* 50-72, 2008.

[34] Leyendekkers, J.V., *Desalination, 29,* 263-274, 1979.

[35] Chen, S.F., Chan, R.C., Read, S.M., Bromley, L.A., *Desalination, 13,* 37-51, 1973.

[36] Horne, R.A., Johnson, D.S., *J Geophys Res., 71,* 5275-5277, 1966.

[37] Isdale, J.D., Spence, C.M., Tudhope, J.S., *Desalination, 10*, 319-328, 1972.

[38] Kobayashi, K., Nagashima, A., *High Temperatures-High Pressures, 17,* 131-137, 1985.

[39] Leyendekkers, J.V., *J Soln Chem., 8,* 853-869, 1979.

[40] Phang, S., *Malaysian J Sci., 4,* 81-88, 1976.

[41] Stanley, E.M., Batten, R.C., *J Geophys Res., 74,* 3415-3420, 1969.

[42] Sharqawy, M.H., Lienhard V, J.H., Zubair, S.M., *Desalination and Water Treatment, 16,* 354-380, 2010.

[43] Mattthaus, V.W., *Beitrage zur Meereskunde, 29,* 93-107, 1972.

[44] Spycher, N., Pruess, K., *Geochim et Cosmochim Acta, 69,* 3309-3320, 2005.

CHAPTER SIX

†Numerical experiments of double diffusion natural convection of carbon dioxide in brine saturated porous media

[1]Akand W. Islam, [2]Muhammad A. R. Sharif, [1]Eric S. Carlson
[1]Department of Chemical and Biological Engineering
[2]Department of Aerospace Engineering and Mechanics
The University of Alabama, Tuscaloosa, AL 35487, USA

Abstract: Double diffusive natural convection of carbon dioxide in two-dimensional cavities filled with brine saturated porous media is numerically investigated in this study. Vertical gradients of carbon dioxide concentration and temperature are imposed across the height of the cavity. The objective is to understand the stabilization of carbon dioxide concentration through natural convection process over long period of time after sequestration into subsurface porous media aquifer. The problem parameters are the solutal Rayleigh number ($100 \leq Ra_s \leq 10000$), the buoyancy ratio ($2 \leq N \leq 100$), the equivalent thermal Rayleigh number (Ra_T) based on the buoyancy ratio, the cavity aspect ratio ($0.5 \leq A \leq 2$), and a fixed Lewis number ($Le = 301$). The effects of the governing parameters on the advancement of carbon dioxide fronts from the top gas-liquid interface to the bottom of the aquifer are analyzed. Required inputs for the simulations are chosen carefully through extensive literature search. The governing equations consist of conservation of mass, momentum (Darcy's law of flow through porous media), species (carbon dioxide), and energy (temperature). A set of elliptic parabolic equations in non-dimensional form are obtained which are solved numerically using the point Gauss-Siedel (PGS) and alternating direction implicit (ADI) methods. Because numerical computations do not exhibit onset of natural convection for homogeneous initial conditions, a sinusoidal small perturbation of the CO_2 concentration is therefore induced at the top face of the domain. It is found that the CO_2 plumes move faster when Ra_s is increased, however slow down with decreasing N. For every simulation run, the average CO_2 dissolution ($\overline{S} = \frac{\sum_{i}^{n_i}\sum_{j}^{n_j} c_{i,j}}{n_i \times n_j}$) in the reservoir is computed. At early stage ($\leq$ 10 years) of the convection process, the CO_2 dissolutions are same for all cases studied. After 500 years the dissolution is found to be around 0.63 for $N = 100$, and around 0.47 for $N = 2$, respectively. After 2000 years the dissolution rate is extremely slow. When the reservoir aspect

ratio (A) is changed, the dissolution rate changes slightly. The rate is slightly higher in laterally wide reservoir, which makes it better candidate than the deeper aquifer from the context of CO_2 sequestration.

Key Words: double diffusion, natural convection, carbon dioxide, brine, porous media

† *Geothermics* (*in review*)

6.1 Introduction: In order to curb carbon emissions, the use of technologies to capture and store CO_2 has rapidly emerged as an important physically and economically viable method these days. Geological storage involves injecting CO_2 into a saline aquifer. It promises to reduce the cost of achieving deep reductions in CO_2 emissions over the next few decades [1]. When CO_2 is injected into an aquifer, the competition between viscous, capillary, and buoyancy forces determines the flow pattern. Eventually CO_2 will migrate upward due to buoyancy forces and be trapped under the cap rock and over the aquifer top surface. Hence an interface between a CO_2-rich phase and brine exists, [2] and dissolution of CO_2 into brine starts by molecular diffusion increasing the brine density [3] on the aquifer top surface. This density increase together with the naturally occurring temperature gradient (typically ~3 °C/100 meter) results in destabilizing the CO_2-brine interface and accelerate the transport rate of CO_2 into the aquifer by natural convection. The geothermal gradient is compensated partially by the geopressure gradient [4] (normally ~10 bar/100 meter). The convective mixing enhances dissolution of CO_2 through continuously removing CO_2-saturated brine from the region adjacent to the CO_2 on top and brings under-saturated brine into contact with the downward advancing CO_2 plume. Thus, it is very important to quantify the rate of dissolution and understand the transport mechanism correctly because the timescale (hundreds to thousands of years) for dissolution corresponds to the timescale over which free phase CO_2 may warrant leaking out [5]. This chance of leaking reduces when a significant amount of CO_2 dissolves into the brine.

Comprehensive investigations have been carried out on double-diffusive convection where heat and solute being the diffusive components [6, 7]. An extensive work has been done in the context of porous media, especially related to the environmental problems and the transport of contaminants [8-12]. Studies have also been found investigating stability analysis for the onset time for convection, the preferred wavelength for the growth of convective fingers, growth rates, and solutal and thermal effects [11, 13-15] The use of modeling and simulation to make predictions on the timescale is obviously impossible to validate, since even in a field operation one cannot history match more than a small amount of the relevant time period [16].

In this paper the double-diffusive convection of CO_2 in brine under vertical thermal and solutal gradients is numerically studied considering reservoir conditions suitable to geologic

sequestration. Realistic simulation inputs, obtained through extensive literature review, are provided for the computations. Results are presented graphically in terms of the propagation of the CO_2 front through the aquifer with time for various cavity configurations ($0.5 \leq A \leq 2$) and for a range of the solutal Rayleigh number ($100 \leq Ra_s \leq 10000$) and buoyancy ratio ($2 \leq N. \leq 100$). The effects of variation of these geometric and hydrodynamic parameters on the CO_2 front propagation are analyzed and evaluated.

6.2 Description of the problem and the governing equations: The geometry under consideration is a two-dimensional rectangular cavity reservoir, sketched in **Figure 6.1**, filled with porous medium saturated with brine (H_2O+NaCl), with a height H and length L. The permeability of the porous medium is φ. Initially the fluid is at rest and there is no CO_2 dissolved. Boundary conditions are no fluid flow across all boundaries and no solute fluxes across lateral and bottom boundaries at all time. Also there is no heat flux across the lateral boundaries while the top and bottom boundaries are maintained at isothermal cold and hot temperatures, respectively. We assume that CO_2-liquid interface is relatively sharp and fixed at the top boundary; meaning pressure change due to dissolution is negligible. This approximation is reasonable below a depth of 1000 m which is the usual case of geologic sequestration [17]. The brine is initially quiescent and the medium is homogeneous in terms of porosity and permeability. The presence of a capillary transition zone between the gas and the brine phase is disregarded. Therefore only the liquid phase is modeled and the presence of the gas phase at the top is represented by a boundary condition for the liquid phase. The Boussinesq approximation and Darcy flow model are assumed valid. Moreover, we assume that velocity-based dispersion and capillary effects are negligible and that geochemical reactions are not occurred. We only expect a laminar flow regime since Rayleigh number is low. Boundary conditions for the temperature are opposite to concentration. Because the geo-temperature at the bottom of the reservoir is higher than that at the top, the actual temperature difference varies from place to place. The density gradient owing to concentration and temperature variations are the source of natural convection here. For such a system, the governing equations of flow and concentration field are:

(a) Continuity equation

$$\frac{\partial \rho}{\partial t}+\frac{\partial\left(\rho u_x\right)}{\partial x}+\frac{\partial\left(\rho u_z\right)}{\partial z}=0 \tag{1}$$

(b) Darcy's law

$$u_x=-\frac{k}{\mu}\frac{\partial p}{\partial x}, \tag{2}$$

$$u_z=-\frac{k}{\mu}\left(\frac{\partial p}{\partial z}-\rho g\right) \tag{3}$$

(c) Concentration transport equation

$$\frac{\varphi \partial c}{\partial t}+u_x\frac{\partial c}{\partial x}+u_z\frac{\partial c}{\partial z}=\varphi D\left(\frac{\partial^2 c}{\partial x^2}+\frac{\partial^2 c}{\partial z^2}\right) \tag{4}$$

For small density variations due to temperature and concentration changes at constant pressure, the brine density is a linear function of temperature and concentration of solute as given by

$$\rho=\rho_0\left[1+\beta_c\left(c-c_0\right)+\beta_T\left(T-T_0\right)\right] \tag{5}$$

Where

$$\beta_c=\frac{1}{\rho_0}\left[\frac{\partial \rho}{\partial c}\right]_T \quad \text{and} \quad \beta_T=\frac{1}{\rho_0}\left[\frac{\partial \rho}{\partial T}\right]_c \tag{6}$$

and we obtain

$$\frac{\partial \rho}{\partial x}=\rho_0\left[\beta_c\frac{\partial c}{\partial x}+\beta_T\frac{\partial T}{\partial x}\right] \tag{7}$$

After eliminating the pressure by cross-differentiation of equations (2) and (3) we get

$$\frac{\partial u_z}{\partial x}-\frac{\partial u_x}{\partial z}=\frac{kg\rho_0}{\mu}\left[\beta_c\frac{\partial c}{\partial x}+\beta_T\frac{\partial T}{\partial x}\right] \tag{8}$$

(d) Energy equation:

$$\rho_0 C_p \left(\frac{\partial T}{\partial t} + u_x \frac{\partial T}{\partial x} + u_z \frac{\partial T}{\partial z} \right) = \kappa \left(\frac{\partial^2 T}{\partial x^2} + \frac{\partial^2 T}{\partial z^2} \right) \tag{9}$$

The equations to be solved are Eqs. (1), (4), (8), and (9) to obtain u_x, u_z, c and T.

6.2.1 Dimensionless form of the equations

Considering the cavity height, H, as the characteristic length and $\varphi D/H$ as the characteristic velocity following dimensionless variables are defined,

$$\begin{aligned}
&x^* = \frac{x}{H},\ z^* = \frac{z}{H},\ u_x^* = \frac{Hu_x}{\varphi D},\ u_z^* = \frac{Hu_z}{\varphi D}, \psi^* = \frac{\psi}{\varphi D} \\
&t^* = \frac{Dt}{H^2},\ c^* = \frac{c - c_r}{c_0 - c_r},\ T^* = \frac{T - T_r}{T_0 - T_r},\ u_x^* = -\frac{\partial \psi^*}{\partial z^*},\ u_z^* = \frac{\partial \psi^*}{\partial x^*} \\
&Ra_s = \frac{\Delta \rho_c g k H}{\varphi D \mu},\ Ra_T = \frac{\Delta \rho_T g k H}{\mu \alpha},\ Le = \frac{\alpha}{\varphi D}.
\end{aligned} \tag{10}$$

After applying the Boussinesq approximation the final forms of dimensionless equations are

$$\frac{\partial^2 \psi^*}{\partial x^{*2}} + \frac{\partial^2 \psi^*}{\partial z^{*2}} = Ra_s \left(\frac{\partial c^*}{\partial x^*} - \frac{1}{N} \frac{\partial T^*}{\partial x^*} \right) \tag{11}$$

where the buoyancy ratio N is defined as $N = -\dfrac{\beta_c \Delta c}{\beta_T \Delta T}$ and,

$$\frac{\partial c^*}{\partial t^*} + u_x^* \frac{\partial c^*}{\partial x^*} + u_z^* \frac{\partial c^*}{\partial z^*} = \frac{\partial^2 c^*}{\partial x^{*2}} + \frac{\partial^2 c^*}{\partial z^{*2}}. \tag{12}$$

Energy equation

$$\frac{\partial T^*}{\partial t^*} + U_x^* \frac{\partial T^*}{\partial x^*} + U_z^* \frac{\partial T^*}{\partial z^*} = \frac{1}{\mathrm{Pr}} \left(\frac{\partial^2 T^*}{\partial x^{*2}} + \frac{\partial^2 T^*}{\partial z^{*2}} \right) \tag{13}$$

Here $U_x^* = \varphi u_x^*,\ U_z^* = \varphi u_z^*,$ and $\mathrm{Pr} = \dfrac{\rho_0 C_p D}{\kappa}$.

6.2.2 Boundary and initial conditions

The initial condition is,

$$\text{at } t^* = 0\ \ \psi^* = 0,\ c^* = 0, T^* = 0. \tag{14}$$

The boundary conditions are shown in **Figure 6.1**,

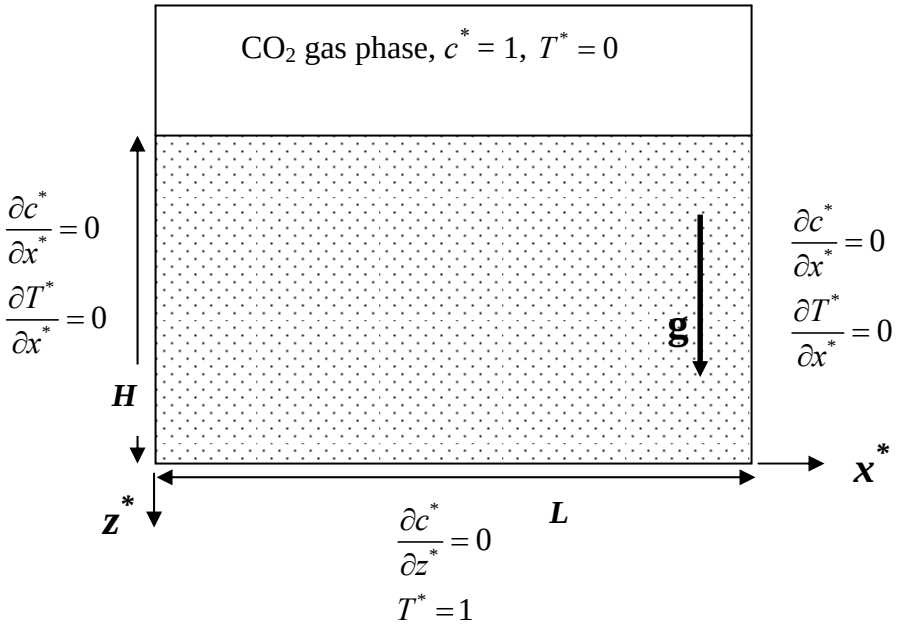

Figure 6.1: Schematic diagram of our hypothetical reservoir model

6.3 Numerical Method: Numerical simulation of density-driven transport problem Equations (12) and (13) is very sensitive to discretization errors. The following criteria must be fulfilled for the stability of the transport equations given by [18]

$$C_R = \frac{u^* \Delta t^*}{\varphi \Delta x^*} \leq \frac{P_E}{2} \tag{15}$$

where $P_E = \frac{u^* \Delta x^*}{D\varphi}$. The simulation was performed with 81×81 uniform rectangular grid cells for the cavity with aspect ratio of unity, and time step (Δt^*) was taken as 10^{-6} (equivalent to ~29 days based on H = 100 m) to meet above conditions. A sequential solution procedure was used to solve the elliptic Poisson equation (11) and the concentration and temperature transport equations (12) and (13). Equation (11) is solved by Point Gauss-Sidel iterative method with convergence criteria of $\sum abs\left(\frac{\psi^{i+1}-\psi^i}{\psi^i}\right) < 10^{-6}$ where the superscript i denotes iteration step number. Equations (12) and (13) are solved using the Alternating Direction Implicit (ADI) method where the convection terms are discretized using the upwind differencing and the

diffusion terms are discretized using the central differencing. The developed code was checked with the literature benchmark solutions [1, 19] and the results are in satisfactory agreement with the published simulations independent of the number of grid cells. It is required that the interface be perturbation in order to observe the downward propagation of the finger like concentration fronts. Therefore a sinusoidal perturbation is used on the top interface in the form

$$c^*(x^*, z^* = 1, t^* = 0) = 1 + 0.01 \sin(2\pi \mathrm{n} x^*) \tag{16}$$

where the wave number (n) of 24 is used.

Basically the long term behavior is not dependent on the initial perturbation [20]. Moreover, the growth of the perturbations is a weak function of the wavelength. Pore-level perturbations and thermo-mechanical fluctuations cause the perturbation to start the finger like plumes in reality [21, 22] Pore-level instabilities [23] is ignored here, however.

The important assumptions in this study are the homogeneity and isotropy of the porous medium. The effect of velocity-induced dispersion is ignored and the flow field as single-phase is considered. Additionally other mechanisms like, precipitation and geochemical reactions are not accounted for simplicity.

6.4 Results and discussion: The double diffusion is imposed here through the buoyancy ratio (N) which was varied between 2 and 100. This represents vast differences of geothermal gradients. The geothermal gradient is not same everywhere; for instance, very high gradient can be observed as 20 °C/100 m at the Mid-Atlantic Rift, whereas in Iceland there is almost no gradient (~ 0 °C/100 m) [24]. The direction of the flow due to thermal buoyancy forces is anticlockwise because temperature at the bottom of the reservoir is always higher than at the top. On the other hand, the flow owing to concentration gradient is clockwise, opposing the thermal flow. The solutal Rayleigh number, Ra_s, is varied between 100 - 10000. The porosity (φ) of a typical reservoir,[7] of 0.30, and recently reported [25] diffusion coefficient (D) of brine filled porous media, of 4×10^{-9} m^2/s, respectively, are taken for calculations. In order to calculate the Prandtl number, Pr, in the energy equation, the required inputs are collected from Sharqawy et al [26]. Pr is calculated to be as 0.0062. To understand the natural convection of different reservoir

shapes, the aspect ratio (A) is changed from 0.5 to 2. The thermal diffusivity (α) is considered constant assigning the value 3.7×10^{-7} m^2/s.[13] Hence, the Lewis number, *Le*, is fixed at 310. To discuss the results in terms of a combination of the solutal Rayleigh number, Ra_s, and the buoyancy ratio, N, the equivalent Rayleigh number, Ra_e, expressed as

$$Ra_e = Ra_s\left(1+\frac{1}{N}\right) \tag{17}$$

is introduced.

6.4. 1. Effects of Ra_s and N

First, various scenarios of varying Ra_s from low (100) to relatively high (10000) and N from 2 to 100 for the case of A = 1 (square shape) are discussed. **Figure 6.2** shows the concentration distribution for Ra_s = 100 and N = 100 where only the top 20% of the vertical domain is included. The corresponding Ra_e for this case is 99. By definition [Equation (17)] Ra_e does not change significantly unless N is low and close to 1. Equation (17) also implies that when the buoyancy ratio is higher, the thermal effect on CO_2 dissolution is relatively minor. When Ra_e is low (such as 99), even though the induced perturbations at the top interface initiate very tiny convection cells, they cannot survive as the time marches. For low Ra_e the dissolution is completely diffusion dominated and therefore propagation of CO_2 concentration front into brine is extremely slow. This is unfavorable because in such case CO_2 will have to be trapped over the aquifer for a very long time (thousands of years) and may caveat leakage through the permeable zone. Average dissolution (or concentration) of CO_2 in the model reservoir is defined as

($\bar{S} = \frac{\sum_{i}^{n_i}\sum_{j}^{n_j} c_{i,j}}{n_i \times n_j}$). After about 4 years the average dissolution is 0.016 while after 100 years the average dissolution is 0.046. After 500 years the aquifer will be only 0.094 CO_2 concentrated. During early periods, CO_2 dissolves in the brine slowly and as time passes the diffusion dominated dissolution rate is slightly enhanced.

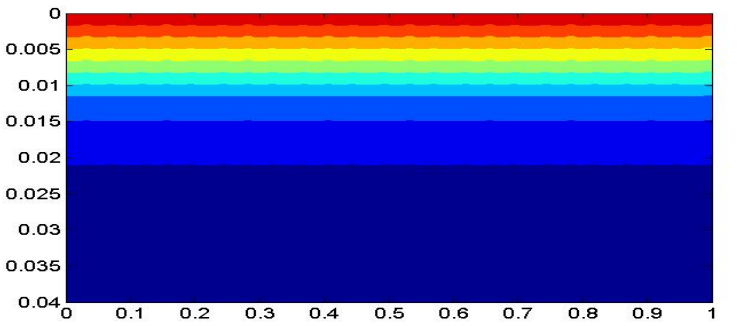

(a)

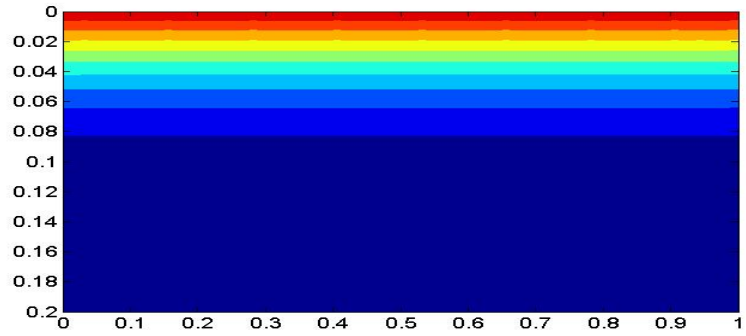

(b)

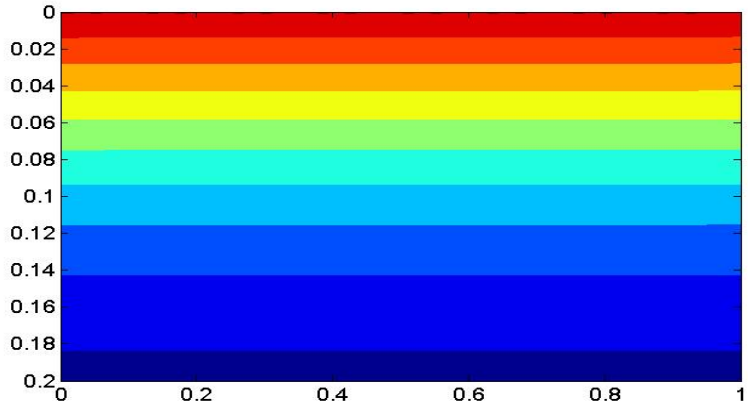

(c)

Figure 6.2: Concentration profiles for Ra_s = 100, N = 100, at (a) t = 4, (b) t = 100, and (c) t = 500 years.

When N is decreased to 50, the Ra_e becomes 98 and correspondingly produces almost the same concentration distribution for Ra_e = 99 as shown in **Figure 6.2**. When the thermal buoyancy effect is increased by substantially decreasing N (= 2), the Ra_e decreases to 50. At this very low equivalent Rayleigh number, CO_2 dissolution is extremely slow.

The CO_2 propagation over the time is shown in **Figure 6.3** when Ra_s is increased to 1000 with N = 100 producing Ra_e of 990. In this case we see that, even up to 100 years the concentration front propagation is primarily diffusive and therefore the average dissolution reaches to only 0.05. However, after long time, the convective mixing becomes traceable. **Figure 6.3c** shows CO_2 concentration fingers after 500 years and some of them reach around half of height of the reservoir producing average dissolution of 0.15. Since we introduced initial perturbations of the wavelength of 24, convection cells start to evolve in 23 segments and they merge together as the movement of fluids becomes stronger. Nevertheless, some fingers grow faster than the others and the finger wavelength increases due to random but stronger nonlinear interactions. It is also observed that the CO_2 front movement is relatively faster close to the sidewalls than the central region. Decreasing the value of N to 50 exhibits marginal difference (Ra_e = 980), and is not shown separately. Further decrease of N to 2 decreases the overall Rayleigh number to 500 which basically shows only diffusion even after 500 years (not shown here). Although the interface is perturbed, the imposed initial disturbances are damped and the CO_2 front advance as diffusion like manner.

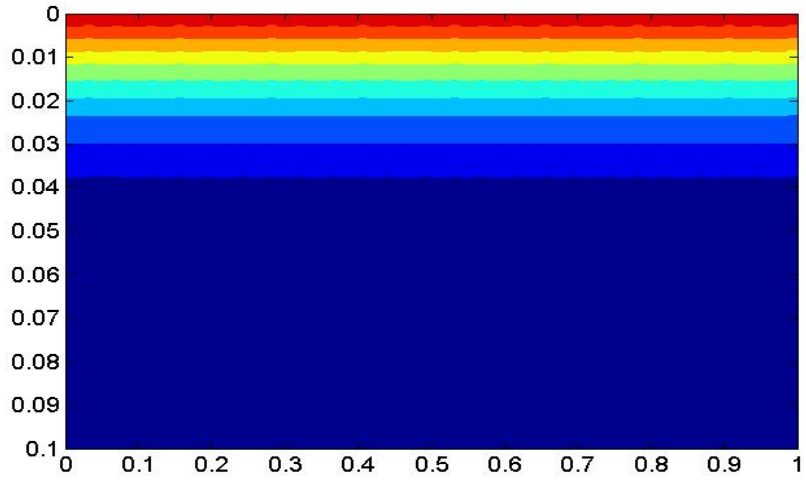

(a)

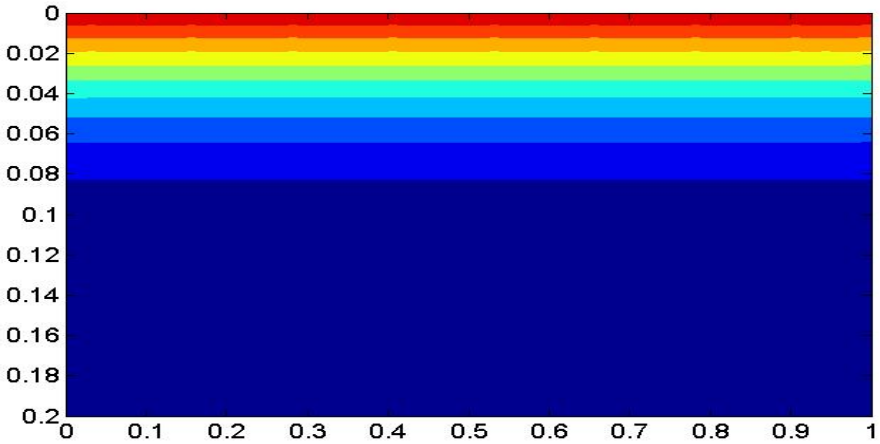

(b)

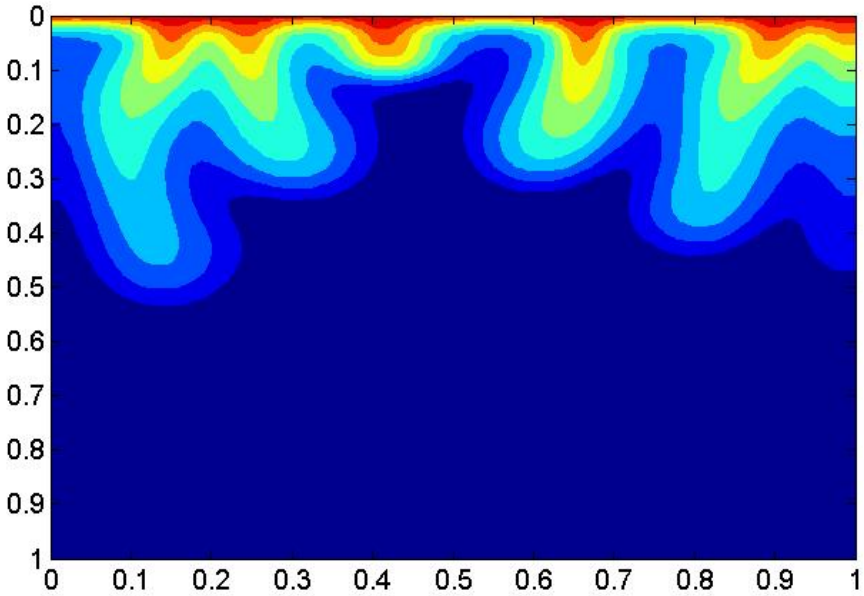

(c)

Figure 6.3: Concentration profiles for Ra_s = 1000, N = 100, at (a) t = 20, (b) t = 100, and (c) t = 500 years.

Now the case for Ra_s = 10,000 and N = 100 (Ra_e = 9,900) **Figure 6.4** shows the CO_2 concentration distribution at several time levels. Here the Rayleigh number is high enough to instigate natural convection even at early periods. Small convection cells are clearly seen in Figure 4a after the simulation is run up to 4 years. At this time, the average concentration is 0.02. The CO_2 concentration is distributed more evenly as time elapses. From 23 fingers generated initially reduce to 8 after 10 years with a corresponding dissolution of 0.03 as is seen in the

figure. The fingers keep moving downward dissolving more CO_2 (0.07 after 20 years) in brine. Many of the fingers are observed to undergo strong interactions while others are in the process of being faded. When the CO_2 front first reaches to the bottom of the reservoir (after 68 years) only one isolated big central plume survives, while two other fingers on both sides of the central plume, originating from single feeding site on top, are still in competition. Dynamics of the fluid movements becomes irregular. As the time passes new feeding sites appear as the older ones are banished. In other regions, multiple fingers can attach to a single feeding site, a process which is governed by the diffusion; the non-linear dynamics then selects one over the others as the favorable flow path[27]. This is noteworthy that the merging process starts at the stem sides rather than at the tip of the fingers and from there they spread to the rest of the system.

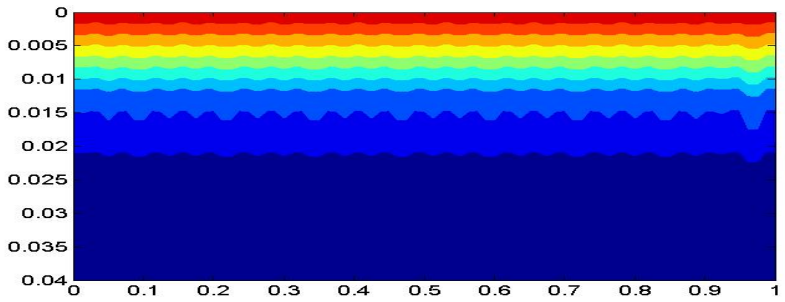

(a)

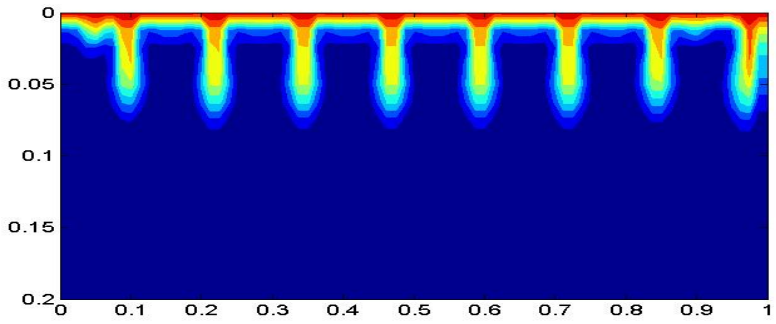

(b)

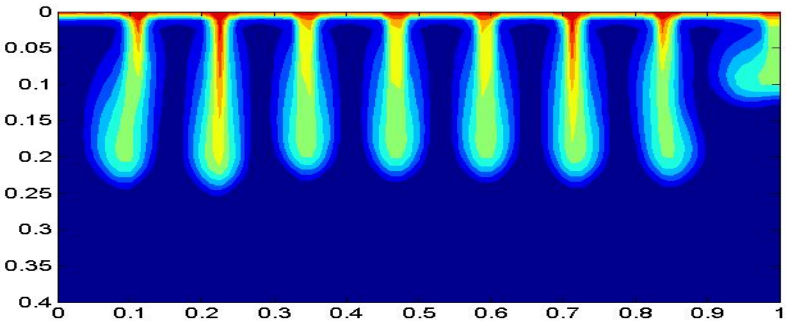

(c)

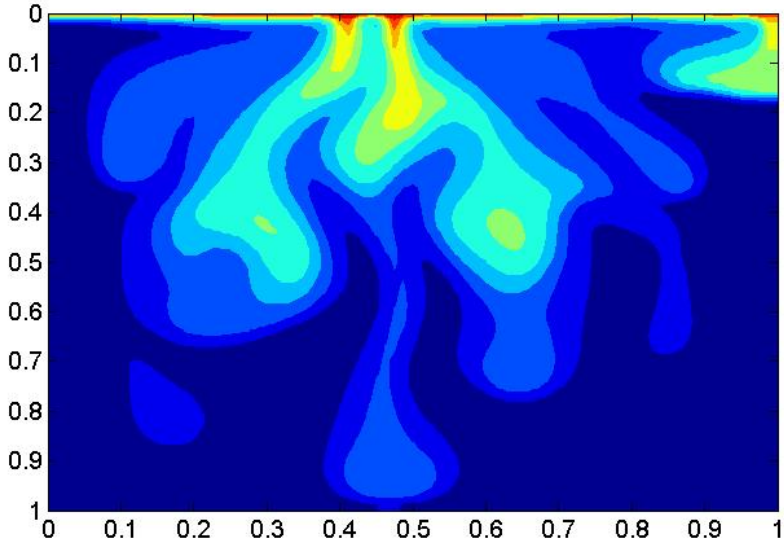
0
0.1
0.2
0.3
0.4
0.5
0.6
0.7
0.8
0.9
1
0
0.1
0.2
0.3
0.4
0.5
0.6
0.7
0.8
0.9
1

(d)

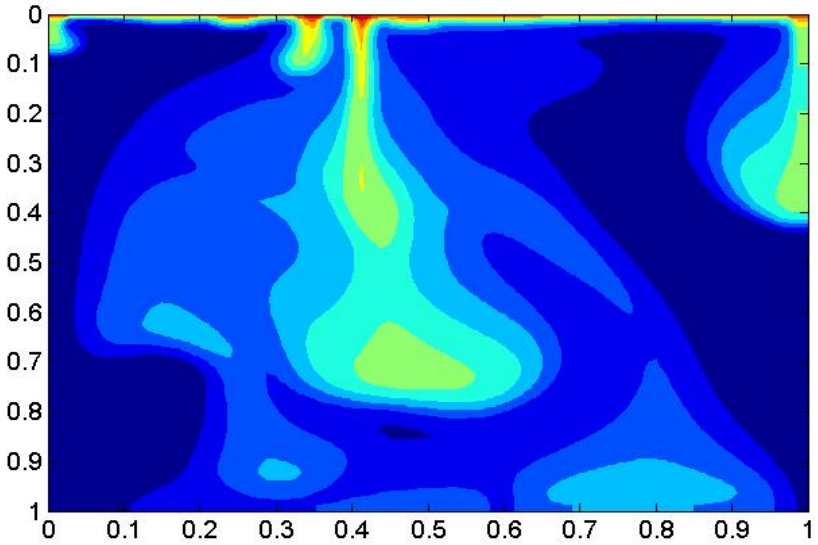
0
0.1
0.2
0.3
0.4
0.5
0.6
0.7
0.8
0.9
1
0
0.1
0.2
0.3
0.4
0.5
0.6
0.7
0.8
0.9
1

(e)

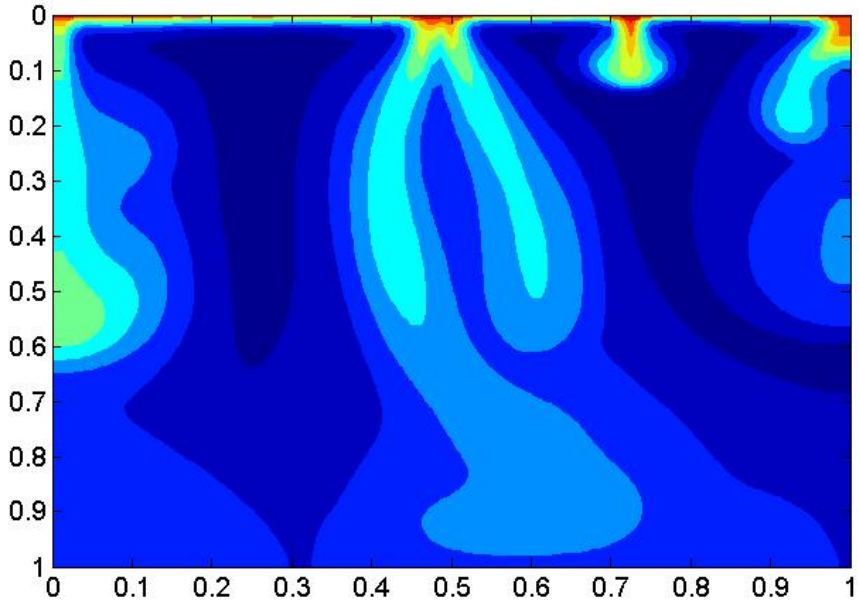

(f)

Figure 6.4: Concentration profiles for Ra_s = 10000, N = 100, at (*a*) t = 4, (*b*) t = 10, (*c*) t = 20, (*d*) t = 68, (e) t = 100, and (*f*) t = 500 years.

The larger fingers travel with less interactions with the neighboring fingers. Moreover, large fingers are connected to the thin diffusive shear layer at discrete locations serving as the feeding sites of high-density fluid for the fingers. The animation of the transient advancement of the plumes (Ra_e = 9,900) may be watched in the YouTube site (http://www.youtube.com/watch?v=mEMrxHo_Z7s). Though CO_2 reaches at the bottom relatively early, the saturation is below 0.20. **Figure 6.4f** shows simulation results for 500 years. The late stage behavior of the convection process cannot be ascertained from the results of early stage and the rate of dissolution is unpredictable. Porosity, permeability, density difference, temperature difference, etc. are the factors which all are retained in the Rayleigh number and therefore the complexity in the flow behavior is strongly dependent on this Rayleigh number (both solutal and thermal). It is already apprehended that the concentration front spreads faster for larger equivalent Rayleigh number. Average dissolution of CO_2 in the reservoir after 100 and 500 years is 0.21 and 0.62, respectively for N = 100. When N is reduced to 2, these corresponding dissolutions are 0.16 and 0.47, respectively. The concentration contours of this

case are shown in **Figure 6.5**. At early stages CO_2 dissolutions are same (0.02) for both N = 100 and 2. This is because at the early stages the transport process is completely diffusion dominated. As mentioned earlier, the CO_2 front reaches the bottom of the aquifer after 68 years when N = 100 while the front advances little more than half of the reservoir depth for N = 2 even after 100 years.

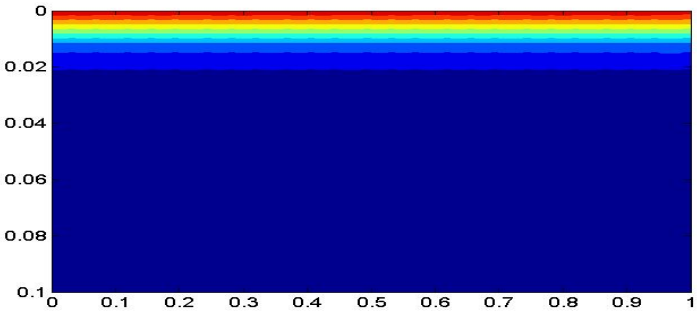

(a)

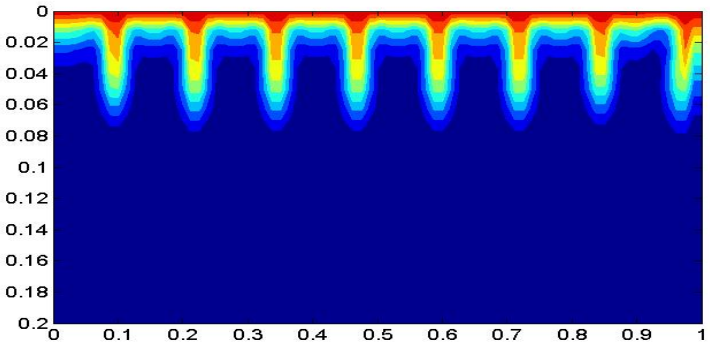

(b)

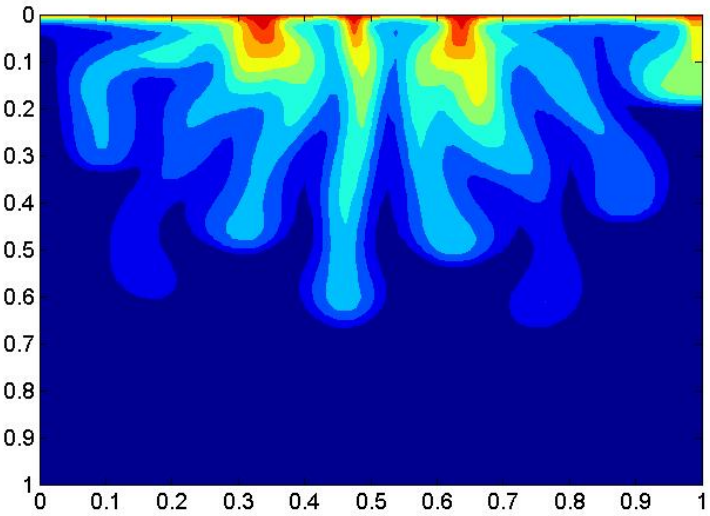

(c)

(d)

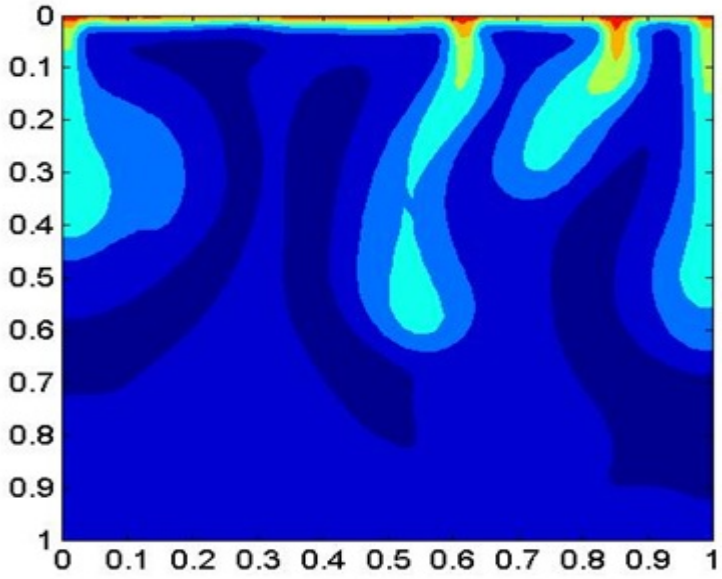

Figure 6.5: Concentration profiles for Ra_s = 10,000, N = 2, at (a) t = 4, (b) t = 20, (*c*) t = 100, (*d*) t = 500 years.

6.4.2 Effects of A

In order to understand the effects of reservoir aspect ratio on the transport process additional computations are performed for A = 0.5 (laterally wide) and A = 2 (deep well). At early stages (< 20 years), the diffusion dominated average dissolution of CO_2 are almost same ($\bar{S}$ ~ 0.02 after 4 years and 0.07 after 20 years) for any aspect ratio while at later stages (> 100 years) the average dissolution varies slightly with aspect ratio. **Figure 6.6** shows the evolution of the CO_2 concentration front with time for Ra_s = 10,000, N = 100, and A = 0.5. The CO_2 distribution after 100 years is very uneven.

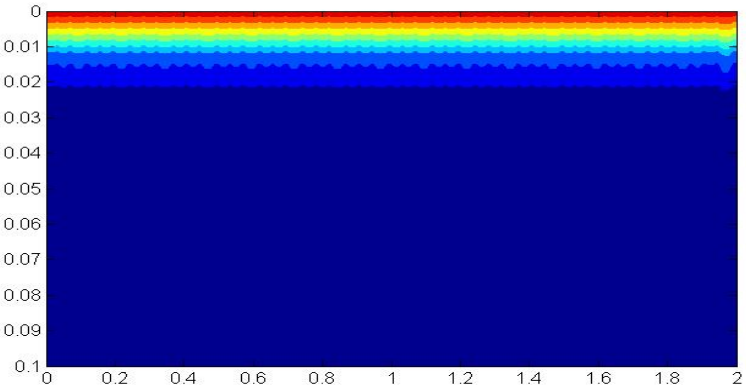
0
0.01
0.02
0.03
0.04
0.05
0.06
0.07
0.08
0.09
0.1
0
0.2
0.4
0.6
0.8
1
1.2
1.4
1.6
1.8
2

(a)

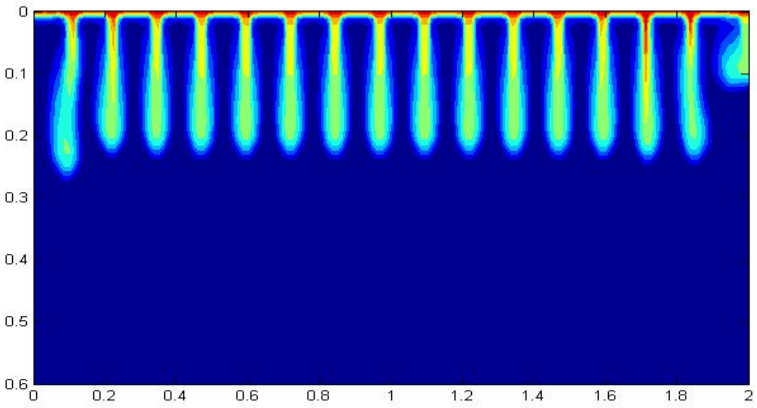
0
0.1
0.2
0.3
0.4
0.5
0.6
0
0.2
0.4
0.6
0.8
1
1.2
1.4
1.6
1.8
2

(b)

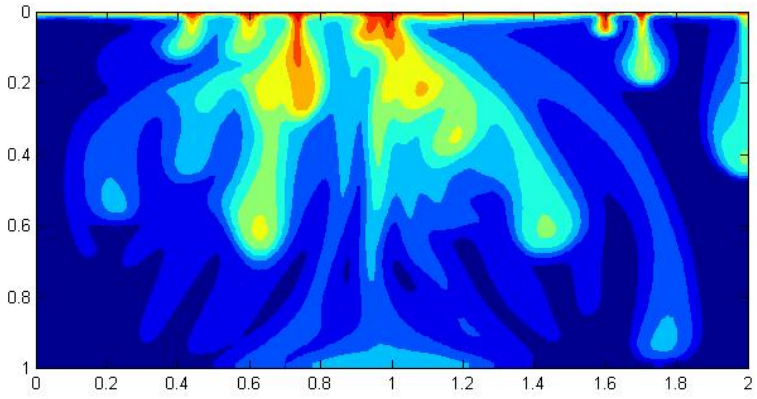
0
0.2
0.4
0.6
0.8
1
0
0.2
0.4
0.6
0.8
1
1.2
1.4
1.6
1.8
2

(c)

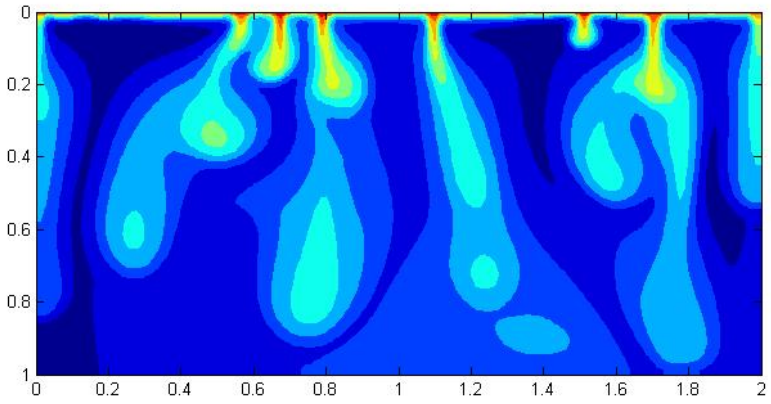

(d)

Figure 6.6: Concentration profiles for Ra_s = 10,000, N = 100, A = 0.5, at (a) t = 4, (b) t = 20, (c) t = 100, (d) t = 500 years.

Interestingly, the mixing is very slow near the side walls. It is also noted that the reservoir aspect ratio has little effect on the CO_2 dissolution. Making the thermal effect significant by decreasing N to 2, the concentration distribution obtained at 100 and 500 years are shown in **Figure 6.7.** Unlike for N = 100, at 100 years the mixing seems even and almost symmetrical about the vertical midline. In this case, the increased thermal effect counteracts with the solutal buoyancy effects making the dissolution process slower. Therefore the average dissolution is low (0.17). Over time the front propagation little more accelerates resulting in average dissolution 0.48 after 500 years.

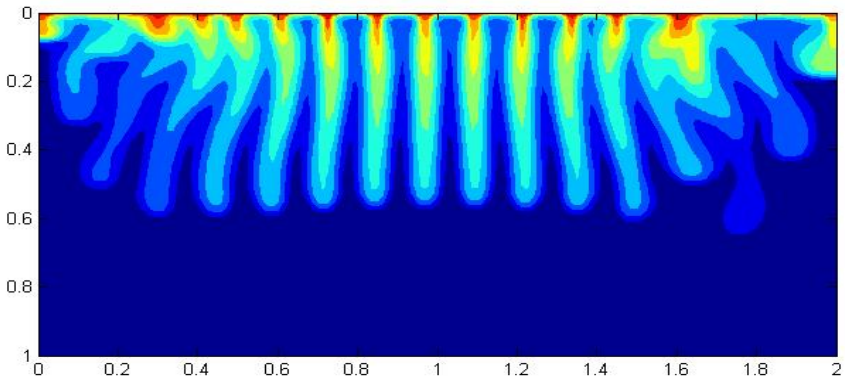

(a)

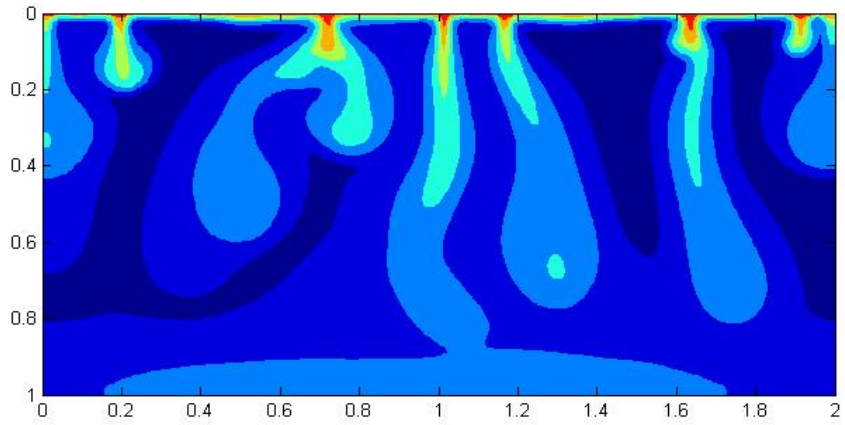

(b)

Figure 6.7: Concentration profiles for Ra_s = 10000, N = 2, A = 0.5, at (a) t = 100, (b) t = 500 years.

For a deeper reservoir (A = 2) **Figure 6.8** shows the results for the case Ra_s = 10000, N = 100. In this case also, the early stage behavior is same. The 23 cells merge to form only 4 plumes after 20 years where concentrations at left walls are invariant and one front advances along the edge of the right wall. The middle three CO_2 fronts merge to only a long one as time marches. However, the plume at the right edge becomes bigger pushing others to left. Thus the dissolution

accelerates reaching 0.60 after 500 years. When the temperature effect is increased (N = 2) the long term dissolution process changes. After 100 years of simulation plumes of various random sizes and shapes are traced. During the 500 year period only one big CO_2 front is survived, which is yet to reach the bottom. Average concentration of the aquifer at this time is 0.46. These are shown in **Figure 6.9**. Actually internal interactions among the fingers decrease, and the time required for CO_2 front to touch the bottom of the reservoir increases with increasing aspect ratio. These are consistent with the findings by Farajzadeh et al [20].

(a)

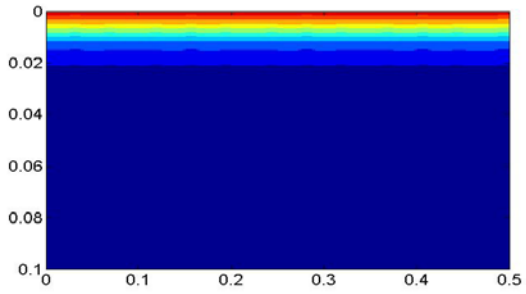

(b)

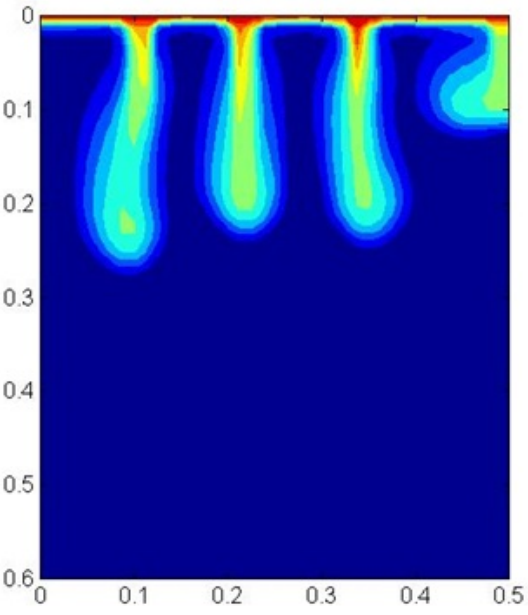

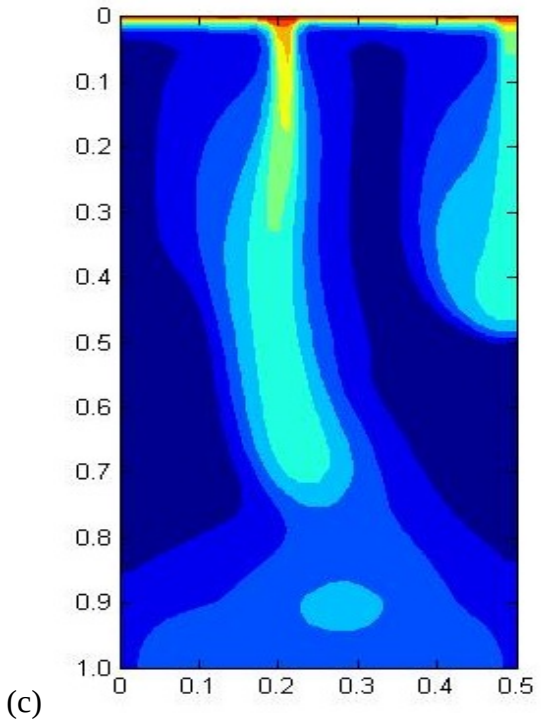

(c)

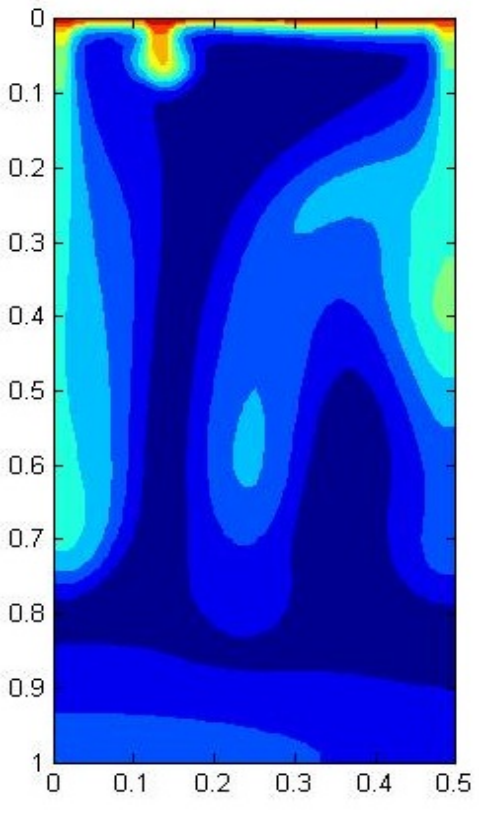

(d)

Figure 6.8: Concentration profiles for Ra_s = 10000, N = 100, A = 2.0, at (a) t = 4, (b) t = 20, (c) t = 100, (d) t = 500 years.

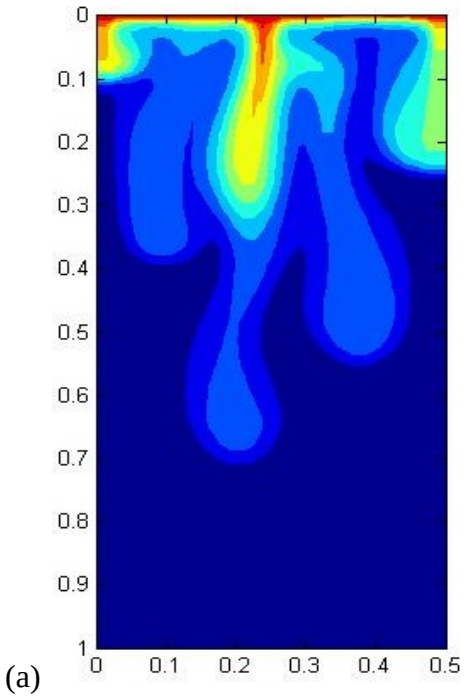

(a)

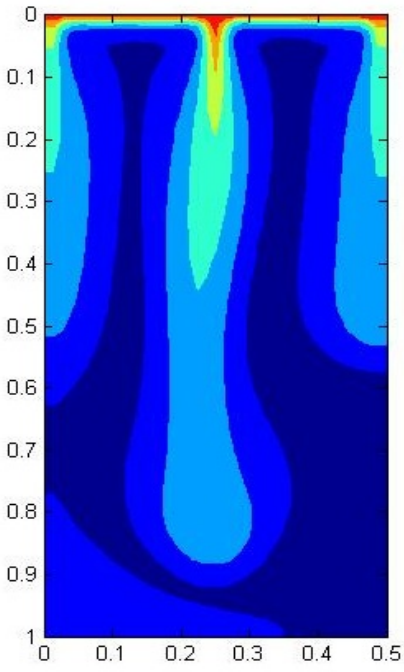

(b)

Figure 6.9: Concentration profiles for Ra_s = 10000, N = 2, A = 2.0, at (a) t = 100, (b) t = 500 years.

Figure 6.10 shows the average dissolution of CO_2 over time up to 500 years in a square reservoir (A = 1) for various equivalent Rayleigh number, Ra_e. In early years (< 80) the average

dissolution rate is faster than that at later times while the dissolution rate increases with increasing Ra_e. For lower values of Ra_e the CO_2 dissolution rate is slower because convective flow is weak and diffusion tends to dominate. To understand the behavior of the dissolution rate over a very long period, simulations were run up to 6,000 years at a fixed Ra_e of 9,900 for a square reservoir and the dissolution rate is presented in **Figure 6.11**. It is noted that up to about 450 years the slope is very steep. After that the rate becomes slower and after 2,000 years, the rate of dissolution becomes asymptotic. Primarily every concentration finger is surrounded by thin shear layer, as they mix together over the time the layer becomes thicker and after long time the propagation again is diffusion dominated. To reach complete equilibrium stage when CO_2 concentration in the aquifer is uniform everywhere, may require thousands of years. **Figure 6.12** shows the effects of aspect ratios on CO_2 dissolution rate. It is observed that CO_2 dissolution rate increases slightly as the reservoir becomes laterally wide with increasing aspect ratio. Because fluid gets more free space to move in laterally wide reservoir enhances the convection. Therefore from practical point of view laterally wide reservoir is better candidate than the deep aquifer for sequestration of CO_2.

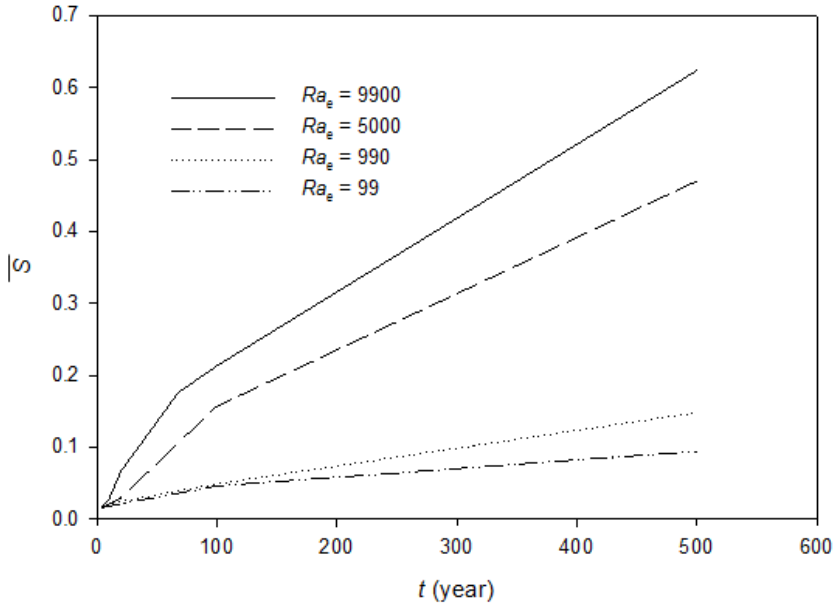

Figure 6.10: average dissolution over the time for different Ra_e's (A = 1).

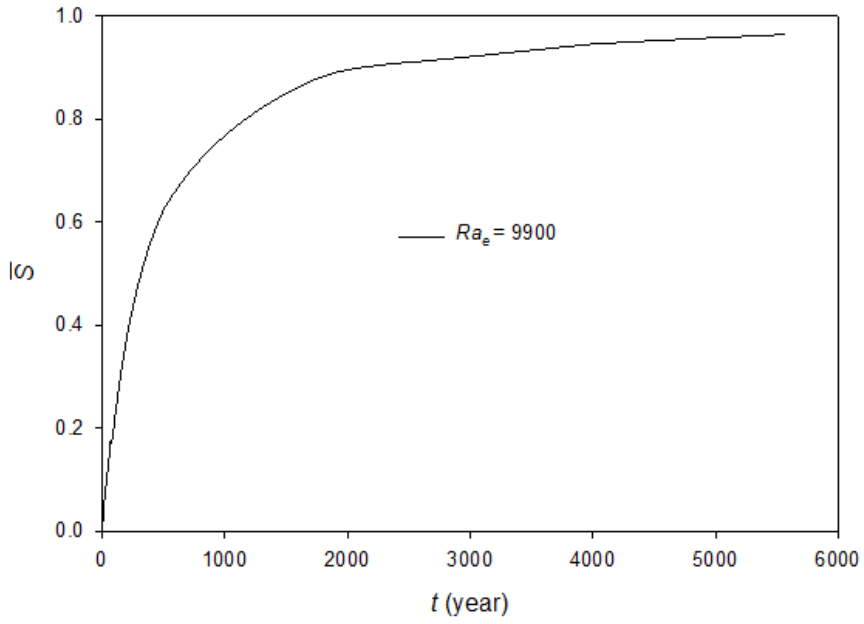

Figure 6.11: average dissolution over the time for different Ra_e = 9900 (A = 1).

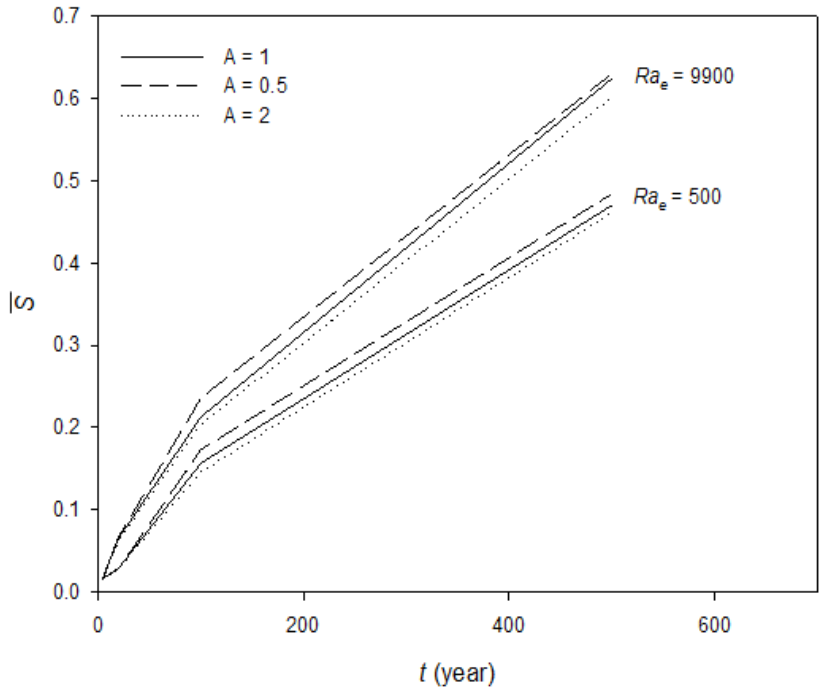

Figure 6.12: average dissolution over the time for different aspect ratios.

6.5 Concluding remarks: Double diffusive natural convection in a two dimensional brine saturated porous media, subjected to vertical concentration and temperature gradients, is investigated numerically. The study is focused on the influence of the solutal and thermal buoyancy forces on the propagation of the concentration front and its resulting dissolution into the brine in the context of CO_2 sequestration in underground reservoirs. It is found that the thermal effect does not interfere the natural convection process significantly unless the buoyancy ratio, N, is low and close to one. For higher values of N (>50), the equivalent Rayleigh number, Ra_e, does not change much and the double diffusion is basically like density-driven mass transfer due to concentration variation. The convection process enhances with increasing Ra_e which depends on reservoir characteristics and physical properties of the brine, viz., porosity, permeability, diffusivity, concentration gradient, thermal gradient, etc.

As the time passes the number of CO_2 fronts decrease due to decreasing convection process. At very initial stage (<10 years) the average CO_2 dissolution is same for all cases studied because of diffusion domination propagation. After 500 years of simulation CO_2 dissolution is over 0.60 for N = 100, and over 0.40 for N = 2. After 2000 years the dissolution process again becomes very slow. The reservoir may be completely CO_2 saturated after thousands of years. Changing reservoir aspect ratio does not affect the average dissolution rate much, however the laterally wide reservoir is favorable than the deeper one.

6.6 Notations:

A aspect ratio, H/L [-]
c concentration [mol/m^3]
C_p heat capacity at constant pressure [Jkg^{-1}K^{-1}]
D Diffusion coefficient [m^2/s]
g acceleration due to gravity [m/s^2]
H porous medium height [m]
k permeability [m^{-2}]
L porous medium length [m]
n number of nodes
p pressure [Pa]
Le Lewis number [-]
Pe Peclet number [-]

Pr Prandtl number [-]
Ra Rayleigh number [-]
$\overline{S}$ average saturation
t time [s]
u velocity [m/s]
x distance along x-axis
z distance along z-axis

Greek letters
α thermal diffusivity
β_c coefficient of density increase by concentration [m^3/mol]
β_T coefficient of thermal expansion [K^{-1}]
φ porosity [-]
μ viscosity [$kgm^{-1}s^{-1}$]
κ thermal conductivity []
ρ density [kg/m^3]
ψ stream function [$m^3/m^{-1}s^{-1}$]

Superscript
* Dimensionless quantity

Subscripts
0 initial value
c concentration
i node in x – direction
j node in z – direction
r reference value
s solutal
T Temperature
x x-coordinate
z z-coordinate

6.7 References:

[1] Hassanzadeh, H., Pooladi-darvish, M., Keith, D. W., *J. Can. Pet. Technol. 44,* 43-51, 2005.

[2] Farajzadeh, R., Zitha, P. L. J., Bruining, J., *Ind. Eng. Chem. Res., 48,* 6423-6431, 2009.

[3] Islam, A.W., Carlson, E.S., *Energy & Fuels, 26,* 5330-5336, 2012.

[4] Lindeberg, E., Wessel-berg, D., *Energy Convers. Mgmt., 38,* S229-S234, 1997.

[5] Hassanzadeh, H., Pooladi-darvish, M., Keith, D.W., *AIChE J., 53,* 1121-1131, 2005.

[6] Stern, M.E., *Ocean circulation physics*. Academic Press, New York, 1975.

[7] Oldenburg, C.M., Pruess, K., *Transport in Porous Media, 33,* 29-63, 1998.

[8] Cooper, C.A., Glass, R.J., Tyler, S.W., *Water Resources Research, 33,* 517-526, 1997.

[9] Cooper, C.A., Glass, R.J., Tyler, S.W., *Water Resources Research, 37,* 2323-2332, 2001.

[10] Green, T., *Water Resources Research, 20,* 1225-1229, 1984.

[11] Poulikakos, D., *Int. Comm. Heat Mass Trans., 13,* 587-598, 1986.

[12] Mojtabi, M.C.C., Razi, Y.P., Mojtabi, J., *Transport phenomena in porous media*, edited by D. B. Ingham and I. Pop, Vol. iii, (Elsevier Ltd., Kidlington, 2005.

[13] Javaheri, M., Abedi, J., Hassanzadeh, H., *Transport in Porous Media, 84,* 441-456, 2010.

[14] Bhadauria, B.S., *Z. Naturforsch, 61a,* 335-344, 2006.

[15] Sodha, M.S., Kumar, A., *Energy Convers. Mgmt., 25,* 463-468, 1985.

[16] Ennis-King, J., Paterson, L., presented at the SPE Annual Technical Conference and Exhibition, Denver, Colorado, 2003 (unpublished).

[17] Ennis-King, J., Paterson, L., *SPE J., September,* 2005.

[18] Burnett, R.D., Frind, E.O., *Water Resources Research, 23,* 689-694, 1987.

[19] Simpson, M.J., Clement, T.P., *Advances in Water Resources, 26,* 17-31, 2003.

[20] Farajzadeh, R., Salimi, H., Zitha, P.L.J., Bruining, J., *Int. J. Heat Mass Transfer, 50,* 5054-5064, 2007.

[21] Landau, L.D., Lifshitz, E.M., *Statistical physics: course of theoritical physics.* Pergamon Press, 1969.

[22] R. D. Gunn and W. B. Krantz, 1980 (unpublished).

[23] Yortsos, Y.C., Xu, B., Salin, D., *Phys Rev Lett, 79,* 4581-4584, 1997.

[24] Lerner, K.L., Lerner, B.W., Gale Cengage, Farmington Hills, MI, 2003.

[25] Newell, D.L., Viswanathan, H.S., Lichtner, P.C., Carey, J.W., Kaszuba, J.P., *American Geophysical Union Meeting,* Sanfrancisco, Dec 5-9, 2011.

[26] Sharqawy, M.H., Lienhard V, J.H., Zubair, S.M., *Desalination and Water Treatment, 16,* 354-380, 2010.

[27] Riaz, A., Hesse, M., Tchelepi, H.A., Orr, F.M., *J. Fluid Mech. 548,* 87-111, 2006.

CHAPTER SEVEN

CONCLUSION AND RECOMMENDATIONS

The sequestration of anthropogenic CO_2 into geological formations is considered as a potential method to alleviate climate change. Predicting the sequestration storage potential and long term behavior of carbon dioxide in geologic reservoirs require computations of physical properties (density, viscosity, etc.) and phase equilibrium of CO_2 and Brine mixtures at depths where temperature is within 100 °C and pressure may reach several hundred bar. Therefore, comprehensive investigations were carried out on physical property modeling of CO_2 and Brine system at these temperatures and pressures ranges.

During the development of the schemes, not only was the accuracy of the computations considered, but also the efficiency of the scheme to ensure reduction in computational expenses. This is because simulation of large-scale, long term geological storage of CO_2 is computationally intensive. The developed models for calculating density of subcritical, liquid, and supercritical CO_2, as well as phase equilibrium, and viscosity were illustrated in the first four chapters. We have shown that in using these new techniques, we could get more than 1,000 times speed-up saving in computational time.

From engineering standpoint, it is very important to ask questions regarding how CO_2 will stabilize in subsurface porous media over time after injection, what type of reservoirs are better candidates for sequestration, and how long will it take CO_2 to dissolve completely. To provide answers to these questions a thorough numerical experimentation was conducted as described in Chapter Six. From this experiment, it is concluded that at early stage (<10 years) the average CO_2 dissolution is the same for all cases considered. This is because initially the convection process is diffusion dominated. After 500 years the CO_2 dissolution is over 0.60 for $N = 100$, and over 0.40 for $N = 2$. After 2,000 years the dissolution process again becomes very slow indicating that the reservoir will be completely CO_2 saturated after very long time (thousands of years). Changing reservoir aspect ratio does not affect the average dissolution rate much; however, laterally wide reservoir is preferable to deeper aquifer.

A comprehensive overview of the simulator, “nSpyres” that is being developed by our group at the University of Alabama and the computational performance have been discussed in (Carlson et al [5]). The simulator performance was tested by solving benchmark SPE-10, Problem 2. Also, a presentation on “nSpyres” was made at Interpore Conference, held on May 14-16, 2012, at Purdue University. Currently “nSpyres” can solve two-phase flow problem and does not account for any phase changes. Therefore, more work is needed to make it suitable for solving phase change problems and to simulate CO_2 flooding. I intend to integrate my phase equilibrium models with nSpyres. I will continue to contribute my quota in this open source project.

For the reservoir simulation, well flow models were reviewed extensively in our recent review article Francis et al [6]. In this review paper, we assessed the impacts of well flow models on numerical reservoir simulation performance.

In reservoir simulation models, pressure equations are in elliptic forms where systems of equations arise in the form $Au = b$. Here A is a linear operation to be performed on the unknown data u, produce the known right-hand side b representing some constraints of known or assumed behavior of the system being modeled. Since such systems can be very large, solving them directly can be too slow. In contrast, a multigrid solver solves partially at full resolution and directly only at low resolution. This new solver [7] was presented at SciPy (Scientific Python) conference, held on July 16-21, 2012, in Austin, TX.

REFERENCES

[1] Ozgur, E., Gumrah, F. *Energy Sources, Part A: Recovery, Utilization, and Environmental Effects*, *31,* 698-709, 2009.

[2] Justus, J.R., Fletcher, S.R. Global climate change. *Congressional Research Service, March 2006, Report no. RL 33602, Washington DC*, 2006.

[3] Ozgur, E., Gumrah, F. *Energy Sources, Part A: Recovery, Utilization, and Environmental Effects*, *32,* 674-687, 2010.

[4] Bachu, S. *Energy Convers Magmt*, *41,* 953-970, 2000.

[5] Carlson, E.S., Islam A.W., Dumkwu, F.A. *nSpyres: An Open Source Python Based Framework for Simulation of Flow through Porous Media. Advances in Water Resources (in review)*

[6] Dumkwu, F.A., Islam A.W., Carlson, E.S. *A Review of Well Models and Assesement of their Impacts on Numerical Reservoir Simulation Performance*. *J Pet Sci Eng., 82-83*, 174-186, 2012.

[7] Bertalan, T.S., Islam, A.W., Sidje, R.B. *OpenMG: A New Multigrid Implimentation in Python*. *Numerical Linear Algebra with Applications (in review)*